Preparation of Single Crystal Molybdenum Bronzes and Polycrystalline Rubidium Molybdenum Oxide

by

Darren Hicks

A THESIS SUBMITTED IN PARTIAL FULFILMENT OF
THE REQUIREMENTS FOR THE DEGREE OF

MASTER OF SCIENCE

in

The Faculty of Mathematics and Sciences

Department of Physics

BROCK UNIVERSITY

August 24, 2017

In presenting this thesis in partial fulfilment of the requirements for an advanced degree at the Brock University, I agree that the Library shall make it freely available for reference and study. I further agree that permission for extensive copying of this thesis for scholarly purposes may be granted by the head of my department or by his or her representatives. It is understood that copying or publication of this thesis for financial gain shall not be allowed without my written permission.

(Signature) _____

Department of Physics

Brock University
St. Catharines, Canada

Date _____

Abstract

Lithium purple bronze (LiPB) $Li_{0.9}Mo_6O_{17}$ was studied extensively in the 1980's and has recently regained interest in the research community. The mechanism for the metal-insulator (M/I) transition at $\sim$25 K and superconductivity at $\sim$2 K is still unknown. The temperature gradient flux technique has been used to grow single crystal LiPB. A large superconducting LiPB single crystal was grown (dimensions: $4.7 \times 3.0 \times 1.2$ mm^3) and characterized and will be referred to throughout this work as 'I33sc2'. For the non-superconducting single crystal oriented along the b-crystallographic axis, we found the maximum value of the energy gap to be 2 meV$\pm$0.1 meV at 9.16 K, which is different from the accepted literature value of $\sim$1 meV at 5-6 K [1, 2]. Furthermore, heavier alkali metals (Na, K and Rb) were used in the temperature gradient flux technique. Small lilac brown single crystals were found in all three growths. In particular, the rubidium growth yielded polyhedral (denoted as 'POLY', having approximate dimensions: $0.5 \times 0.3 \times 0.3$ mm^3) and small bar shaped (denoted as 'SBAR', having approximate dimensions: $1 \times 0.1 \times 0.1$ mm^3) lilac brown single crystals which exhibited anomalous properties in the resistivity and specific heat. The anomalous properties include a M/I transition at

250 K and a small phase transition in the resistivity at 94 K. These lilac brown single crystals were studied with powder X-ray diffraction (XRD) and match very closely with molybdenum dioxide MoO_2, however with slightly larger 'a' and 'b' lattice parameters. These lilac brown crystals are being further characterized with single crystal XRD. Polycrystalline rubidium molybdenum dioxide $Rb_{0.03}MoO_{2-\delta}$ was then grown to further understand what rubidium doping (if any) these lilac brown single crystals have. The resistivity of polycrystalline $Rb_{0.03}MoO_{2-\delta}$ has a M/I transition at 250 K, similar to the lilac brown single crystals, but lacks a phase transition at 94 K. Unlike the lilac brown single crystals, the slope of the M/I transition at 250 K is strongly affected by thermal cycling. Furthermore, polycrystalline $Rb_{0.03}MoO_{2-\delta}$ shows signs of a small superconducting volume fraction. This material is under further investigation.

Contents

List of Figures

List of Tables

Acknowledgements

I would like to thank Dr. Razavi for his belief in my abilities as a student and a researcher. I would like to thank Dr. Razavi and Dr. Reedyk for all of their advice, ideas and help throughout my thesis. I would also like to thank Dr. Bose for the continued support and kind words of encouragement. Furthermore, I would like to thank Jon Aguilar and Jesse Lock for their support through my research and writing. Brock University is an ideal environment because it has allowed me to incorporate family, fitness and physics in my life in a balanced way. I would like to thank Barbara, Richard, Amanda, grandma and grandpa Hicks for their continued support throughout my studies at Brock. I would like to dedicate this work to my grandma and grandpa Coulis, you are missed and loved.

'He that followeth after righteousness and mercy findeth life, righteousness, and honour.'

Proverbs 21:21 (KJV)

Chapter 1

Introduction

The molybdenum oxide family has various compounds. In particular, molybdenum bronzes refer to the type of single crystal represented by the chemical formula $A_xMo_zO_y$. The molybdenum bronzes have metallic or semiconducting properties and appear shiny [3]. The blue bronzes are single crystals represented by $A_{0.3}MoO_3$ (A=K,Rb,Tl). These compounds have quasi-one-dimensional and quasi-two-dimensional metallic behaviour and display a charge-density wave (CDW) which is represented by a metal-insulator transition. This transition can be clearly seen in the resistivity as a function of temperature data [3]. Molybdenum dioxide MoO_2 is an good conductor (see section 1.2) and is one of three starting compounds in the growth of the molybdenum purple bronzes [3]. The molybdenum purple bronzes (or just 'purple bronzes') are represented by the following chemical formula $A_{0.9}Mo_6O_{17}$ where A=Li, Na, K and Tl [3]. The purple bronzes A= Na and K are quasi-two-dimensional conductors which display a CDW state [8]. $Li_{0.9}Mo_6O_{17}$, a

one-dimensional conductor, has a metal-insulator (M/I) transition in the resistivity at $\sim$ 25K (see Chapter 1.1). Recently, polycrystalline $K_{0.05}MoO_{2-\delta}$ has produced anomalous results in the resistivity, specific heat, thermal expansion and DC susceptibility [4]. Furthermore, polycrystalline $K_xMoO_{2-\delta}$ has been confirmed as superconducting for x= 0.05, 0.1, 0.25 and 0.3 where $3.9K < T_C < 9.5K$ depending on the K doping [4–7]. $Li_{0.9}Mo_6O_{17}$ will be the main topic of focus in this work. Single crystal MoO_2 and polycrystalline rubidium doped MoO_2 will also be discussed.

1.1 Lithium Purple Bronze $Li_{0.9}Mo_6O_{17}$

The compound $Li_{0.9}Mo_6O_{17}$ (lithium purple bronze or LiPB) is a quasi one-dimensional conductor and has been studied in detail since the 1980's [3, 9–13]. There is some discrepancy over the resistivity along the 'a' and c-crystallographic axes [3, 14, 15], however it has been agreed upon that the b-crystallographic direction is the lowest resistive direction. For the purple bronze materials, the alkali metal (Li, Na or K) donates its outer electron to the conduction band [16]. Due to the anisotropic crystal structure of this class of compounds, metallic behaviour is constrained to two-dimensions (sodium and potassium purple bronze) [17] and one-dimension (lithium purple bronze) [14]. The two most interesting features of LiPB are the superconducting transition at ∼2K (See Figure 1.1) and the metal-insulator (M/I) transition at ∼25K (see Figure 1.2) [3].

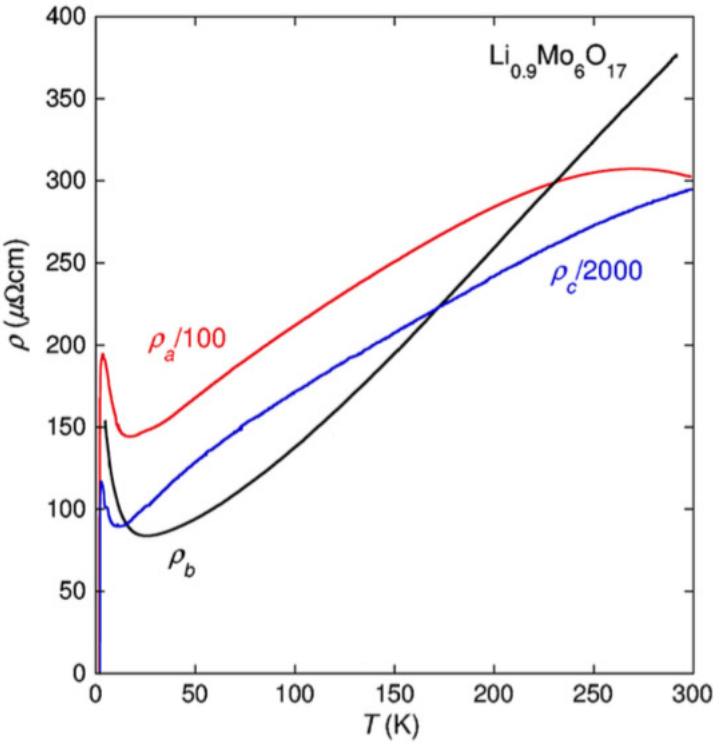

Figure 1.1: Resistivity of $Li_{0.9}Mo_6O_{17}$ along all three crystallographic axes shows its low dimensionality. ρ_b(T) only goes down to 4.2K. Figure taken from [18].

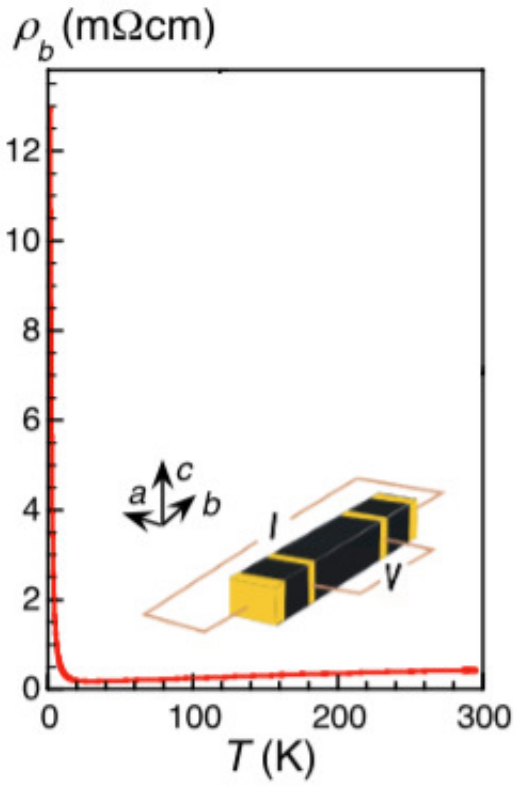

Figure 1.2: The M/I transition in non-superconducting $Li_{0.9}Mo_6O_{17}$ oriented along the lowest resistive axis, parallel to the b-crystallographic lattice parameter. Figure taken from [1].

There are two interpretations proposed by the scientific community to be the cause of this 25K M/I transition: Luttinger liquid and charge density wave (CDW) which will be summarized in Chapter 2. The mechanism for the superconductivity of LiPB is still unknown, however studies suggest that it may possibly be a spin-triplet superconductor [18–20].

The space group for LiPB is $P2_1/m$ [21]. The 'P' here stands for primitive [22], hence the lattice parameters are all different (i.e. a≠b≠c [23, 24]. The '2_1' here is the screw axis and glide plane rule [25]. In this case we have a

180^o rotation about the c-axis and translation down the c-axis by a value of the c-lattice parameter [22] (c= $9.499\mathring{A}$ for LiPB [21]). Lastly, 'm' is a mirror plane, objects are reflected to the other side of this plane. Figure 1.3 shows the crystal structure of LiPB looking down the b-crystallographic axis. Figure 1.3 was compiled using Jmol software [26] and the .cif file obtained from the COD database [27] is taken from reference [21]. The lithium atoms are pink, the molybdenum atoms are turquoise and the oxygen atoms are red. One can clearly see the conducting chains along the b-crystallographic axis which consist of Mo(1) atoms (yellow lines) and Mo(4) atoms (orange lines) [21]. The O(11) atoms (blue lines) are sandwiched between these two conducting chains. Notice that the lithium atoms appear to separate planes perpendicular to the 'a' lattice parameter. This observation suggests that single crystals will have planes perpendicular to the 'a' lattice parameter. This phenomenon is observed in Figure 4.14 (discussed in Chapter 4.2.1) and [12], where the 'a' lattice parameter is perpendicular to the plane of the crystal.

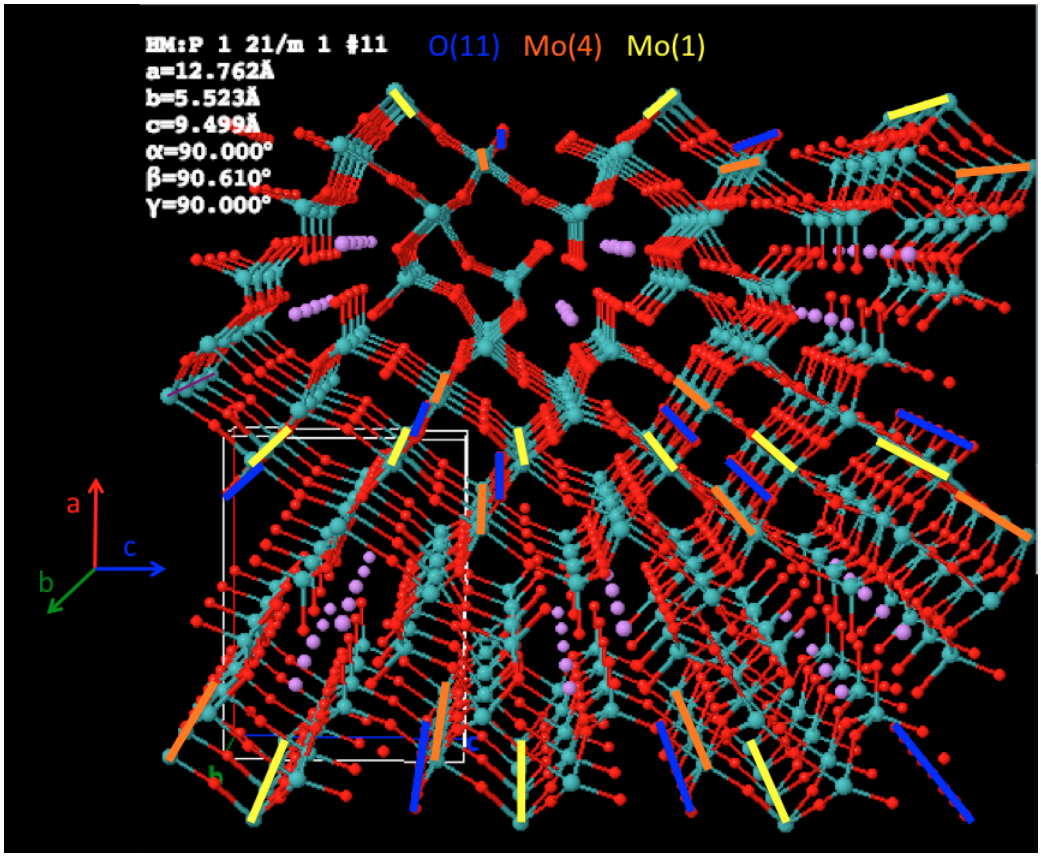

Figure 1.3: View down the b-axis of LiPB.

The structure of LiPB is composed of octahedral and tetrahedral bundles with a single molybdenum atom at the centre and oxygen atoms located at the vertices [21]. The Mo(1) and Mo(4) atoms both form MoO_6 polyhedra and have valences of 5.05 and 5.01, respectively [28] (as can be seen by Figure 1.3). Hence, the highest concentration of unpaired electrons are located around the Mo(1) and Mo(4) sites. The other molybdenum atoms have less electron contribution due to some forming the MoO_4 polyhedra and their slightly higher valences (Mo(2) has a valence of 5.72 and Mo(3), Mo(5) and Mo(6) have valences of 5.76) [28]. Therefore, the Mo(1)-O(11)-Mo(4)-O(11) atoms form the conducting chains giving strong one-dimensional conductivity along the b-crystallographic axis.

1.2 Molybdenum Dioxide MoO_2

Molybdenum dioxide (Molybdenum (IV) Oxide) has been a widely studied compound. Single crystal MoO_2 is a good metallic conductor [24, 29], does not show any signs of a M/I transition in the resistivity [30] and displays a Peierls-type instability [31] (summarized in Chapter 2). It is known that polycrystalline and thin film MoO_x properties are extremely sensitive to their oxygen doping[1] [32, 33]. Polycrystalline MoO_2 shows a M/I transition in the resistivity at roughly ~ 100 K which is suppressed at lower oxygen doping [32][2]. Two binary oxides of molybdenum exist, namely molybdenum dioxide MoO_2 and its sister compound molybdenum trioxide MoO_3 [24]. It has been shown that MoO_3 powder can be reduced to MoO_2 [24], specifically to purities of 99% at 500^oC in $H_{2,gas}$ being pumped at a rate of 8 litres/hour (the temperature of the $H_{2,gas}$ being kept at a constant 5^oC)[3] [34]. The crystal structure of MoO_2, shown in Figure 1.4, is monoclinic with space group $P2_1/c$ [31]. The reported lattice parameters of this compound vary quite substantially (see Table 1.1).

[1]For polycrystalline MoO_x the properties were explored in the range $1.85 \leq x \leq 2.05$ [32] and for thin film MoO_x the properties were explored at 5, 53, and 64 atom % of oxygen [33].

[2]For polycrystalline MoO_y with y=1.95 and y=2.00 there exits a M/I transition at 110K and 120K, respectively [32].

[3]The reduction time of $MoO_3 \rightarrow MoO_2$ is a function of the powder grain size, reduction temperature, $H_{2,gas}$ dew point and agglomerate size [34].

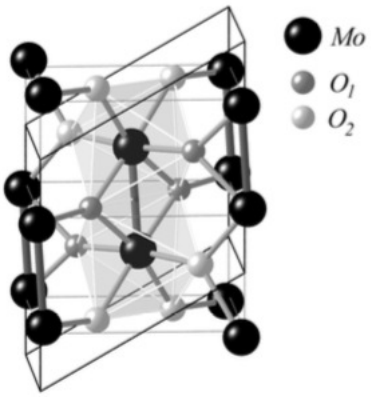

Figure 1.4: Crystal structure of monoclinic MoO_2. Picture taken from [31].

Table 1.1: Lattice parameters of MoO_2 from various sources in the literature. The 'T' stands for 'Tugarinovite' and is naturally occurring MoO_2, the 'S' stands for 'Synthetic' and is synthesized MoO_2. Data organized by unit cell volume (from smallest to largest).

Type and Source	Publication Year	a (Å)	b (Å)	c (Å)	α (^{o})	β (^{o})	γ (^{o})	Unit Cell Volume ($Å^3$)
T [23, 35]	2005, 1982	5.59	4.82	5.51	90	119.533	90	129.17
S [35, 36]	1982, 1952	5.608	4.842	5.517	90	119.75	90	130.06
S [29, 37]	1973, 1974	5.60	4.86	5.63	90	120.95	90	131.41
S [38]	1967	5.6109	4.8562	5.6285	90	120.95	90	131.52

1.3 Research Goals

Recently there has been a resurgence of interest in $Li_{0.9}Mo_6O_{17}$, specifically the metal-insulator (M/I) transition at $\sim$ 25K and the mechanism of superconductivity at $T_C \sim$ 2K [1, 14, 18, 19]. The goal of this research is to produce high quality superconducting and non-superconducting single crystals using the temperature gradient flux technique as described in reference [9]. We will probe the energy gap at $\sim$25K in non-superconducting LiPB. In addition, it seems that molybdenum dioxide MoO_2 (lilac brown single crystals) is often a by-product of the $Li_{0.9}Mo_6O_{17}$ single crystal growth using the temperature gradient flux technique [9]. However the properties of these lilac brown single crystals have not been explored thoroughly. The temperature gradient flux technique will be performed using heavier alkali metals (Na, K and Rb) and the properties of the various lilac brown single crystals will be studied.

Chapter 2

Theoretical Background

In this chapter I will give a brief description of the main theoretical ideas for the compounds LiPB and MoO_2. However, my research focus is on the synthesis and characterization of single crystals and polycrystalline materials.

2.1 Superconductivity

The most fundamental property of superconductivity is the Meissner Effect [39]. The Meissner Effect is characterized by a complete expulsion of an external field H by a superconductor when $H < H_C$ and $T < T_C$ [39][1]. There is a small layer on the surface of the superconductor that has a non zero field inside of it [39]. The thickness of this small layer is called the *magnetic penetration depth* λ. Although vanishing resistivity is the most striking property of superconductivity, some samples may only have superconducting domains [40].

[1]Here H_C is called the critical field and T_C the critical temperature [39].

This effect will show up as a transition at T_C, but the resistivity may still be a small finite value for $T < T_C$.

A **type I** superconductor experiences zero magnetic field in the bulk for $H < H_C$ and $T < T_C$ [39]. A **type II** superconductor experiences zero magnetic field in the bulk for $H < H_{C1}$, and a mixed (normal and superconducting state) for $H_{C1} < H < H_{C2}$ [39][2]. The temperature dependence of the critical fields is compared for a **type I** and **type II** superconductor in Figure 2.1. The magnetization as a function of applied magnetic field below T_C is compared for a **type I** and **type II** superconductor in Figure 2.2.

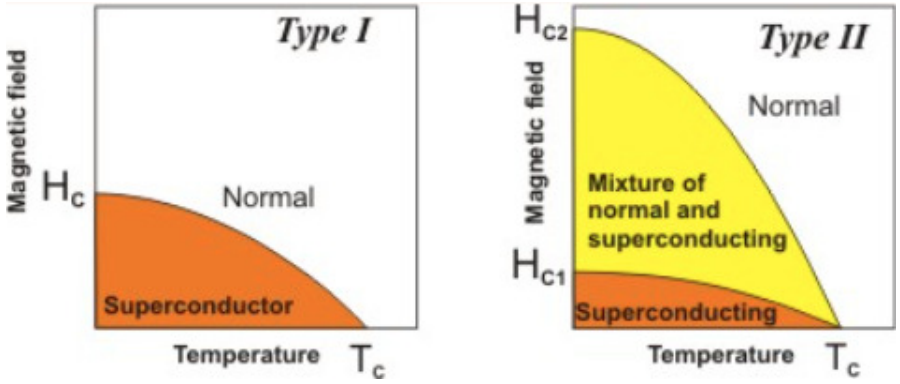

Figure 2.1: The difference between a **Type 1** (left mage) and **Type 2** (right image) superconductor (applied magnetic field as a function of temperature). Image taken from [41].

[2]In this regime the external magnetic field H partially penetrates the bulk of the superconductor [39].

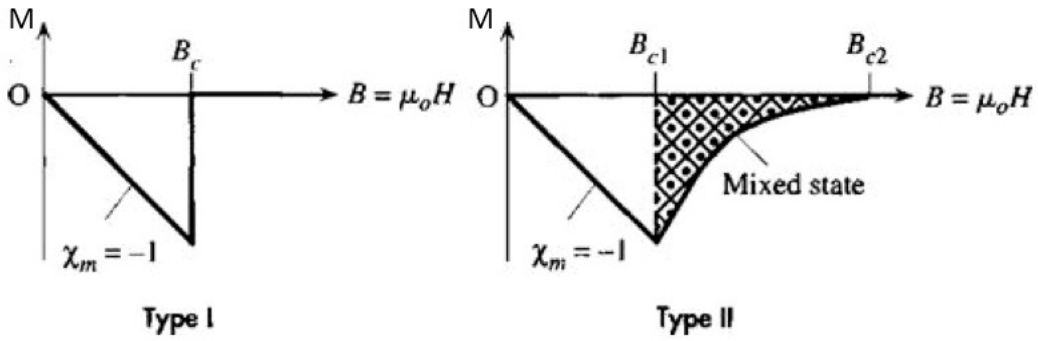

Figure 2.2: The difference between a **Type 1** (left image) and **Type 2** (right image) superconductor below T_C (magnetization as a function of applied magnetic field). Image taken from [42].

The **superconducting volume fraction** V_{sc} is the percentage of a sample that is superconducting. It is explained in detail in the following references [43, 44]. To find this parameter one must do a **field cooling** (FC) and a **zero field cooling** (ZFC) susceptibility measurement [43, 44]. An example of both these types of measurements will be outlined below and can be seen in Figure 2.3.

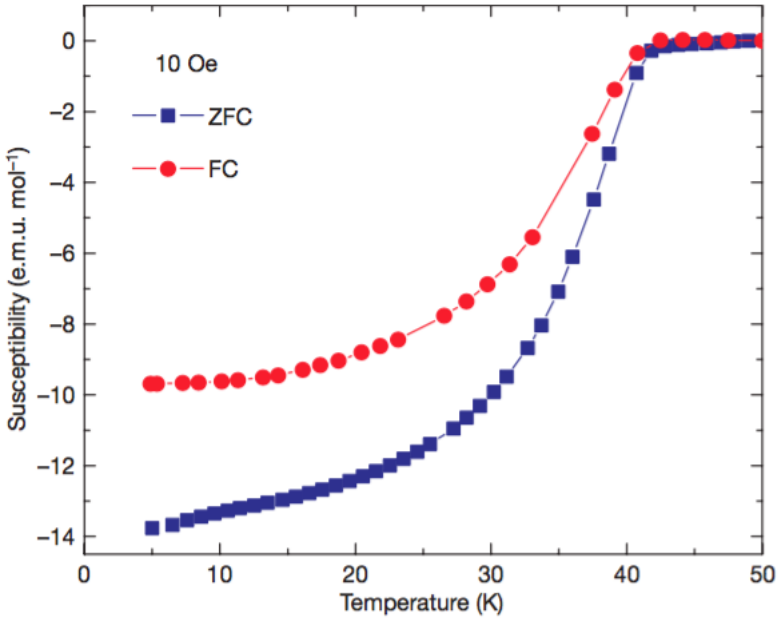

Figure 2.3: **FC**, **ZFC** measurements of susceptibility as a function of temperature for polycrystalline superconducting $SmFeAsO_{1-x}F_x$ where $x = 0.15$ with an external field of $H = 10$ Oe. The sample has a $T_C = 43$K. Notice how the FC curve is *more paramagnetic* than the ZFC curve for the same value of T. Image taken from [45].

In a **FC** measurement, one turns on a small magnetic field ($H < H_C$) above the material's T_C and then lowers the temperature below T_C while measuring the magnetization $\mathcal{M}(T)$ [44]. In this scenario the conducting part of the sample (assuming some of your sample is a conductor) preserves the initial field (i.e. a paramagnetic contribution) for $T < T_C$, this reduces the total diamagnetic response of the superconductor [39, 44]. Furthermore, the defects inside of a sample act to 'pin' magnetic flux lines so that they aren't fully expelled in the superconducting state (further reducing the measured diamagnetic response of

the material) [44]. In a **ZFC** measurement, one cools the sample down to $T < T_c$ in zero field and then turns on a small magnetic field ($H < H_C$). $\mathcal{M}$ is then measured while sweeping the sample temperature from $T < T_C$ to $T > T_C$ [44]. When the field $H < H_C$ is turned on from $H = 0$ below T_C, the conducting part of the sample will act to preserve the initial field (i.e. $H = 0$) and will give a diamagnetic contribution to the response of the sample. Therefore, the FC $\mathcal{M}$ is always *more paramagnetic* than the ZFC $\mathcal{M}$ at the same value of T [44].

We can obtain an approximate upper and lower bound to V_{sc} by extrapolation of a common temperature point T (below T_C) on the ZFC and FC curves [43], respectively. A material that is 100% superconducting will create screening currents and completely expel any magnetic field from the bulk [39]. Hence, the magnetic field inside of a material that is 100% superconducting is expressed as (cgs units)

$$\left|\vec{B}\right| = \left|\vec{H}\right| + 4\pi \left|\vec{\mathcal{M}}\right| = 0 \quad \Longrightarrow \frac{\mathcal{M}}{H} = \frac{-1}{4\pi}. \tag{2.1}$$

We know that $\mathcal{M} = \chi^{cgs} H$, where χ^{cgs} is the magnetic susceptibility in cgs units. Hence, V_{sc} (cgs) is approximately[3] equal to [47]

$$Vsc \simeq \left|\frac{4\pi\mathcal{M}}{H}\right| \tag{2.2}$$

where H is the applied field, $\mathcal{M}$ is the magnetization (both expressed in cgs). Therefore the **upper bound superconducting volume fraction** $V_{sc,upper}$ and

[3] neglecting demagnetization factor which is a sufficient assumption for small applied fields [46].

the **lower bound superconducting volume fraction** $V_{sc,lower}$ are given by

$$V_{sc,upper} \simeq \frac{4\pi \left|\mathcal{M}_{ZFC}(T)\right|}{H}, \tag{2.3}$$

$$V_{sc,lower} \simeq \frac{4\pi \left|\mathcal{M}_{FC}(T)\right|}{H}, \tag{2.4}$$

where $M_{ZFC}(T)$ is the magnetization of the ZFC curve at temperature[4] T (in cgs), H is the applied field[5] (in cgs) and $M_{FC}(T)$ is the magnetization of the FC curve at temperature T (in cgs). For a more accurate approach to finding V_{sc} one can follow the arguments in references [48, 49].

We will now briefly summarize a Luttinger liquid LL and charge density wave CDW and explain how both models relate to LiPB.

[4] $T < T_C$ is measured at the lower temperatures where ZFC and FC curves are approximately horizontal.

[5] This value is the same for the FC and ZFC curves.

2.2 Luttinger Liquid (LL)

The Wiedemann-Franz (WF) law states that the ratio of thermal conductivity K of a metal to the electrical conductivity σ and the absolute temperature T is equal to a constant (i.e. $K/\sigma T$=constant) [50]. An anomalous behaviour of LiPB is its deviation from the Wiedemann-Franz law [14]. This observation lead scientists to propose the Luttinger Liquid (LL) as a viable explanation for the $\sim$25K M/I transition [14]. One can describe a LL by various characteristics such as special features in the spectral function [51], strong electron correlation[6], low-dimensionality, zero conductance at low temperature, and spin-charge separation.

The spectral function $A(\mathbf{k}, \omega)$ is used in many-body physics to describe interacting systems, and contains the information proportional to the imaginary part of the single-particle retarded Green function [53]. $A(\mathbf{k}, \omega)$ can be measured by angle-resolved photo-emission spectroscopy (ARPES) [54]. The complication arises in quasi one-dimensional (q-1D) conductors. Since many q-1D conductors exhibit CDW fluctuations above the CDW transition temperature, this effect can allow $A(\mathbf{k}, \omega)$ to display trends which are very similar to that of a LL [54]. In general, the spectral function will show a peak around the Fermi energy E_F for a Fermi liquid (FL) and LL [55]. The spectral function must be summed over $\vec{k}$ to distinguish between the FL and LL (The LL fits a power law at the onset of the peak at E_F) [55, 56].

[6]The LL model takes into account interaction between fermions [52].

$Li_{0.9}Mo_6O_{17}$ single crystals (grown by the temperature gradient flux technique) were studied using ARPES, the results agree very well with the LL spectral function [56]. It was found that at photon energies of $h\nu$=500 eV and 30 eV the maximum in the momentum integrated spectrum peaks near the Fermi energy and hence may be described by a LL [56]. Furthermore, the fit parameters for 500 eV and 30 eV do not vary considerably [56]. Therefore, LL ARPES data is valid for the bulk and not just constrained to the surface of LiPB [56].

Low dimensionality (or a low-dimensional conductor) is a material where the electrons move only in a two-dimensional plane (as in $Na_{0.9}Mo_6O_{17}$ and $K_{0.9}Mo_6O_{17}$ [57]) or a one dimensional line (as in $Li_{0.9}Mo_6O_{17}$). One can clearly see the one-dimensional conductivity of $Li_{0.9}Mo_6O_{17}$ in Figure 1.1 [18], because $\rho_b(T) \sim \rho_a(T)/100 \sim \rho_c(T)/2000$. Furthermore, in non-superconducting $Li_{0.9}Mo_6O_{17}$, below ∼25K the electrical conductance approaches zero as T→0K (see Figure 1.2) [1], this effect supports the LL model [51].

Spin-charge separation occurs in a one-dimensional system and is characterized by the splitting of electron spin and electron charge into two different waves as predicted by the LL theory. These waves travel at different speeds and are confirmed using an electrostatically gated[7] 1D apparatus [59]. Spin charge separation has been observed in $Li_{0.9}Mo_6O_{17}$ which further supports the LL theory [60].

[7]Electrostatic gating is a method which alters the electric and magnetic properties of a material leading to a controlled carrier density. The main benefit of electrostatic gating is that the carrier density can be controlled without introducing impurities in the crystal lattice through doping [58].

2.3 Charge Density Wave (CDW)

Interestingly, in most cases depending on how $Li_{0.9}Mo_6O_{17}$ is grown, the measurement of ARPES returns two very different results [61]. On one hand the ARPES data for electrolytic reduction samples returns the $\vec{k}$ integrated spectral function with a power law opening up at E_F and hence describes a LL [54, 61]. On the other hand the samples prepared using temperature gradient flux technique report ARPES data with Fermi liquid FL behaviour [61, 62]. Furthermore, quasi one dimensional conductors tend to display a charge density wave (CDW) which shows similar properties in $A(\mathbf{k}, \omega)$ as the LL [54]. The CDW was first predicted to be the cause of lowered electronic energy in 1D metals [63]. The CDW was later experimentally verified in quasi-low dimensional compounds such as $(TaSe_4)_2I$, TaS_2, $TaSe_2$ and $NbSe_3$ [64, 65]. A CDW can be classified by an abnormal transition in the temperature dependence of the specific heat or magnetic susceptibility [28]. Furthermore, it can be detected by a M/I transition in the resistivity as a function of temperature measurement and variation in the X-ray diffraction (XRD) data above and below the CDW transition temperature [28].

The main feature describing a CDW is the Peierls Transition. A Peierls transition is energetically favourable in lower dimensional systems at low temperatures because the electrons are typically confined to one-dimensional chains [66, 67]. A Peierls transition shows up as the opening of an energy gap at the Fermi energy at temperature T_P [67]. We define $k_{\|}$ as the component of the

electronic wavevector along the conducting chains, where the reciprocal lattice vector $G_{\|} = 2\pi/b^*$ is the zone boundary [8] [65]. For an ideal 1D conductor, the components of the electronic wavevector perpendicular to the 1D conducting chains do not contribute to energy inside of the zone boundary [65]. Hence, The Fermi surface is composed of planes perpendicular to $k_{\|} = \pm k_F$ (i.e. the Fermi wave vector is pointing in the direction of the conducting chains) [65]. At low temperatures the 1D lattice will modulate and it will be energetically more favourable for two adjacent atoms to cluster [66], thereby opening up an energy gap at $k_{\|} = \pm k_F$.

There is a small peak in the specific heat for $Li_{0.9}Mo_6O_{17}$ from 22-34K which is the location of the resistivity upturn [68]. This coupled with the fact that $K_{0.9}Mo_6O_{17}$ is a known CDW at $T_P \sim 120$K which exhibits a resistivity upturn and peak in the specific heat [8] suggests the possibility of $Li_{0.9}Mo_6O_{17}$ exhibiting CDW behaviour [8]. The Fermi surface (see Figure 2.4) consists of two partially filled d-block bands originating from the Mo_4O_{18} chains[9] [69]. In Figure 2.4, $\Gamma = (0, 0, 0)$, $X = (\tilde{c}/2, 0, 0)$ and $Y = (0, \tilde{b}/2, 0)$, where $\tilde{c}$ is related to the lattice spacing between adjacent atoms along the c-crystallographic axis and $\tilde{b}$ is related to the spacing between successive Mo(1)-Mo(1) and Mo(4)-Mo(4) atoms along the b-crystallographic axis. The shaded regions depict the occupied electronic states and the unshaded regions depict the unoccupied electronic states. XRD has not uncovered the existence of a structural instability in LiPB at the

[8] For LiPB b^*=5.52$\mathring{A}$ is the spacing between successive Mo(1)-Mo(1) and Mo(4)-Mo(4) atoms along the b-crystallographic axis (spacing checked with Jmol).

[9] These Mo_4O_{18} chains are the Mo(1)-O(11)-Mo(4)-O(11) conducting chains described in Figure 1.3 [21, 69]. See Figure 1 in reference [69] for details.

temperature corresponding to the M/I transition (∼25K) [28].

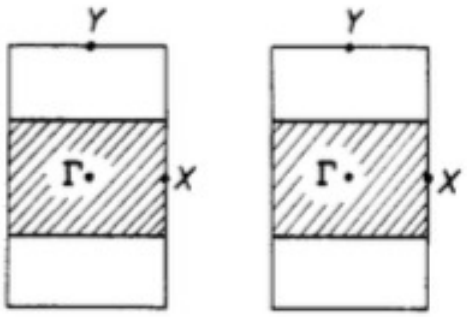

Figure 2.4: Schematic representation of the two identical Fermi surfaces of LiPB represented by the boundaries between the shaded and unshaded regions. Figure taken from [69].

Chapter 3

Methods: Crystal Growth

3.1 Oven calibration

The emphasis of this work was on the growth of single crystals. Two ovens were used for all single crystal growths[1]. Both ovens are three zone Lindberg ovens and use Omegaette CN4000 temperature controllers. These temperature controllers were calibrated before crystal growth. All values in the system parameter table for each temperature controller were set equal to one another[2]. Before the crystal growth was started both ovens were calibrated using a Eurotherm thermocouple. The thermocouple tip was placed in a large beaker of ice water and stirred continuously for 5 minutes. After 5 minutes the reading of the display fluctuated between 0.6-0.7^{o}C$\pm$0.1^{o}C.

[1] A Lindberg Blue single zone box furnace was used in the polycrystalline rubidium doped molybdenum dioxide growth discussed at the end of Chapter 3.6.

[2] Each temperature controller has 53 parameters which affect the output temperature, duty cycle output power, and various warning alarms [70].

Calibration of the oven temperature was performed in order to closely resemble the distributions found in [9]. To do this, the Eurotherm thermocouple tip was placed at the hot zone which is directly above the central oven thermocouple by about ∼3 cm (see Figure 3.1 **bottom centre picture**) and the oven was turned on. Once steady state temperature was reached, the thermocouple was moved through ≃ 20cm of the oven in 1 cm intervals. The thermocouple was stopped at each centimetre and left for a certain time (≥2 minutes) to allow temperature to equilibrate. Figure 3.1 **top picture** shows the two cold zones and hot zone of oven 1. High temperature insulation was used on both ends of the oven. The upper cold zone was set to the same settings as the lower cold zone, but the ampoule was placed only in the lower cold zone and hot zone (see **bottom left picture**). This was done to create a more stable temperature gradient. Figure 3.1 **bottom right picture** shows how the back end of the thermocouple is flush with the backside of the brick at 0 cm (in this configuration the thermocouple tip is located above the central oven thermocouple as seen in Figure 3.1 **bottom centre picture**). This created a good reference allowing one to take accurate temperature distribution measurements with a metre stick.

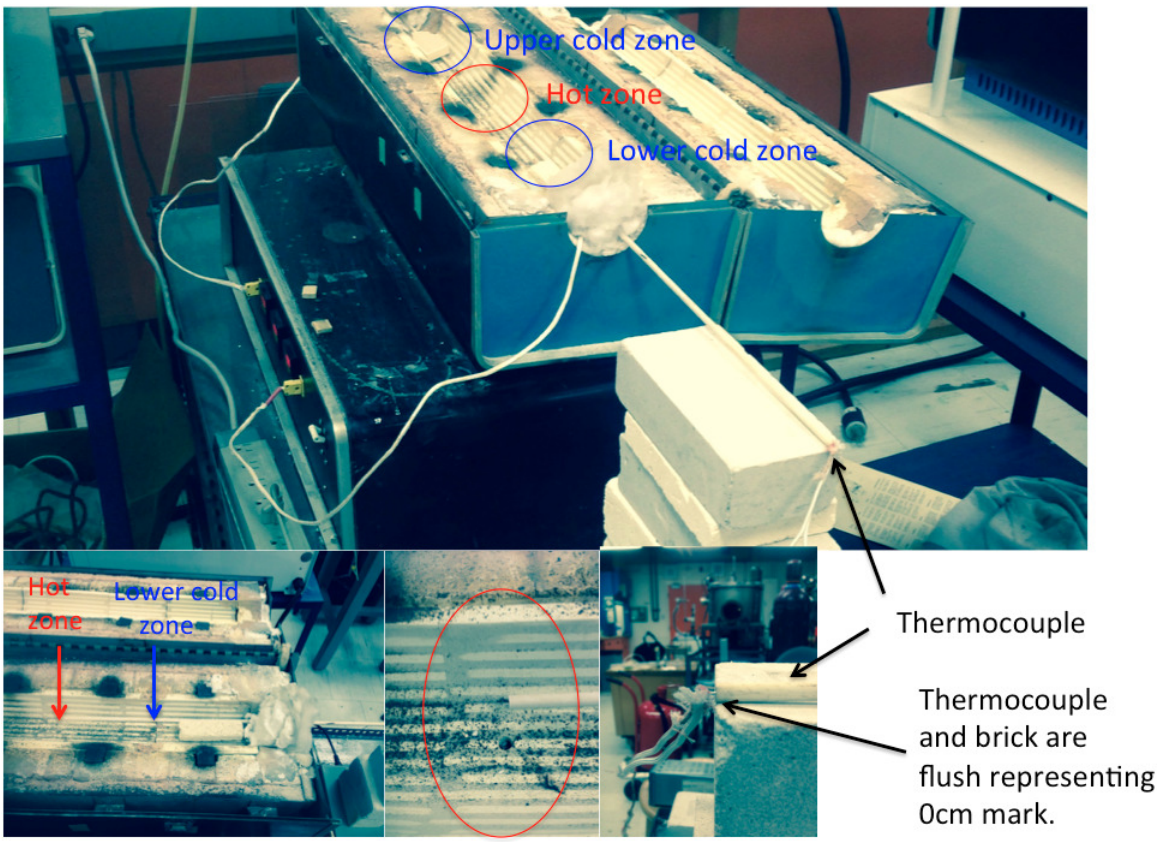

Figure 3.1: Temperature calibration for **oven 1**. Oven 2 was calibrated using the same method as oven 1.

Temperature calibration was performed for the preheat and crystal growth steps as seen in Figure 3.2. The horizontal line at 574^{o}C corresponds to the preheat temperature and is consistent across both zones, remaining fixed for typically 4 days.

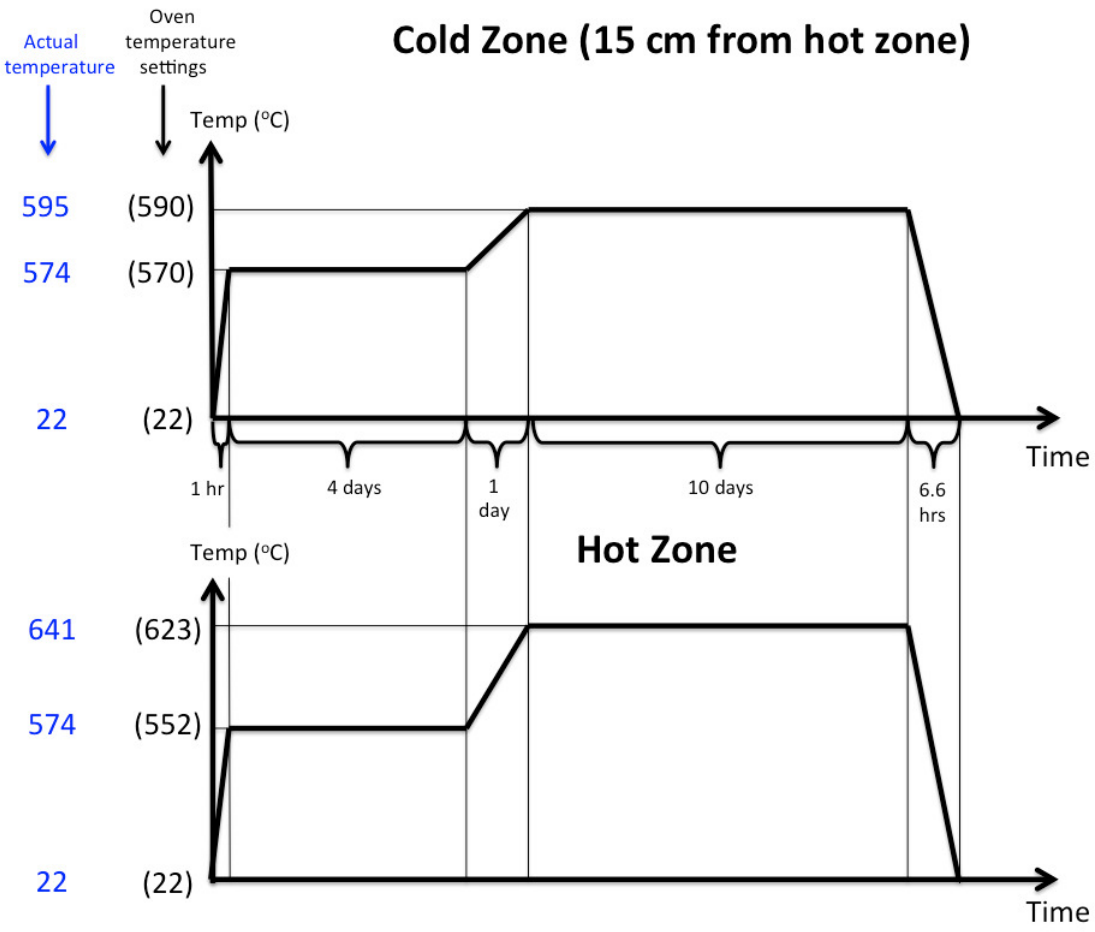

Figure 3.2: Temperature settings of the cold and hot zones as a function of time for **oven 2**. The hot zone is located at the oven's central thermocouple and the cold zone is located 15 cm from the hot zone.

The horizontal lines at 641^{o}C and 595^{o}C correspond to the crystal growth temperatures of the hot and cold zones, respectively. The crystal growth temperatures remain fixed for a duration of 10 days. The crystal growth timeline (Figure 3.2) was used for the following batches: I.26, I.31, I.33 and I.34. The temperature distributions for ovens 1 and 2 during the crystal growth step can be found in Tables 3.1 and 3.2, respectively.

Table 3.1: True temperature distribution (i.e. the temperature measured by the Eurotherm thermocouple) of **oven 1** as measured from the hot zone. The hot zone (central oven thermocouple) was set to 614^{o}C and the two cold zones (outer oven thermocouples) were set to 606^{o}C. This distribution was used for the 10 day constant temperature setting of the oven during the crystal growth step.

Distance of thermocouple tip from hot zone (cm)	Temperature of Eurotherm Thermocouple (^{o}C)	Time interval required for thermocouple to reach steady state (seconds)	Change in temperature (^{o}C)
0	644.8	/	/
1	644.5	120	0.3
2	644.1	120	0.4
3	643.5	120	0.6
4	642.9	120	0.6
5	641.7	120	1.2
6	640.4	120	1.3
7	638.8	120	1.6
8	636.6	120	2.2
9	634.1	120	2.5
10	631.1	120	3
11	627.7	120	3.4
12	624.0	120	3.7
13	619.8	120	4.2
14	615.0	150	4.8
15	609.9	150	5.1
16	605.3	150	4.6
17	602.1	150	3.2
18	598.7	150	3.4
19	594.0	180	4.7
20	587.5	180	6.5

Table 3.2: True temperature distribution (i.e. the temperature measured by the Eurotherm thermocouple) of **oven 2** as measured from the hot zone. The hot zone (central oven thermocouple) was set to 623^{o}C and the two cold zones (outer oven thermocouples) were set to 590^{o}C (see the 10 day time interval in Figure 3.2 for details). This distribution was used for the ten day constant temperature setting of the oven during the crystal growth step.

Distance of thermocouple tip from hot zone (cm)	Temperature of Eurotherm Thermocouple (^{o}C)	Time interval required for thermocouple to reach steady state (seconds)	Change in temperature (^{o}C)
0	641.3	/	/
1	641.3	120	0
2	641.0	120	0.3
3	640.2	120	0.8
4	639.0	120	1.2
5	636.9	120	2.1
6	634.5	240	2.4
7	631.7	480	2.8
8	628.5	540	3.2
9	625.0	360	3.5
10	621.0	300	4
11	616.7	300	4.3
12	611.9	360	4.8
13	606.0	720	5.9
14	600.4	600	5.6
15	594.6	600	5.8
16	589.3	540	5.3
17	584.9	300	4.4
18	580.7	660	4.2
19	576.5	360	4.2
20	572.7	660	3.8

To obtain high quality single crystals, one must use a preheat temperature in the temperature range 550-580 ^{o}C [9]. Table 3.3 is an example of the preheat temperature distributions for oven 2 (a similar distribution was recorded for oven 1). The thermocouple was placed in the centre of the oven and the oven was allowed to stabilize before the distribution was recorded. The thermocouple was moved in 2 cm intervals allowing temperature equilibrium to occur before recording the data.

Table 3.3: True temperature distribution (i.e. the temperature measured by the Eurotherm thermocouple) of **oven 2** as measured from the hot zone. The hot zone (central oven thermocouple) was set to 552^{o}C and the two cold zones (outer oven thermocouples) were set to 570^{o}C (see the 4 day time interval in Figure 3.2 for details). This distribution was used for the preheat temperature setting (lasting 3 or 4 days).

Distance of thermocouple tip from hot zone (cm)	Temperature of Eurotherm Thermocouple (^{o}C)	Time interval required for thermocouple to reach steady state (seconds)
0	573.5	/
2	574.2	420
4	574.5	540
6	574.1	420
8	573.6	540
10	573.8	780
12	573.5	360
14	573.3	840
16	574.7	600
18	576.4	720
20	576.1	480

3.2 Temperature Gradient Flux Technique: Single crystal $Li_{0.9}Mo_6O_{17}$

All single crystals were grown inside quartz ampoules (o.d.[3] 12 mm and i.d.[4] 10 mm) which were thoroughly cleaned with aqua regia before use. Most ampoules were heated to 800 ^{o}C in a furnace before adding the sample. The ampoules were then flamed lightly twice with sample inside before seal-off. In this section, all purple bronze crystals were grown according to [9], using the chemical equation given by:

$$nA_2MoO_4 + 2(1-n)MoO_3 + nMoO_2 \rightarrow 2A_nMoO_3 \quad ; \; A = Li, Na, K, Rb. \tag{3.1}$$

Example Calculation for Li

The amount of each compound can be calculated for general doping parameter n using the following definitions,

$m_{Li_nMoO_3} \equiv mass\ of\ Li_nMoO_3$,

$m_{Li_2MoO_4} \equiv mass\ of\ Li_2MoO_4$,

$m_{MoO_3} \equiv mass\ of\ MoO_3$,

$m_{MoO_2} \equiv mass\ of\ MoO_2$,

$n_{Li_nMoO_3} \equiv moles\ of\ Li_nMoO_3$,

$n_{Li_2MoO_4} \equiv moles\ of\ Li_2MoO_4$,

[3]Stands for 'outer diameter'.
[4]Stands for 'inner diameter'.

$n_{MoO_3} \equiv moles\ of\ MoO_3$,

$n_{MoO_2} \equiv moles\ of\ MoO_2$,

$M_{Li} \equiv molar\ mass\ of\ Li$,

$M_{Mo} \equiv molar\ mass\ of\ Mo$,

$M_O \equiv molar\ mass\ of\ O$,

$M_{Li_nMoO_3} \equiv molar\ mass\ of\ Li_nMoO_3$,

$M_{Li_2MoO_4} \equiv molar\ mass\ of\ Li_2MoO_4$,

$M_{MoO_3} \equiv molar\ mass\ of\ MoO_3$,

$M_{MoO_2} \equiv molar\ mass\ of\ MoO_2$.

Using the above parameters and equation 3.1 the following equations are obtained for the masses of the starting compounds:

$$m_{Li_2MoO_4} = \frac{n \cdot m_{Li_nMoO_3}}{2 \cdot M_{Li_nMoO_3}} M_{Li_2MoO_4}, \tag{3.2}$$

$$m_{MoO_3} = (1-n) \cdot \frac{m_{Li_nMoO_3}}{M_{Li_nMoO_3}} M_{MoO_3}, \tag{3.3}$$

$$m_{MoO_2} = \frac{n \cdot m_{Li_nMoO_3}}{2 \cdot M_{Li_nMoO_3}} M_{MoO_2}. \tag{3.4}$$

Consider *doping parameter* n=0.33

All of the elemental molar masses were taken directly from the appendix in [71], the stable isotopes were averaged and weighted in terms of natural abundance to obtain the average molar mass of each element. Finding the molar masses of the separate compounds, we obtain

$$M_{Li_{0.33}MoO_3} = 0.33M_{Li} + M_{Mo} + 3M_O = 146.2188\frac{g}{mol}, \tag{3.5}$$

$$M_{Li_2MoO_4} = 2M_{Li} + M_{Mo} + 4M_O = 173.8091\frac{g}{mol}, \tag{3.6}$$

$$M_{MoO_3} = M_{Mo} + 3M_O = 143.9282\frac{g}{mol}, \tag{3.7}$$

$$M_{MoO_2} = M_{Mo} + 2M_O = 127.9293\frac{g}{mol}. \tag{3.8}$$

Finally, substituting the above into equations (3.2), (3.3) and (3.4), (using the fact that the final charge should weigh $m_{Li_nMoO_3} = 10g$), we obtain the starting compound masses

$$\boxed{m_{Li_2MoO_4} = 1.9613g \quad ,} \tag{3.9}$$

$$\boxed{m_{MoO_3} = 6.5950g \quad ,} \tag{3.10}$$

$$\boxed{m_{MoO_2} = 1.4436g \quad .} \tag{3.11}$$

These masses were used in the crystal growth for sample I.33 (see Table 3.4 for more complete growth details of this sample). All lithium samples in Table 3.4 were grown using the above method. In addition, the samples II.33_{Na}, III.33_{Rb} and IV.33_K in Table 3.6 were also grown using the above method. The sample I.05_{Rb} is a polycrystalline sample and was grown using a different method. The growth method of I.05_{Rb} will be briefly discussed in Chapter 3.6. The temperature gradient flux technique will be explained in further detail in the next section.

3.3 Temperature Gradient Flux Technique

Temperature gradient flux technique is a method of single crystal growth where a temperature gradient is applied across an evacuated, sealed quartz ampoule [9]. This method is a special case of vapour transport, where a melt is used as the transport agent instead of a gas [72]. This method of crystal growth can be described in three steps (illustrated in Figure 3.3):

1. **Preheat step:** The compressed powder, which has been pressed into tablets, fuses together and the space between particles becomes smaller [72].

2. **Diffusion step:** The sample melts and the liquid flux diffuses to the cold zone (located ∼15 cm from hot zone)[5].

3. **Crystal growth step:** Crystal growth in the cold zone and throughout the flux.

[5]The **diffusion step** (and hence the **crystal growth step**) does not always occur (i.e. no melting). In this case the compound only becomes sintered and as a result single crystal LiPB does not form. The reason why some mixtures do not melt is because the eutectic melting point is too high for these molar ratios (discussed below). Visible melting occurred in the following samples: I.33, I.34, $II.33_{Na}$, $III.33_{Rb}$, $IV.33_{K}$.

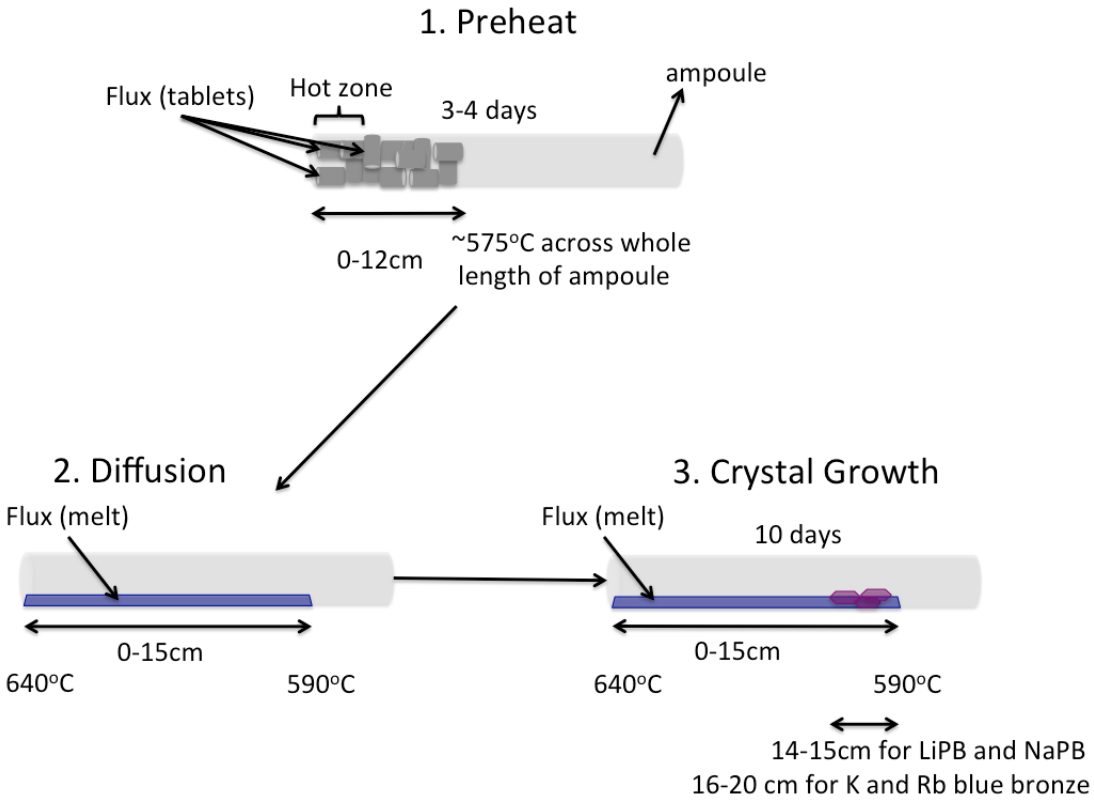

Figure 3.3: The crystal growth steps involved in the temperature gradient flux technique.

The single crystal $Li_{0.9}Mo_6O_{17}$ (LiPB) is grown by the temperature gradient flux technique. A temperature gradient ΔT was created over the first 20 cm of the ampoule ($580^oC \leq \Delta T \leq 640^oC$). The starting compounds were high purity[6] Li_2MoO_4 (m.p. 705 ^{o}C), MoO_3 (m.p. 795 ^{o}C) and MoO_2 (m.p. $\sim$1,200 ^{o}C [73]) which were dried at 160^oC, mixed thoroughly and ground into powder[7].

The powder was then pressed into 5mm diameter tablets[8] (double pressed) before being sealed in a quartz ampoule. During tablet compression, methanol was used as lubricant[9] but later this was switched to petroleum ether due to the solubility of the starting compounds in methanol. In both cases the tablets were dried at 100^{o}C after tablet compression to evaporate any excess lubricant before crystal growth. For all crystal growths the charge was placed in the bottom rounded section of the ampoule which was later placed in the hot zone of the oven. The tablets extended 12 cm from the hot zone in most cases. After growth, all samples were leached in $\sim$2M HCl solution (HCl was diluted with distilled water) and hot sodium phosphate mono-basic dissolved in distilled water. The sample was alternated between both acidic and salt solutions and kept in each solution for several hours until the solution appeared clear and colourless. This step is necessary in order to extract high quality single crystals.

[6] See section 3.4 for starting compound purities of each growth.

[7] It is known that MoO_3 reduces to MoO_2 in a hydrogen gas environment at high temperatures [34], however this temperature was not high enough to cause significant reduction (a slight change in colour of MoO_3 was noted over time) and drying MoO_3 at 160^oC is standard practice [9].

[8] Sample I.29 was not pressed into tablets. Sample I.30 was pressed into 3 tablets, the remaining sample was powder.

[9] Lubricant is needed in order to maintain the structural integrity of the tablet while it is being removed from the inner bore. If lubricant isn't used, then the tablet may break into pieces upon removal from the inner bore.

There is equal number of moles of Li_2MoO_4 and MoO_2. Looking at the mass ratios of each starting compound, we see that $m_{MoO_2} : m_{Li_2MoO_4}$ is roughly $0.74 : 1$ (for $0.26 \leq n \leq 0.34$). $m_{MoO_2} : m_{MoO_3}$ is $0.23 : 1$ for $n = 0.34$ and monotonically decreases with decreasing *doping parameter* n to $0.16 : 1$ for $n = 0.26$. Hence, MoO_2 is the least abundant starting compound by mass compared to the other two compounds for the $0.26 \leq n \leq 0.34$ doping range. Furthermore, MoO_2 melts at temperatures much higher than the working temperature of the oven ($\sim 1200^o$C). This is important because in order to create a melt which extends to the cold zone, we need to find the proper doping ratios of molybdenum trioxide, molybdenum dioxide and lithium molybdate so that the melting eutectic point is established around $\sim 590^o$C. Since molybdenum dioxide is least abundant, we will focus attention on the eutectic point of Li_2MoO_4 and MoO_3 (see[10] Figure 3.4). In this figure the red region represents the n dopings which didn't produced high quality LiPB crystals (i.e., n=0.26, 0.28 and 0.29), the yellow region represents n dopings which produced good quality LiPB crystals (i.e. n=0.30, 0.33 and 0.34). For more information on each growth see Table 3.5.

[10]Figure taken and adapted from [74].

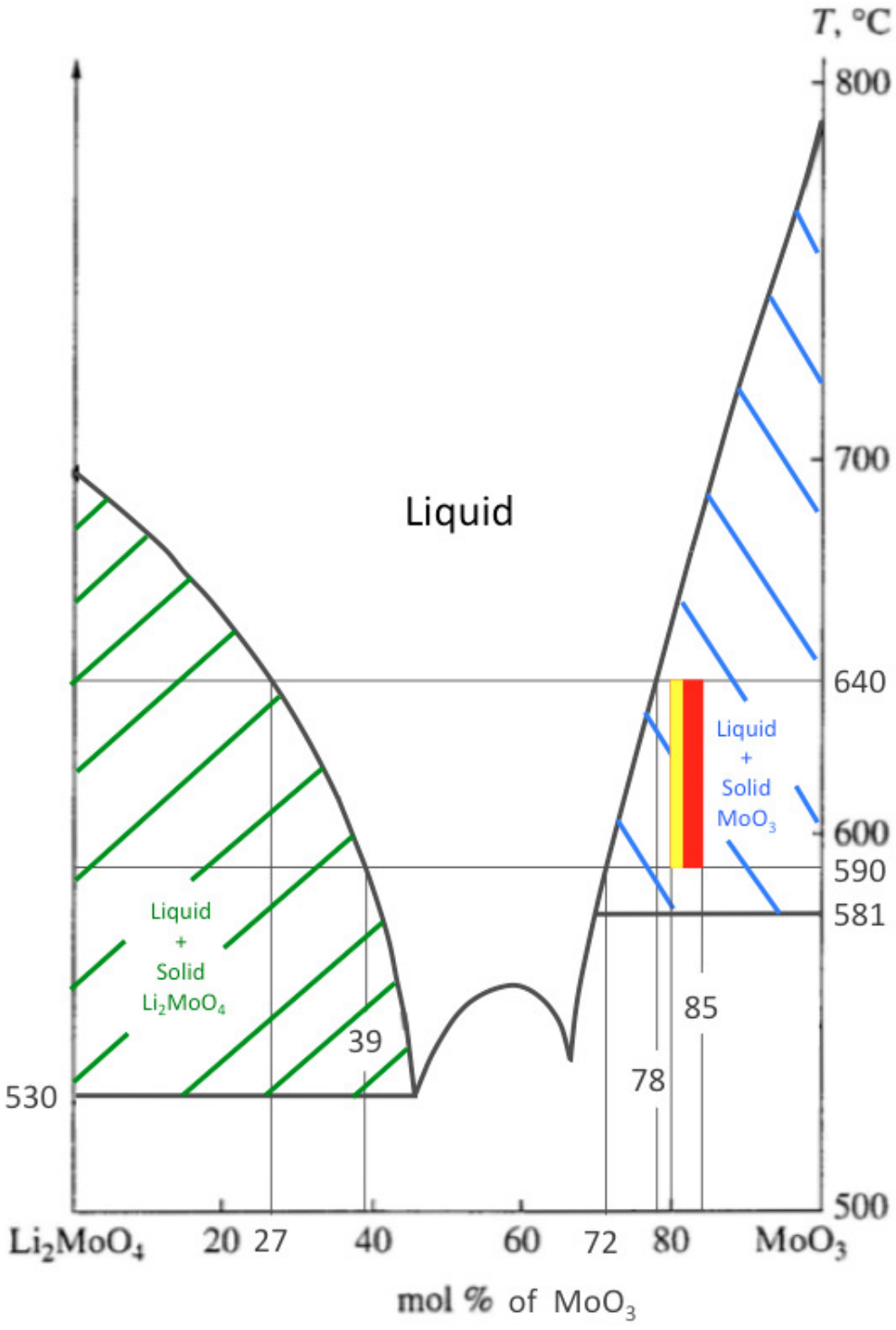

Figure 3.4: Phase diagram of lithium molybdate and molybdenum trioxide.

3.3.1 Nucleation and crystal growth

Nucleation and crystal growth will be discussed in detail below. Nucleation is the creation of a solid phase from a liquid phase[11], which occurs because the free energy of the solid phase is lower than that of the liquid phase. In classical nucleation theory, the nucleation rate (nuclei per unit volume per second) is given by the following equation [72]

$$I \propto e^{\frac{-\Delta G}{k_B T}}, \tag{3.12}$$

where k_B is the Boltzmann constant, T is the temperature and ΔG is given by [75]

$$\Delta G = \Delta G_B + \Delta G_S = \frac{4}{3}\pi r^3 \Delta G_V + 4\pi r^2 \gamma. \tag{3.13}$$

ΔG_B, the free energy of the bulk, is the change in a system's free energy due to the formation of a single crystalline nucleus in the melt[12]. ΔG_S is the free energy change associated with diffusion across the liquid/nucleus interface. In equation (3.13), ΔG_B and ΔG_S are expressed in terms of a spherical nucleus of radius r. γ, the interfacial free energy (a positive constant), is the energy at the crystal/melt interface and ΔG_V is the difference in free energy of the melt phase compared to the nucleating phase per unit volume. ΔG_V is negative because the crystallization phase has a lower free energy than the melt. For small r, the

[11] Hence, nucleation is a first order phase transition.
[12] ΔG_B is called the *thermodynamic barrier to nucleation.*

crystalline nucleus is small and hence $4\pi r^2\gamma$ dominates, this leads to an increase in free energy with increasing r and hence the nucleus will either dissolve or melt. Once $r = r_c$, the bulk term $\frac{4}{3}\pi r^3 \Delta G_V$ begins to dominate leading to a maximum in $\Delta G(r_c) = \Delta G_c$, hence the nucleus is stable at r_c. For $r > r_c$ (which occurs by statistical means) the free energy of the nucleus ΔG begins to decrease with increasing r and hence the nucleus crystallizes (Figure 3.5).

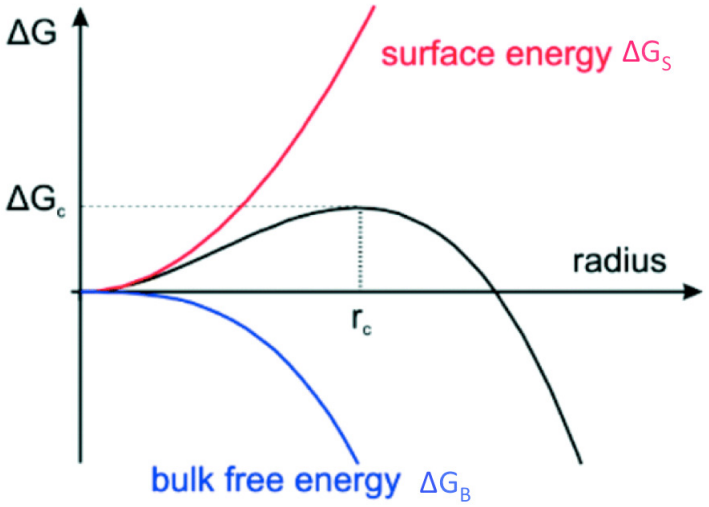

Figure 3.5: Contributions of the surface free energy $\Delta G_S = 4\pi r^2\gamma$ and the free energy of the bulk $\Delta G_B = \frac{4}{3}\pi r^3 \Delta G_V$ to the free energy for the creation of a nucleus ΔG. Figure taken from [76].

The presence of a solid in the melt (i.e. the ampoule wall) may also affect the $4\pi r^2\gamma$ term and ultimately alter the form of equation (3.13). The interfacial free energy γ between the crystalline nucleus and a solid is a smaller positive number than the interfacial free energy between the crystalline nucleus and the melt [75]. Hence, it is more probable that nucleation will occur along the ampoule wall.

Generally, crystal growth is simpler than nucleation [77] and can occur at any temperature below T_m (the melting point of the crystal) as long as there are available nuclei. Specifically, the crystal growth rate is maximized at a slightly higher temperature than the maximum in the nucleation rate (see Figure 3.6). This occurs because the viscosity of the melt decreases with increasing temperature and hence macromolecule diffusion will become easier leading to an increased crystal growth rate [72, 77]. If the nucleation maximum and crystal growth maximum coincide or are close to one another in temperature then nucleation and crystal growth will occur simultaneously. In this case crystallization of the melt will occur with ease. Consider the nucleation maximum at a much lower temperature than the crystal growth maximum. In this case if the temperature is left at the corresponding maximum in nucleation and is not increased to the corresponding maximum in crystal growth then many nuclei will form but not grow into crystals and thus the melt will form a glass [72].

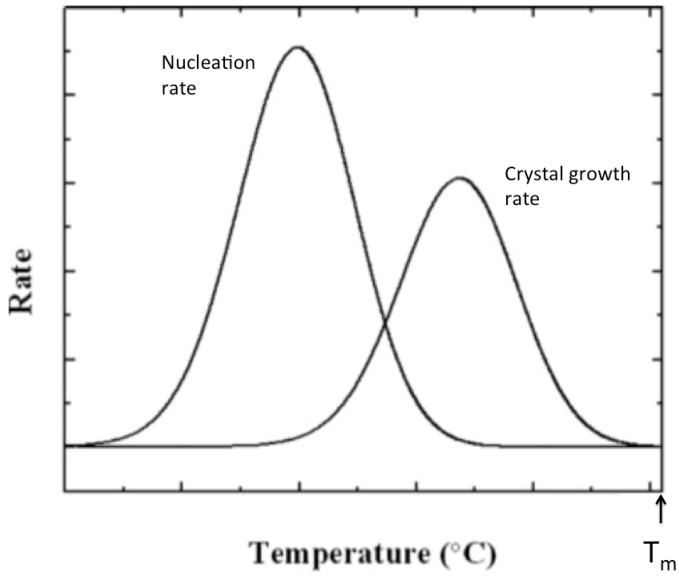

Figure 3.6: Comparison of the nucleation rate (i.e. equation (3.12)) with the crystal growth rate. The maximum nucleation rate occurs at a lower temperature than the maximum crystal growth rate because viscosity decreases at higher temperature which creates ideal conditions for transporting the required materials through the crystal/melt interface [72]. T_m is the temperature at which the crystallization phase melts. Figure taken from [77].

3.4 Growth parameters of each sample

This section will discuss the preparation and growth results of each sample which were prepared using the following chemical formula:

$$nLi_2MoO_4 + 2(1-n)MoO_3 + nMoO_2 \rightarrow 2Li_nMoO_3.$$

The goal was to obtain high quality single crystals of $Li_{0.9}Mo_6O_{17}$. The details that will be discussed include: starting compound purities, physical properties before and after crystal growth, charge length before crystal growth, ampoule total length[13], similarities and differences between samples, and any anomalous results or methodologies. The pregrowth conditions of each sample are outlined in Table 3.4 and the growth results of each sample are outlined in Table 3.5.

[13]Ampoule total length refers to the length from one end of the inner wall of the ampoule to the other end of the inner wall of the ampoule.

Table 3.4: Table organizing the growth parameters of each Lithium sample. t_i is the time duration of the **preheat step**. T_0, T_5, T_{10} and T_{15} are the oven temperatures during the **diffusion/crystal growth steps** for the distances 0cm, 5cm, 10cm and 15cm from the hot zone, respectively.

Sample	n	T_i in cold/ hot zones (^oC)	t_i	T_0 (^oC)	T_5 (^oC)	T_{10} (^oC)	T_{15} (^oC)	Ampoule pressure before seal-off (torr)	Made tablets?	Tablet Pressure range (metric tons mT)
I.26	0.26	595/641	4 days	641	637	621	595	10^{-5}	Yes (all)	0.9-1.3
I.28	0.28	610/645	4 days	645	642	631	610	10^{-5}	Yes (all)	0.9-1.1
I.29	0.29	610/645	3 days	645	642	631	610	10^{-7}	No	NA
I.30	0.30	610/645	3 days	645	642	631	610	10^{-8}	Yes (only 3)	0.3-0.5
I.31	0.31	595/641	4 days	641	637	621	595	10^{-2}-760	Yes (all)	0.7-0.9
I.33	0.33	595/641	4 days	641	637	621	595	10^{-6}	Yes (all)	0.3-0.5
I.34	0.34	595/641	4 days	641	637	621	595	10^{-5}	Yes (all)	0.9-1.3

Sample I.26:

pre-growth: Starting compounds had the following purities: 99.98% MoO_2, 99.99% Li_2MoO_4 and 99.9995% of MoO_3. The starting compounds were dried at a constant 160^{o}C for several days before use. This sample was pressed into tablets in the pressure range 0.9- 1.3 mT (see Figure 3.7).

Figure 3.7: Tablets of sample I.26 (preoven).

The tablets were placed in 100^{o}C furnace overnight. The total length of the ampoule and charge after seal-off was ∼24cm and ∼14cm, respectively.

post-growth: Sample did not melt. Majority of crystals obtained are blue-grey spores and minority is bluish-purple black gold BPBG crystals. These BPBG crystals are identical in appearance to the ones obtained from samples I.28 and I.29. Furthermore, these BPBG crystals do not have visible orientation (i.e. they do not form visible planes) and are amorphously shaped. For more of an in-depth

physical description of these BPBG crystals, see I.28 post-growth. For characterization of the BPBG crystals see I.29 post-growth.

Sample I.28:

pre-growth: Starting compounds had the same purities as that of I.26. The starting compounds were dried at a constant 160^{o}C for several days before use. After the individual compounds were weighed out, they were ground continuously for 10 minutes with a mortar and pestle. This sample was pressed into tablets in the pressure range 0.9-1.1 mT. Once the tablets were pressed, the sample was put into the oven at 100^{o}C for $\sim$1 hour. The total length of the ampoule and charge after seal-off was $\sim$20cm and $\sim$16cm, respectively.

post-growth: Majority of sample does not appear to have melted because the individual tablets are still visible (see Figure 3.8) as well as the charge length remained constant before and after growth ($\sim$ 16cm). However, from Figure 3.8 it appears that the tablet located 3.5-4cm from the hot zone did slightly melt.

Figure 3.8: Sample I.28 (postoven and preleach). Hot zone is the leftmost side of the ampoule. Ticks on wooden ruler are in mm.

Primary phase crystals appear a bluish-purple colour on some surfaces and a gold black colour on other surfaces[14]. A trace amount of $Li_{0.9}Mo_6O_{17}$ crystals were obtained with average size of $2 \times 1 \times 0.5mm^3$ and no superconducting crystals were found.

[14] As opposed to a pure purple colour on the whole surface as is the case for LiPB single crystals.

Sample I.29:

pre-growth: Starting compounds had the following purities: 99% MoO_2, 99+% Li_2MoO_4 and 99.9995% of MoO_3. The starting compounds were not dried. Once the starting compounds were added to the mortar, they were immediately mixed with mortar and pestle and transferred to the ampoule via a glass funnel. The charge was then pumped on overnight. The ampoule was lightly flamed the next day with a natural gas and oxygen torch. The total length of the ampoule and charge after seal-off was ∼20cm and ∼8cm, respectively.

post-growth: The ampoule was cooled at a rate of 1.5^{o}C/min and quenched in cold water from $\simeq 525^oC$ (hot zone: 550^oC and cold zone: 500^oC). Sample appears to have melted but it is hard to be certain. A blue layer formed between the quartz ampoule and the charge. This material was confirmed by X-ray analysis[15] to be a mix of SiO_2, $Li_6Mo_2O_7$ and $Li_{0.91}MoO_3$. After leaching, the main phase crystals appeared a bluish-purple black gold BPBG colour on the surface[16]. Initially, these crystals appeared to be lithium purple bronze as they looked very purple in the leaching process (see Figure 3.9).

[15]The latest version of the program MATCH! [78] was used to characterize the material.
[16]As opposed to a shiny purple colour of pure lithium purple bronze crystals.

Figure 3.9: Leaching of sample I.29 in ∼2M HCl. Polycrystals appear purple and can be mistaken for LiPB.

The $\rho(T)$ curve of these crystals has similarities to that of potassium and sodium purple bronze [9]. After further analysis, the resistivity curves of these samples are nearly identical to $\eta - Mo_4O_{11}$ found in [3]. BPBG crystals were ground into a fine powder and measured using powder Bragg-Brentano X-ray diffraction and it was found[17] that the crystals have a composition of 62.6% $\eta - Mo_4O_{11}$, 21.6% $Li_{0.9}Mo_6O_{17}$ and 15.8% beta-quartz.

[17]The latest version of the program MATCH! [78] was used to characterize the sample.

Sample I.30:

pre-growth: Starting compounds had the same purities as that of I.29. The starting compounds were dried at a constant 160^{o}C for several days before use. This sample used both powder and three tablets pressed in the pressure range 0.3-0.5 mT. The powder was transferred into the ampoule via a glass funnel. The total length of the ampoule and charge after seal-off was ∼21cm and ∼13cm, respectively.

post-growth: The ampoule was cooled at a rate of 1.5^{o}C/min and then taken out of the oven at $\simeq 525^oC$ (hot zone: 550^oC and cold zone: 500^oC) and left to cool down to room temperature. Once the ampoule was broken and inspected, the sample seemed to have melted because visible tablets cannot be seen in the hardened flux (see Figure 3.10).

Figure 3.10: Crystal appearance of I.30 after oven and before leaching.

After leaching about 1/3 of the remaining phase was $Li_{0.9}Mo_6O_{17}$, which was confirmed by powder Bragg-Brentano X-ray diffraction. The single crystals appeared shiny and purple. The average dimensions of the single crystals was $\sim 2.5 \times 1 \times 0.5mm^3$. The resistivity as a function of temperature curves obtained by single crystal measurements matched the expected results for non-superconducting lithium purple bronze [1, 51]. Many of these crystals were non superconducting but a few had a confirmed superconducting transition at 2K.

Sample I.31:

pre-growth: Starting compounds had the same purities as that of I.26. The starting compounds were heated at a constant 160^{o}C for several days before use. After all compounds were put in the mortar, they were continuously mixed with pestle for ten minutes[18]. All tablets were pressed in the pressure range of 0.7- 0.9 mT. Before putting the tablets in the ampoule, they were put in a crucible and left at a constant 100^{o}C overnight. During seal-off there was a puncture in the wall of the upper quartz connector which may have increased the pressure in the ampoule. The total length of the ampoule and charge was ∼22cm and ∼14cm, respectively.

post-growth: Before the ampoule was broken, one could see some thin bar-shaped bluish grey crystals in the coldest region of the ampoule (see Figure 3.11 a). These crystals were confirmed to be $Li_2Mo_4O_{13}$ by powder XRD analysis[19]. Once the ampoule was broken it appears that some melting occurred within the first 4 centimetres of the hot zone. Possibly some melting occurred at the 14cm mark. Tablets are clearly still visible from 4-14cm of the ampoule. A visible purple crystal can be seen at the 8cm mark (see Figure 3.11 b). After leaching, purple crystals have an average size of $2 \times 2 \times 0.5mm^3$.

[18]This will further reduce the size of the powder, thereby increasing the surface area of the reactant compounds. Increased surface area will ensure more complete fusion of particles during the preheat step [72].

[19]The latest version of the program MATCH! [78] was used to characterize the material.

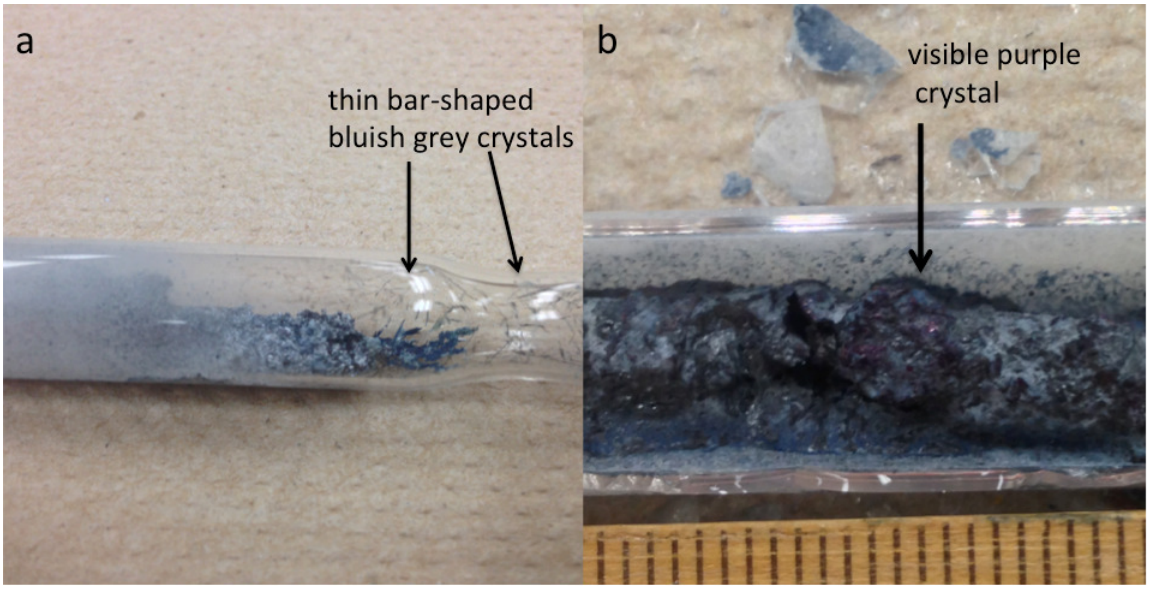

Figure 3.11: Sample I.31 postgrowth and preleach. **a)** Growth of spore crystals via oxygen transport in cold zone. **b)** Single visible purple crystal. Ticks on wooden ruler are in mm.

Sample I.33:

pregrowth: Starting compounds had the same purities as that of I.29. The starting compounds were heated at a constant 160^{o}C for several days before use. All tablets were pressed in the pressure range of 0.3-0.5 mT. Prior to seal-off, tablets and ampoule were torched lightly. After seal-off, the total length of the ampoule and charge was ∼20cm and ∼13cm, respectively.

postgrowth: The ampoule was cooled at a rate of 1.5^{o}C/min to room temperature. The tablets appeared to have melted because the charge covered a length of 15cm (as opposed to the pregrowth length of 13cm) as well as the presence of a visible contact angle between the top of the sample and bottom of quartz ampoule [79]. A large number of purple crystals appeared in the the cold zone (i.e. 14-15 cm from hot zone of the ampoule). Many large LiPB single crystals were formed (see Figure 3.12) with some being as large as 7mm in length.

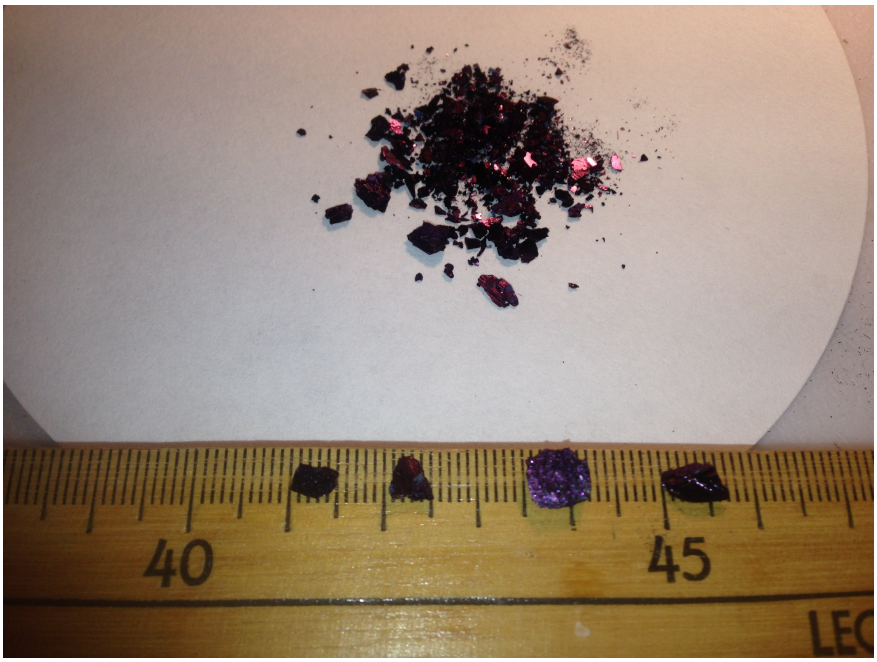

Figure 3.12: Single crystal LiPB from sample I.33.

The average crystal size was about 3mm in length. A single crystal I33sc2 (having dimensions $4.70 \times 3.03 \times 1.19 mm^3$) was found to be superconducting and was oriented with respect to the 'a' and 'b' lattice parameters optically using single crystal XRD and the BOMEM interferometer. I33sc2 will be used for a-crystallographic axis reflectance measurements below $T_C \simeq 1.85$K using similar methodologies as references [51, 80].

Sample I.34:

pre-growth: Starting compounds had the same purities as that of I.26. Compounds were mixed and ground continuously for ∼10 minutes with a mortar and pestle. The powder was put into a 100^{o}C furnace overnight. Powder was removed from oven and ground continuously for ∼ 5 minutes. All tablets were pressed in the pressure range of 0.9-1.3 mT. Tablets were then put into a 100^{o}C furnace overnight. After seal-off, the total length of the ampoule and charge was ∼25cm and ∼12cm, respectively. The seal-off region of the ampoule was very narrow and some tablets broke as they passed through it.

post-growth: Sample appeared to have melted which can be confirmed by the visible contact angle, the absence of any visible tablets as well as an increase in the length of the charge (pre-growth charge length=12 cm, post-growth charge length=15 cm). Many LiPB single crystals were formed with some being as large as 6mm in length. The average crystal size was about 3mm in length. There was a large concentration of single purple crystals 8-12 cm from the hot zone (see Figure 3.13).

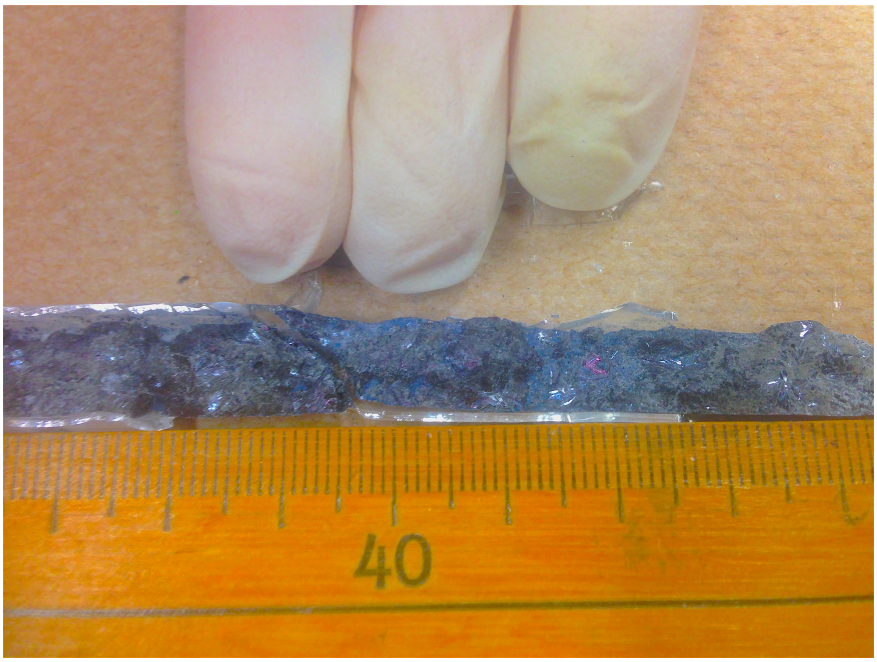

Figure 3.13: Crystal appearance of I.34 postgrowth and preleach. There appears to be a large concentration of single purple crystals 8-12 cm from the hot zone (Three fingers are pointing here.). Figure is enhanced to show purple crystals. Ticks on wooden ruler are in mm.

3.5 Table Summary of Growth Results for Lithium Purple Bronze

Table 3.5 summarizes the growth results for all samples prepared using the following chemical formula:

$$nLi_2MoO_4 + 2(1-n)MoO_3 + nMoO_2 \rightarrow 2Li_nMoO_3.$$

Table 3.5: Summary of different growth results. More crystals were tested from the 0.30, 0.31 and 0.33 batches for superconductivity than from the 0.28 and 0.34 batches (0.26 and 0.29 had no visible lithium purple bronze single crystals to test.) Cold zone is 15cm from hot zone.

Doping parameter n	Hot zone temperature (^{o}C)	Cold zone temperature (^{o}C)	Ampoule pressure before seal-off (torr)	Tablet pressure range (metric tons)	Growth Results
0.26	641	595	10^{-5}	0.9-1.3	Sample did not melt. Primary phase obtained was Mo_4O_{11}. No lithium purple bronze single crystals found.
0.28	645	610	10^{-5}	0.9-1.1	Sample did not melt. Trace amount of lithium purple bronze. Average crystal size is $\sim 2 \times 1 \times 0.5mm^3$. No superconducting crystals found.
0.29	645	610	10^{-7}	NA	Primary phase was Mo_4O_{11}. The crystals appeared a dark blue purple colour. No LiPB single crystals were found.
0.30	645	610	10^{-8}	0.3-0.5	Sample appears to have melted. Roughly 1/3 of the crystals obtained were lithium purple bronze with an average size of $\sim 2 \times 2 \times 0.5mm^3$. Few superconducting crystals found.
0.31	641	595	10^{-2}-760	0.7-0.9	Sample appears to have melted in the hot zone and melted slightly 14 cm from the hot zone. Average lithium purple bronze crystal size is $\sim 2 \times 2 \times 0.5mm^3$. So far only 1 superconducting crystal has been found.
0.33	641	595	10^{-6}	0.3-0.5	Melting at cold zone (i.e. roughly 14-15cm from the hot zone). Visible purple crystals were seen in the 14-15 cm region before sample was leached. Large lithium purple bronze crystals with average size $\sim 3 \times 3 \times 1.5mm^3$. Largest crystals were 7 mm in length. Some superconducting crystals were found. Specifically there is a crystal with dimensions $4.70 \times 3.03 \times 1.19mm^3$ which was confirmed superconducting with resistivity, ac and dc susceptibility. This sample will be used for a-axis optical work.
0.34	641	595	10^{-5}	0.9-1.3	Sample melted. Very similar description to $n = 0.33$. Only a few crystals have been tested for superconductivity. None of these crystals have shown a 2K superconducting transition.

3.6 Growth results of other samples of interest where Li is substituted by other alkali metals

This section discusses the preparation and growth results of three samples which were prepared using the following chemical formula:

$$nA_2MoO_4 + 2(1-n)MoO_3 + nMoO_2 \rightarrow 2A_nMoO_3,$$

where A=Na, K, Rb. These samples were grown using the temperature gradient flux technique with fixed doping parameter $n = 0.33$. The fourth sample $I.05_{Rb}$ (not included in the table below) was grown using solid state reaction outlined in [4]. The details of this method will be explained briefly in the $I.05_{Rb}$ pre-growth section. The details that will be discussed for the three growths tabulated in Table 3.6 include: starting compound purities, physical properties before and after crystal growth, charge length before crystal growth, ampoule total length[20], similarities and differences between samples, and any anomalous results or methodologies. The pregrowth conditions of each sample are outlined in Table 3.6.

[20]Ampoule total length refers to the length from one end of the inner wall of the ampoule to the other end of the inner wall of the ampoule.

Table 3.6: Growth parameters of each alkali metal sample. t_i is the time duration of the **preheat step**. T_0, T_5, T_{10} and T_{15} are the oven temperatures during the **diffusion/crystal growth steps** for the distances 0cm, 5cm, 10cm and 15cm from the hot zone, respectively.

Sample	n	T_i in cold/ hot zones (^oC)	t_i	T_0 (^oC)	T_5 (^oC)	T_{10} (^oC)	T_{15} (^oC)	Ampoule pressure before seal-off (torr)	Made tablets?	Tablet Pressure range (mT)
II.33_{Na}	0.33	595/641	4 days	641	637	621	595	10^{-5}	Yes (all)	0.9-1.3
III.33_{Rb}	0.33	595/641	4 days	641	637	621	595	10^{-5}	Yes (all)	0.9-1.3
IV.33_{K}	0.33	595/641	4 days	641	637	621	595	10^{-5}	Yes (all)	0.9-1.3

Sample $II.33_{Na}$:

pre-growth: Starting compounds had the following purities: ≥99% $Na_2MoO_4{\cdot}2H_2O$, 99.9995% MoO_3 and 99.98% MoO_2. All compounds were put in the oven at a constant 160^{o}C for several days before weighing out. The sodium molybdate was weighed out last to minimize any water absorption. After weigh out, the compounds were mixed and ground continuously for 10 minutes and then pressed into tablets in the pressure range of 0.9-1.3 mT. The crucible was then placed in the oven at 121^{o}C overnight to drive off any excess lubricant and water. After seal-off, the total length of the ampoule and charge was ∼21cm and ∼14cm, respectively.

post-growth: The sample melted and the melt was 15 cm in length. Many purple crystals were located 14-15cm from hot zone, which could be clearly seen prior to leaching (see Figure 3.14).

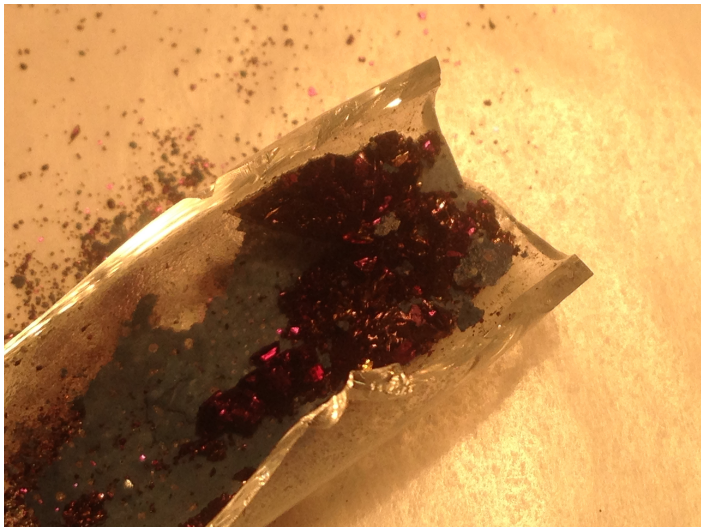

Figure 3.14: Appearance of large sodium purple bronze single crystals.

The average size of the single crystals was ≃5mm in length. XRD powder

analysis[21] confirmed the phase of these single purple crystals to be $Na_{0.9}Mo_6O_{17}$. Many of these single crystals had a polyhedral structure. There was an interesting macroscopic optical property worth noting for non-polyhedral single crystals of $Na_{0.9}Mo_6O_{17}$. When looking normal to the crystal edge (this edge is perpendicular to the plane) the sample wall appears golden in colour. As the sample is slowly rotated, the crystal edge changes from gold to purple in colour. This phenomenon was observed in non-polyhedral single crystals of $Na_{0.9}Mo_6O_{17}$.

[21] Analysis of powder data was done using PDXL [81].

Sample $III.33_{Rb}$:

pre-growth: Starting compounds had the following purities: 99.5% Rb_2MoO_4, 99.9995% MoO_3 and 99.98% MoO_2. All compounds were put in the oven at a constant 160^{o}C for several days before weighing out. Once the sample was weighed out it was ground continuously for 10 minutes with a mortar and pestle and then pressed into tablets in the pressure range 0.9-1.3 mT. Afterwards, tablets were put into a furnace overnight at 100^{o}C to drive off any excess lubricant and water. The tablets were put into the ampoule immediately after being removed from the oven. The ampoule was flamed twice before seal-off. After seal-off, the total length of the ampoule and charge was ∼24cm and ∼13cm, respectively.

post-growth: The charge length after crystal growth was ∼20cm, indicating that the tablets melted. There were shiny blue single crystals 17-20cm from the hot zone whose phase was confirmed[22] with powder XRD analysis to be $Rb_{0.3}MoO_3$ (blue bronze) which exhibits a CDW [28]. Looking through the melt, very small lilac brown single crystals were also found (see Figure 3.15). These crystals appear to have two allotropes similar to sulphur[23]: 1) Rhombic crystals (anatase) ($\sim 0.5 \times 0.3 \times 0.3\text{mm}^3$) and 2) rectangular prism crystals ($\sim 1 \times 0.1 \times 0.1\text{mm}^3$ and $1.5 \times 0.4 \times 0.4\text{mm}^3$).

[22] Analysis of powder data was done using PDXL [81].

[23] Sulphur forms both rhombic and rectangular prism shaped (monoclinic) crystals.

Figure 3.15: Lilac brown single crystals. Some of these crystals exhibit anomalous characteristics not inherent to tugarinovite. There are three forms of crystals present: *polyhedral* (POLY) having average dimensions $0.5 \times 0.3 \times 0.3\text{mm}^3$, *bar shaped and thin* (SBAR) having average dimensions $1 \times 0.1 \times 0.1\text{mm}^3$ and *bar shaped and thick* (LBAR) having average dimensions $1.5 \times 0.4 \times 0.4\text{mm}^3$. The latter are good conductors from 300K to 2K. See Chapter 5.1 for more details.

Powder XRD diffraction was performed on assorted lilac brown single crystals. XRD analysis confirmed[24] these crystals matched best with MoO_2 and tugarinovite (see Table 5.1) but have slightly larger 'a' and 'b' lattice parameters than those reported in reference [23, 38] as seen in Table 1.1. However, the 'c' lattice parameter seems to vary quite substantially (see Table 5.1). Furthermore, the XRD data (using PDXL analysis) also matched very closely with $Ti_{0.025}Mo_{0.975}O_2$.

[24] Analysis of powder data was done using PDXL [81].

Sample $IV.33_K$:

pre-growth: Starting compounds had the following purities: 99.8% K_2MoO_4, 99.9995% MoO_3 and 99.98% MoO_2. All compounds were put in the oven at a constant 160^{o}C for several days before weighing out. Once the sample was weighed out it was ground continuously for 10 minutes with a mortar and pestle and then pressed into tablets in the pressure range 0.9-1.3 mT. Afterwards, the tablets were put into a furnace overnight at 100^{o}C to drive off any excess lubricant and water. The tablets were put into the ampoule immediately after being removed from the oven. The ampoule was flamed twice before seal-off. After seal-off, the total length of the ampoule and charge was ∼24cm and ∼13cm, respectively.

post-growth: The charge length after crystal growth was ∼20cm (7cm longer than the pregrowth charge length), indicating that the tablets melted. There were shiny blue single crystals 16-20cm from the hot zone whose phase were confirmed with powder XRD to be $K_{0.3}MoO_3$ (blue bronze) which exhibits a CDW [28]. These blue crystals were fairly large (Figure 3.16 **a)**) and were on average 3-4mm in length. The largest $K_{0.3}MoO_3$ single crystals were approximately 1cm in length. Lilac brown single crystals were found throughout the melt (Figure 3.16 **b)**) which have an average length of ∼1.5mm.

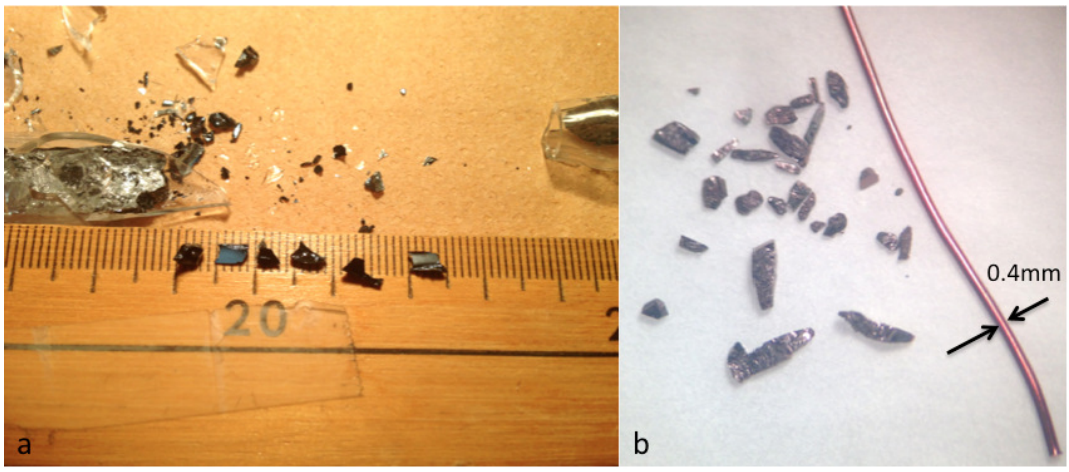

Figure 3.16: **a)** On the left are the potassium blue bronze $K_{0.3}MoO_3$ single crystals. Ticks on wooden ruler are in mm. **b)** On the right are the lilac brown single crystals of MoO_2 (seen next to a 26 AWG wire with 0.4mm diameter).

These lilac brown single crystals were larger on average than the ones obtained from the $III.33_{Rb}$ crystal growth. Powder XRD analysis[25] was performed on the lilac brown crystals. The XRD data matched best with MoO_2.

[25] Analysis of powder data was done using PDXL [81].

This next crystal growth was performed after analysing the characteristics of the lilac brown single crystals obtained from the III.33_{Rb} growth (see Chapter 5.1.2 and 5.1.3). These anomalous properties matched closely with those found in the literature for polycrystalline $K_{0.05}MoO_2$ [4–7]. The pre-growth parameters are briefly outlined below along with the post-growth results.

Sample $I.05_{Rb}$:

pre-growth: The polycrystalline sample was prepared using the following chemical formula:

$$41Mo + 76MoO_3 + 3Rb_2MoO_4 \rightarrow 120Rb_{0.05}MoO_2. \tag{3.14}$$

The starting compounds had the following purities: 99.5% Rb_2MoO_4, 99.9995% MoO_3 and 99.95% Mo powder. The starting compounds Rb_2MoO_4 and MoO_3 were dried several days at 160^{o}C before use. Mo power was not dried. Once all compounds were weighed out they were ground continuously for 10 minutes. A total of 6 tablets were prepared (i.e. 3 grams total). Petroleum ether was used as a lubricant. Tablets were pressed twice at roughly ∼1.5mT. Before crystal growth the tablets appeared turquoise in colour (Figure 3.17 **a)**). The ampoule was flamed twice before seal-off. Pressure in the ampoule after seal-off was 10^{-6} torr. The ampoule was placed at the bottom of the oven with the tablets centred. It was preheated for ∼1 day at ∼410^{o}C, then heated to ∼720^{o}C for ∼3 days and then cooled down to room temperature.

post-growth: The tablets appeared black in colour (Figure 3.17 **b)**). There appeared to be an opaque deposit along the inner ampoule wall at the location of the 6 tablets during crystal growth (Figure 3.17 **c)**).

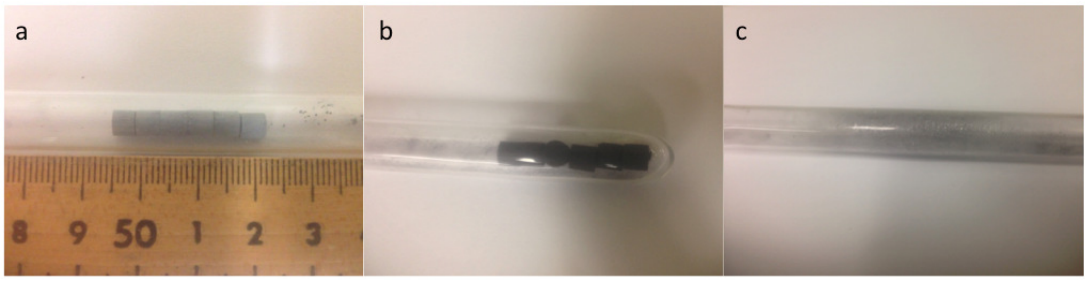

Figure 3.17: **a)** The left figure shows the 6 tablets inside the sealed ampoule before crystal growth. Notice the turquoise colour of the tablets. **b)** The middle figure shows the 6 tablets inside the sealed ampoule after crystal growth. Notice the tablets appear black (identical in appearance to 99.98% MoO_2). **c)** The right figure shows an opaque deposit along the inner ampoule wall which appeared after crystal growth.

Inductively coupled plasma mass spectrometry ICP-MS was performed on tablet 1/6 to verify the true doping of the sample to be $Rb_{0.03}MoO_{2-\delta}$ where the parameter δ has yet to be determined[26]. Tablet 1/6 was then cut into a bar and a cylindrical disc. Resistivity measurements were performed on the bar-shaped sample. DC susceptibility measurements were performed on the cylindrical disc sample. The evidence collected by both sets of measurements show that the sample is superconducting (see Chapter 5.2). ZFC (zero field cooling)/FC (field cooling) measurements were performed and resistivity measurements were

[26]ICP-MS cannot give percent composition of oxygen.

performed (at various fields) which confirms a superconducting transition temperature of $\sim$3.5K.

Chapter 4

Results and Discussion: Lithium Purple Bronze

In section 4.1 we discuss non superconducting LiPB and its $\sim$ 25K energy gap along the b-crystallographic axis. In section 4.2 we discuss the superconducting trends of LiPB and discuss the alignment of a particular superconducting crystal using single crystal XRD and optical anisotropy. In this section I provide a simple analysis of the results of my measurements[1].

[1]For simplicity I perform analyses that do not take into account the special states of the material.

4.1 Non-Superconducting Lithium Purple Bronze

This section has two main foci. Firstly, we probe the metal insulator (M/I) transition of $Li_{0.9}Mo_6O_{17}$ and see how the low temperature resistance data changes as excitation current is varied. Secondly, by measuring resistivity as a function of temperature we probe the M/I transition for a sample aligned along the b-crystallographic axis[2] and evaluate how the energy gap changes as a function of temperature. Both samples were connected in a four probe resistivity geometry. 0.05 mm diameter (99.995% pure) gold wire was used for the V+/V- and I+/I- connections which were connected in-plane. The I+/I- current probes were connected perpendicular to the long axis of each sample along the sample edge and they spanned the whole width of the sample. The V+/V- connections were also connected perpendicular to the sample spanning the whole width of the sample (refer to Figure 4.1).

[2]LiPB crystals seem to grow with their low resistive axis (i.e. b-crystallographic axis) along the long axis of the crystal [12], which was confirmed in section 4.2.2.

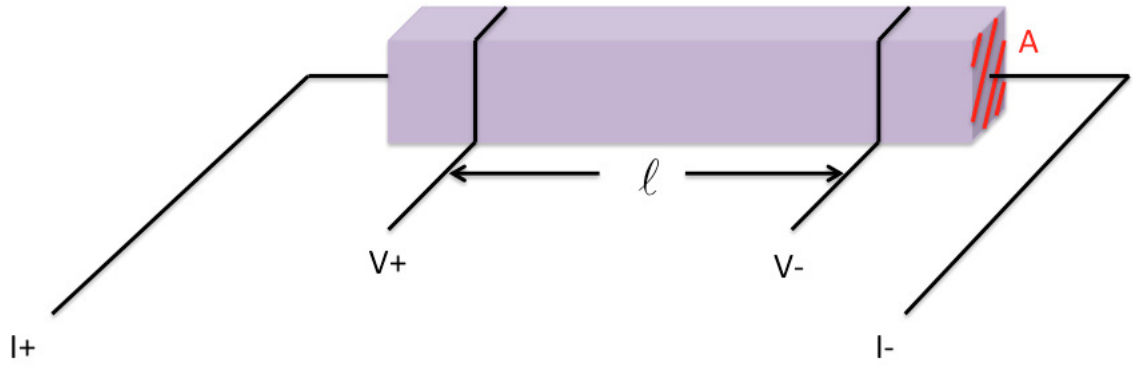

Figure 4.1: This diagram relates ρ to the resistance R of a bar-shaped sample, the following relation is $\rho = \frac{A}{l}R$.

4.1.1 Varying excitation current

In this section, we consider various excitation currents applied to LiPB. The apparatus used was a Quantum Design Physical Property Measurement System PPMS which measured resistance as a function of temperature on a bar shaped sample with four probe resistivity set up along the long axis of the sample similar to Figure 4.1. In Figure 4.2 various excitation currents 0.1, 1, 1.5, 2 and 2.5mA are applied to the sample.

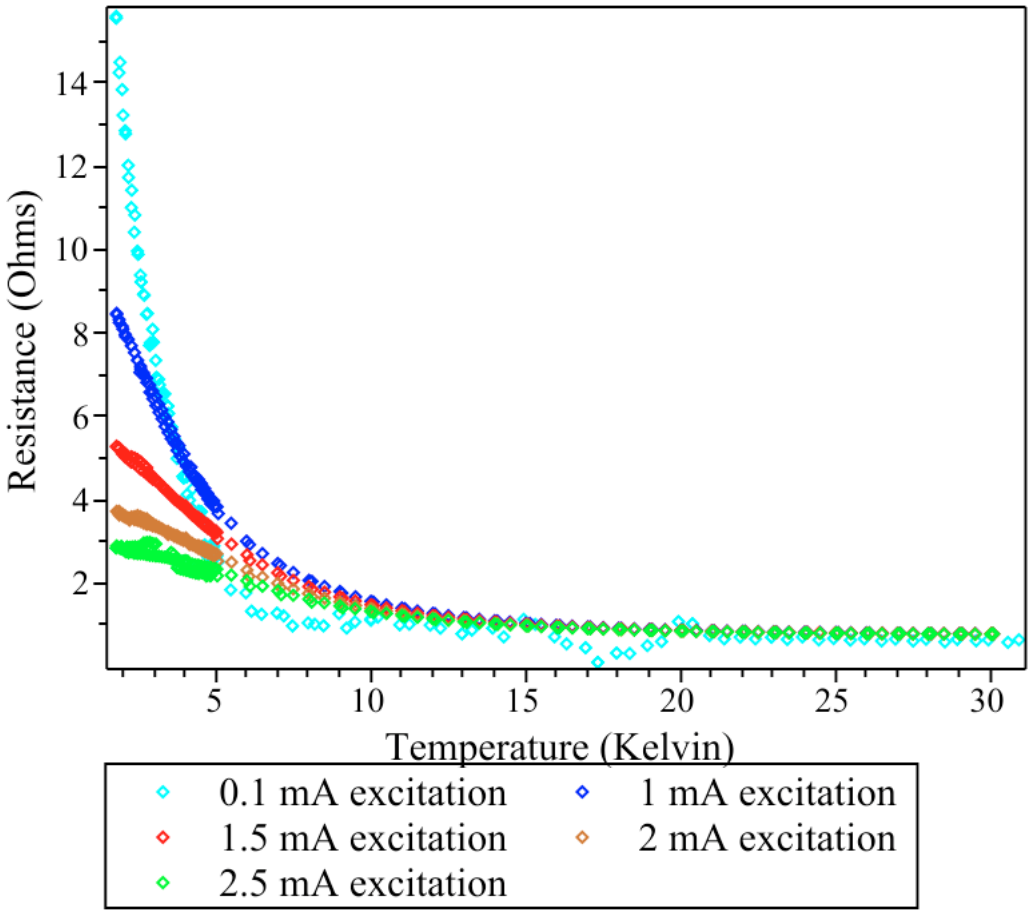

Figure 4.2: In-plane resistance as a function of temperature for a LiPB single crystal for various excitation currents (sample was taken from I.33 batch).

For $T \leq$10K, the insulating properties of LiPB are suppressed by a greater

amount with increasing excitation current. Furthermore, in this plot we see that the sample resistance is unstable[3] at 0.1mA excitation current (this was not the case for every sample). In Figure 4.3 various excitation currents 3, 3.5, 4, 4.5 and 5mA are applied to the same sample.

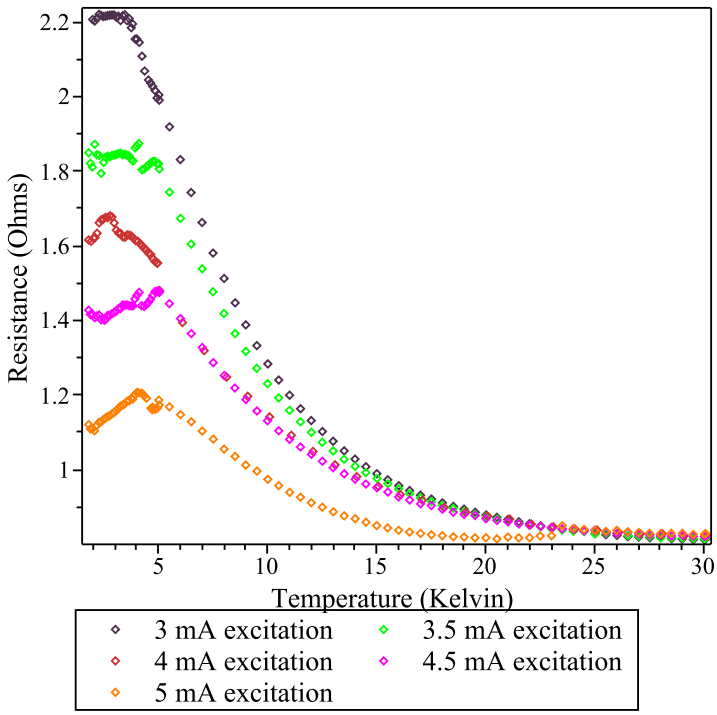

Figure 4.3: In-plane temperature dependence of the resistance for various excitation currents for single crystal LiPB (same sample from Figure 4.2). For this particular sample, with excitation currents $I \geq 4$mA, joule heating begins to affect the sample resistivity at temperatures less than ~ 5K.

For $T \lesssim 23$K, the insulating properties of LiPB are suppressed by a greater amount with increasing excitation current. The insulating transition is fully suppressed from 5K to 2K for 3mA and 3.5mA. Joule heating begins to affect

[3]This can be seen by the fluctuations in resistance at 20K, 17K and 15K.

sample resistivity at 4, 4.5 and 5mA excitation currents from 5K to 2K. We deduce that for excitation currents greater than a certain value I_S the sample begins to experience complete suppression of its insulating properties, and resistivity data is no longer valid at low temperatures. This effect is important when considering which excitation currents can be used to obtain accurate energy gap E_g results. Furthermore, when checking for superconducting samples one must be sure to use an excitation current $I < I_S$. From Figure 4.3 we deduce that $I_S \sim 3$mA for this particular sample. Hence for all low temperature LiPB resistivity data presented in this work, we used excitation currents in the range $0.1\text{mA} < I \leq I_S/2$ for similar sized samples as the one measured in Figures 4.2 and 4.3.

Section 4.1.2 will provide a derivation for evaluating the temperature dependence of the band gap energy $E_g(T)$ from the resistivity. This derivation is assuming a 3D density of states. Only the important equations will be shown. For a more complete derivation see reference [82]. In section 4.1.3, resistivity as a function of temperature data of a LiPB non superconducting sample aligned along the b-crystallographic axis will be presented in Figure 4.5. The resistivity data was fit to equation (4.14) using a computer program written in MAPLE 14 (this program can be found in Appendix D). Equation (4.14) is then used to determine the energy gap $E_g(T)$ and the result is presented in Figure 4.6.

4.1.2 Band gap energy derivation

To derive an equation for the band gap energy, one needs to first consider the concentration of intrinsic charge carriers as a function of temperature. The temperature range of interest is from 1.8K to 35K (LiPB M/I transition). Typically the Fermi level μ is constrained to lie within the band gap [82] and thus one can make the approximation that

$$\epsilon - \mu \gg k_B T, \tag{4.1}$$

where ϵ is the energy of a single particle state in the conduction band, k_B is the Boltzmann constant and T is the temperature of the system. Since the charge carriers in this case are electrons, the Fermi-Dirac distribution function can be approximated by use of equation (4.1):

$$f(\epsilon) = \frac{1}{e^{(\epsilon-\mu)/k_BT}+1} \simeq e^{\frac{(\mu-\epsilon)}{k_BT}}, \tag{4.2}$$

which gives the probability that an orbital in the conduction band is occupied. Figure 4.4 provides a plot of the Fermi-Dirac distribution function.

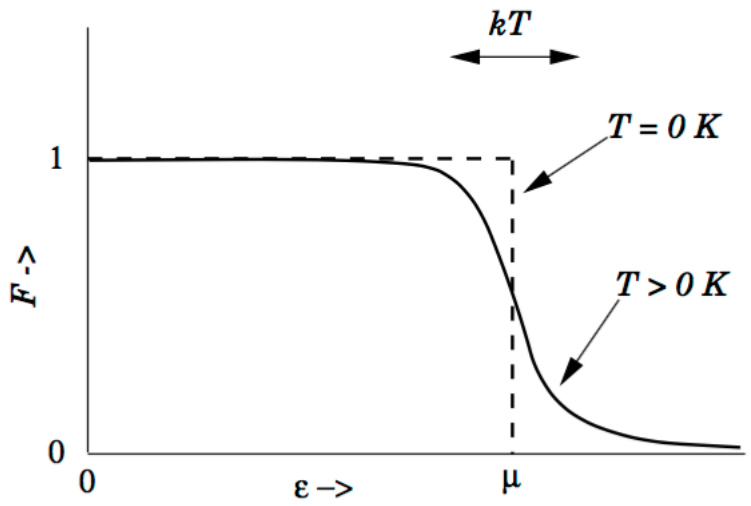

Figure 4.4: Fermi-Dirac distribution function is the probability that an eigenstate at energy ϵ is occupied. For small temperatures this function approximates a step function with the step occurring over a small range $\sim k_BT$ about μ. This figure was taken from reference [83].

The energy of an electron in the conduction band measured from the conduction band edge is given by

$$\epsilon_{cond} = \epsilon - E_c, \tag{4.3}$$

where E_c is the energy of the conduction band edge. Thus the density of states (in 3D) measured from the conduction band edge becomes

$$g(\epsilon) = \frac{1}{2\pi^2}\left(\frac{2m_e}{\hbar^2}\right)^{3/2}(\epsilon - E_c)^{1/2}, \tag{4.4}$$

where m_e is the effective mass of a conduction electron. Thus, the concentration of electrons in the conduction band can be found by the following:

$$n = \int_{E_c}^{\infty} g(\epsilon)f(\epsilon)d\epsilon = 2\left(\frac{m_e k_B T}{2\pi\hbar^2}\right)^{3/2} e^{\frac{(\mu - E_c)}{k_B T}}. \tag{4.5}$$

By a similar argument one can find the concentration of holes in the valence band p

$$p = 2\left(\frac{m_h k_B T}{2\pi\hbar^2}\right)^{3/2} e^{\frac{(E_v - \mu)}{k_B T}}, \tag{4.6}$$

where m_h is the effective mass of a conduction electron. For an intrinsic semiconductor the electron density in the conduction band n is equal to the hole density in the valence band p. This occurs because the thermal excitation of an electron into the conduction band leaves behind a hole in the valence band. Hence, for an intrinsic semiconductor there is a $1:1$ ratio of electrons and holes (i.e. $n = p$), which implies

$$np = n^2 = 4\left(\frac{k_B T}{2\pi\hbar^2}\right)^3 (m_e m_h)^{3/2} e^{\frac{(E_v - E_c)}{k_B T}} = 4\left(\frac{k_B T}{2\pi\hbar^2}\right)^3 (m_e m_h)^{3/2} e^{\frac{(-E_g)}{k_B T}}, \tag{4.7}$$

$$\therefore n = 2\left(\frac{k_B T}{2\pi\hbar^2}\right)^{3/2}(m_e m_h)^{3/4} e^{-\frac{E_g}{2k_B T}}, \tag{4.8}$$

where E_v is the energy of the valence band edge and $E_g = E_c - E_v$ is the energy gap between the valence band edge and the conduction band edge. The electrical conductivity can be shown by simple arguments [82] to be

$$\sigma = \frac{ne^2\tau}{m_e}, \tag{4.9}$$

where τ is the mean time an electron travels between two consecutive collisions. Finally the resistivity ρ is the inverse of the electrical conductivity by definition

$$\rho = \frac{1}{\sigma} = \frac{m_e}{ne^2\tau} = \frac{1}{2}\left(\frac{k_B T}{2\pi\hbar^2}\right)^{-3/2}\frac{m_e^{1/4}}{e^2\tau m_h^{3/4}} e^{\frac{E_g}{2k_B T}}. \tag{4.10}$$

In general E_g is a function of temperature, hence equation (4.10) can be written as[4]

$$\rho = \rho_o \cdot T^{-3/2} \cdot e^{\frac{E_g(T)}{2k_B T}}, \tag{4.11}$$

where ρ_o is a constant. At the opening of the energy gap, the exponential term dominates[5] the temperature dependence [82], hence equation (4.11) becomes[6]

[4]Equation (4.11) can be re-expressed in 1D (d=1) and 2D (d=2) and a constant E_g can be assumed. In this case, for dimensionalities between d=1 and d=2, the resistivity data fit best in the temperature range 2-5K and 20-25K, however the data 6-24K did not fit well. This could be due to the lack of knowledge of dimensionality as well as the nature of the density of states. In general τ is a function of temperature which could also affect this fit method.

[5]This is only true for values in the argument of the exponential $\gtrsim 100$.

[6]This is the same equation used to find $E_g(T)$ along the b-crystallographic axis in reference [1].

$$\therefore \rho \simeq \rho_o e^{\frac{E_g(T)}{2k_BT}}. \tag{4.12}$$

Therefore, equation (4.12) in terms of the resistance R of the sample becomes[7]

$$\therefore R = \frac{l}{A}\rho = \left(\frac{l}{A}\rho_o\right) e^{\frac{E_g(T)}{2k_BT}} = R_o e^{\frac{E_g(T)}{2k_BT}}, \tag{4.13}$$

which is only true for bar-shaped samples (see Figure 4.1). Equation (4.13) can be rewritten as

$$\boxed{\ln R = \ln R_o + \frac{E_g(T)}{2k_BT}}. \tag{4.14}$$

Equation (4.14) is used for finding $E_g(T)$ in Figure 4.6.

[7]For arbitrarily shaped samples the resistivity is still directly proportional to the resistance of the sample. In particular $\rho = 2\pi F(1/s_1 - 1/(s_2+s_3) - 1/(s_1+s_2) + 1/s_3)^{-1}R$, where s_1 is the probe spacing between I_+ and V_+, s_2 is the probe spacing between V_+ and V_-, s_3 is the probe spacing between V_- and I_-, F is a correction factor containing sample thickness, lateral sample dimensions and probe placement relative to sample edges [86].

4.1.3 Band gap energy results

The resistivity data presented in Figure 4.5 agrees with the accepted value of resistivity for a ρ_b aligned sample (i.e. a sample aligned along the low resistive b-crystallographic axis) [14, 15].

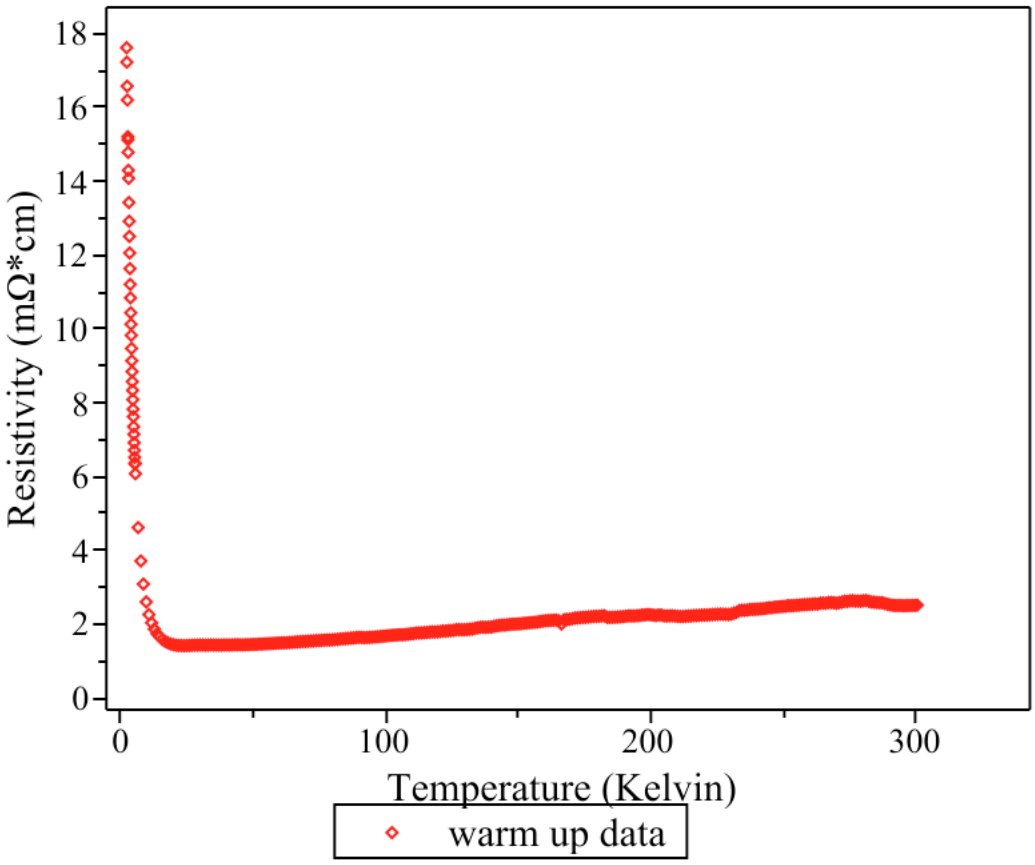

Figure 4.5: This plot shows the temperature dependence of the resistivity oriented along the b-crystallographic axis (i.e. along its long axis). The single crystal was bar shaped from batch I.30 and a 1mA excitation current was applied.

The vertical error bars are ∼0.1mΩ·cm (smaller than the thickness of individual points). The resistivity as a function of temperature (Figure 4.5) was fit to $y = mx + B$ (i.e. equation (4.14)) using a least squares fit between five

consecutive points at a time with the substitutions: $y = \ln(R)$, $B = \ln(R_o)$, $x = 1/T$ and $m = E_g/2k_B$. The energy gap E_g was solved for using $E_g = 2k_B m$ and then $E_g(T)$ was plotted in Figure 4.6.

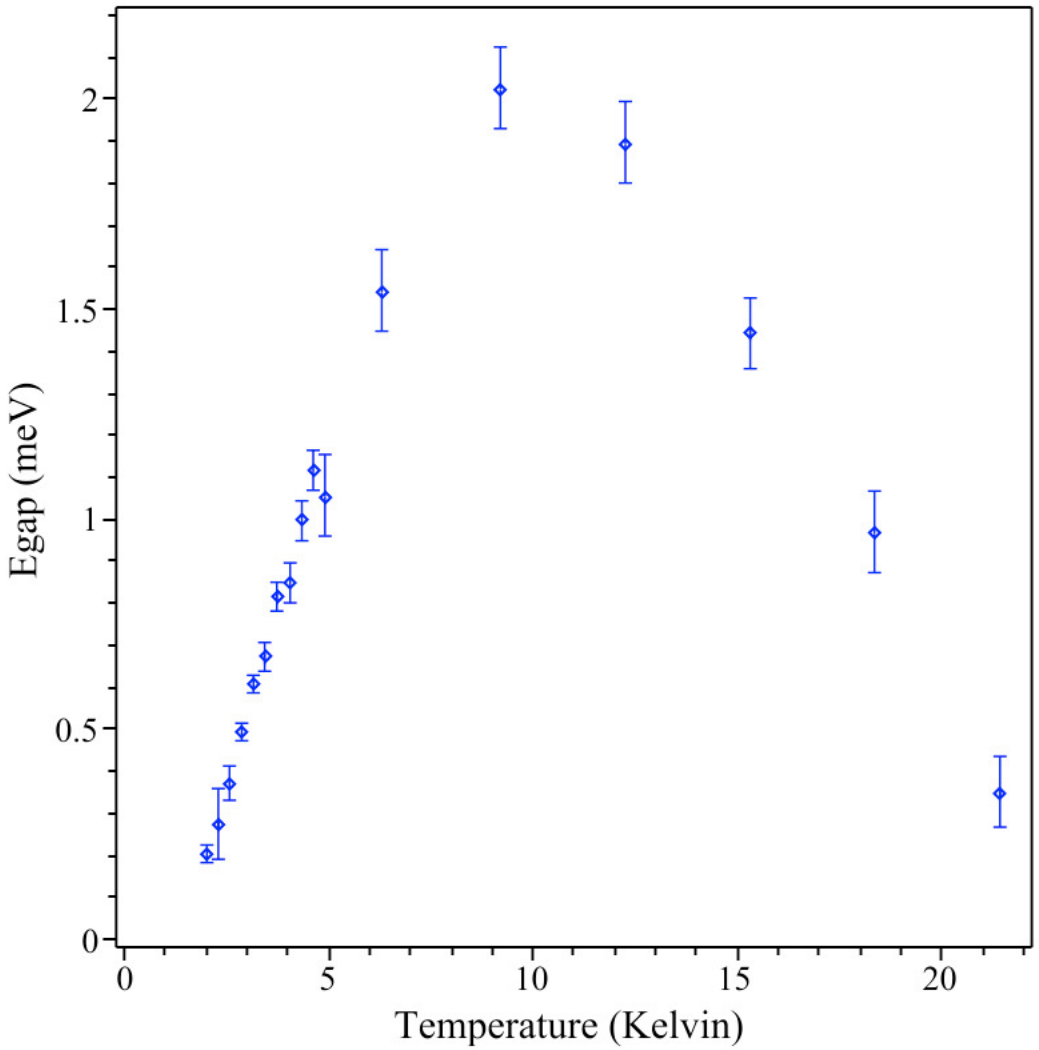

Figure 4.6: This plot shows the temperature dependence of the energy gap extracted from the data in Figure 4.5. The energy gap has a peak of 2.0meV±0.1meV at 9.16K.

It was found that the energy gap has a peak of 2.0meV±0.1meV at 9.16K. This maximum value is twice the value stated in the literature where the gap

maximum is ∼1meV at 5-6K [1, 2]. In addition, $E_g(T)$ seems to approach much lower values as $T \to 0$K which deviates from reference [1]. It seems that a more rigorous approach needs to be used to find $E_g(T)$. Using the data from Figure 4.6 notice that $E_g(T)/2k_BT \gtrsim 100$ does not hold and hence one cannot go from equation (4.11) to equation (4.12). A more rigorous approach should be used to find $E_g(T)$ which takes into account the low dimensionality of the system. One could also try expressing $\tau := \tau(T)$.

4.2 Superconducting Lithium Purple Bronze

Superconductivity of lithium purple bronze single crystals can be confirmed using various techniques. In this section we review three specific techniques, DC susceptibility, AC susceptibility and resistivity. We will discuss how these techniques were used to confirm the presence of superconductivity and will focus our attention on measurements done on the sample I33sc2. For resistivity measurements, all samples were measured using four probe resistivity[8] as shown in Figure 4.1 using a Quantum Design PPMS. The lowest excitation current was applied to each sample such that the resistance remained stable. An example of a resistance measurement for the sample I33sc2 is shown in Figure 4.7, the sample shows a superconducting transition around 2K along with a M/I transition at 25K.

[8]The I+/I- current probes were connected perpendicular to the long axis of the sample along the sample edge and they spanned the whole width of the sample. The V+/V- connections were also connected perpendicular to the sample spanning the whole width of the sample.

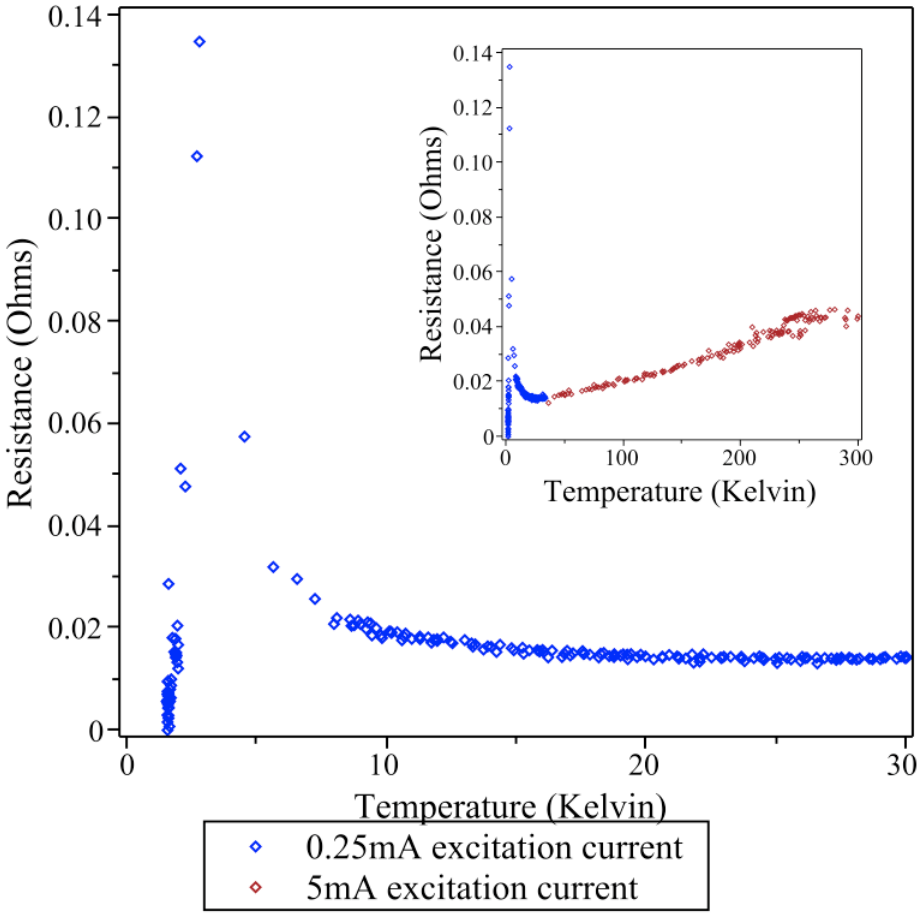

Figure 4.7: In-plane resistance as a function of temperature of superconducting lithium purple bronze. The sample used here was I33sc2. 5mA excitation current was used from 300K to 30K and then 0.25mA excitation current was used from 30K to 1.5K (see upper inset). Notice the superconducting transition at T_C ~2K.

A small excitation current is important when checking for superconductivity because LiPB has a transition temperature of 2K which is the temperature regime where joule heating begins to affect sample resistance (see Figure 4.3).

DC susceptibility was measured using a Magnetic Property Measurement System MPMS. Figure 4.8 explains the setup used to measure DC susceptibility.

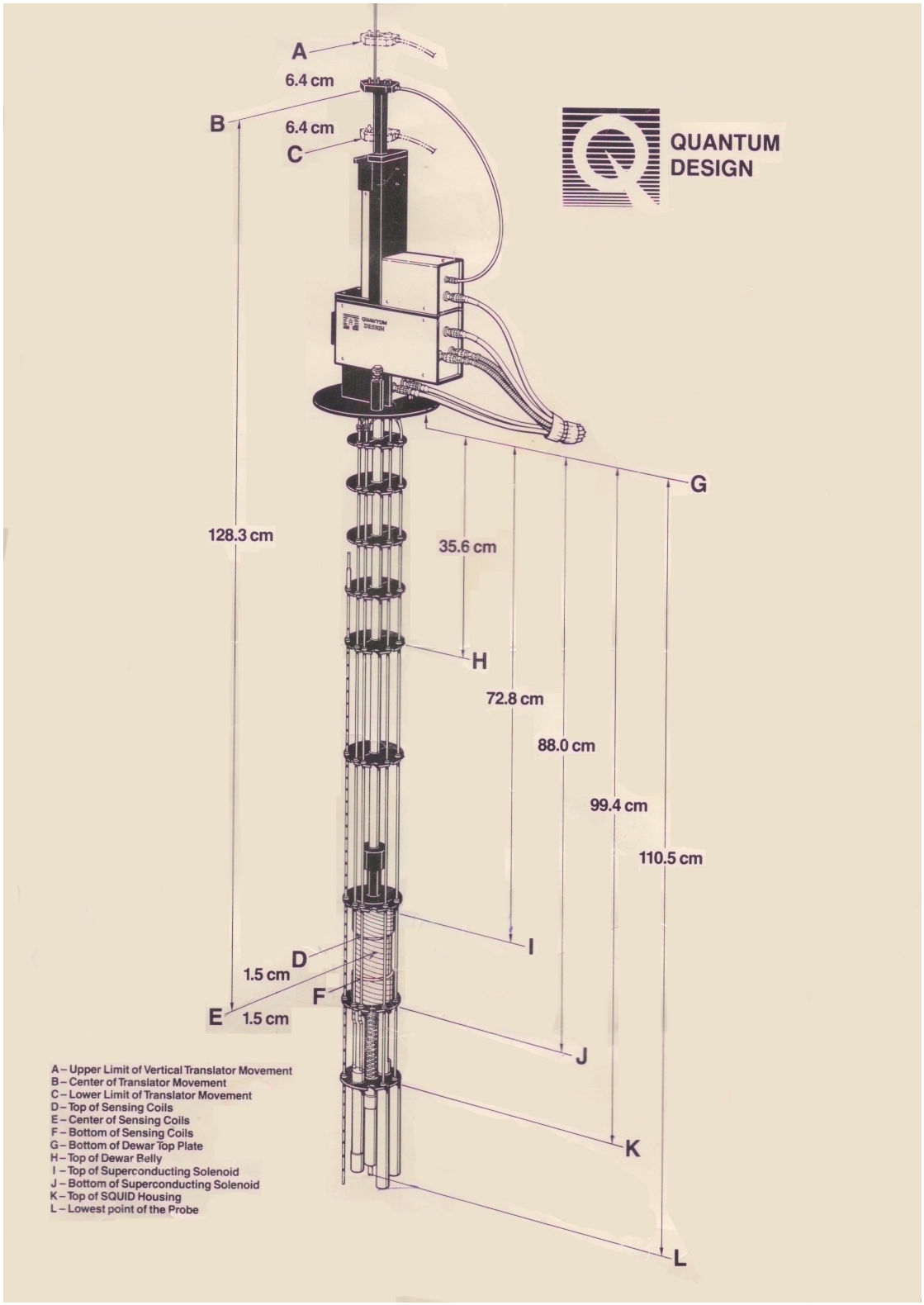

Figure 4.8: This diagram is the MPMS sample reservoir. This instrument was used for all DC susceptibility measurements. Notice here that the sample location (E) must be $\sim$ 128cm from B.

The positions B and E in Figure 4.8 are connected using a metal rod as seen in Figure 4.9 a. Position B is represented by the edge of the plastic black bracket as seen in Figure 4.9 b. Position E is the location of the sample as seen in Figure 4.9 c.

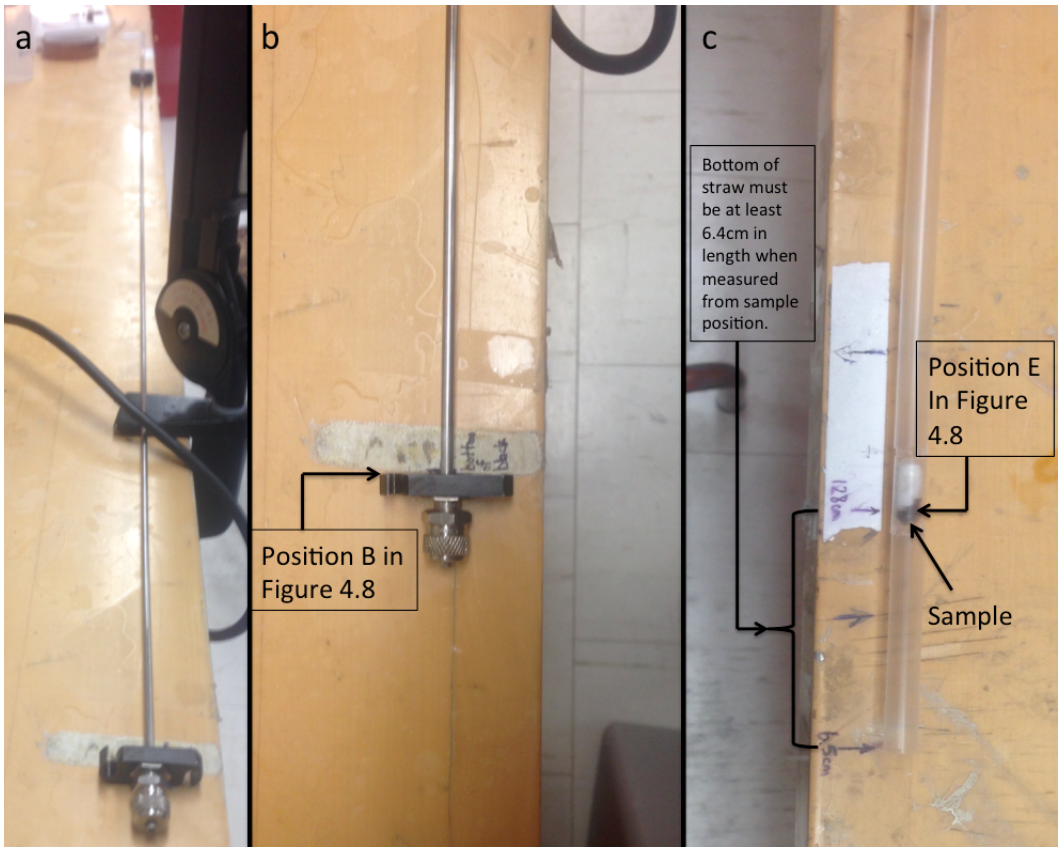

Figure 4.9: **a**: Diagram of the MPMS metal rod sample probe. **b**: The edge of the plastic black bracket (position B in Figure 4.8). **c**: Sample location (position E in Figure 4.8) is $\sim$ 128cm from position B.

The important feature here is that the sample placement (represented by position E) is located in the centre of the sensing coils (i.e. 128.3cm$\sim$ 128cm distance between positions B and E) and that the bottom of the straw (i.e. the sample holder) does not move between the top and centre region of the sensing coils

(position D to position E) during a measurement. In one complete measurement the machine scans from C to A representing a scan range of 12.8cm (6.4cm above and below the sample). In particular, notice the 6.4cm scan length from B to A. It is important that the straw length extends at least 6.4cm below the sample to avoid any magnetic response of the straw edge.

Figure 4.10 shows the magnetization as a function of the applied field for a lead shot[9] at constant 5K.

[9]Lead has a superconducting transition temperature of 7.175K [87].

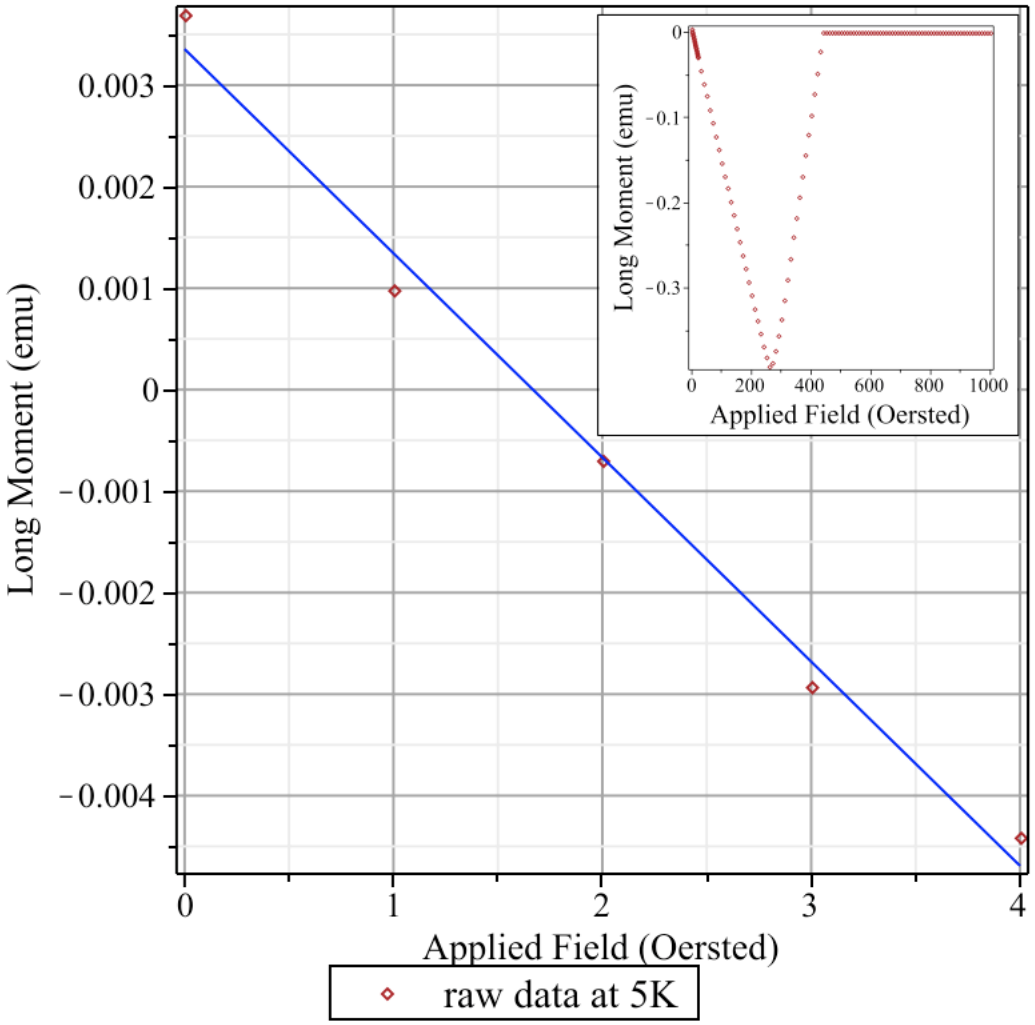

Figure 4.10: Calibration of MPMS zero field using lead shot. The lead shot has a mass of $\sim$ 140mg with purity 99.999% and is approximately spherical in shape.

This measurement was performed to determine the zero field of the MPMS. The applied field began at 0 Oe and was swept to 1000 Oe in intervals of 1 Oe (see upper inset). For $T < T_C$ and $H < H_C$ we would expect a linear response of the magnetization[10] (see Figure 2.2). The applied field value which intersects the line of zero magnetization is the zero field of the system. It was deduced that zero

[10]Lead is a Type 1 superconductor.

field for our system is approximately 1.5 Oersted. When doing a zero field cool (ZFC) it is imperative to get as close to zero external field as possible. Notice how the magnetization doesn't immediately equal zero as we increase the applied field slightly above $H_C = 260$ Oe (not including demagnetization) as expected in a Type 1 superconductor (see Figure 2.2). This is because the lead shot is approximately spherical and has a non zero demagnetization factor, hence there exists an intermediate state which is responsible for a linear decrease to zero magnetization for applied fields above 260 Oe [88] . Taking into account demagnetization[11] for a sphere, the critical field $H_C \simeq (3/2)(260\text{ Oe}) = 390$ Oe. This value differs slightly with the accepted value of $H_C \simeq 432$ Oe for lead [89].

Recall for a Type 2 superconductor, when $T < T_C$ and applied field $H < H_{C1}$ the magnetization has a linear decreasing slope for increasing H which creates a minima at $H = H_{C1}$. The magnetization then decays to zero as $H \to H_{C2}$ (see Figure 2.2). Figure 4.11 shows magnetization as a function of applied field at constant 1.71K for I33sc2.

[11] The demagnetization of a spherical body yield a factor of 3/2, however the lead shot used in the measurement shown in Figure 4.10 was approximately spherical.

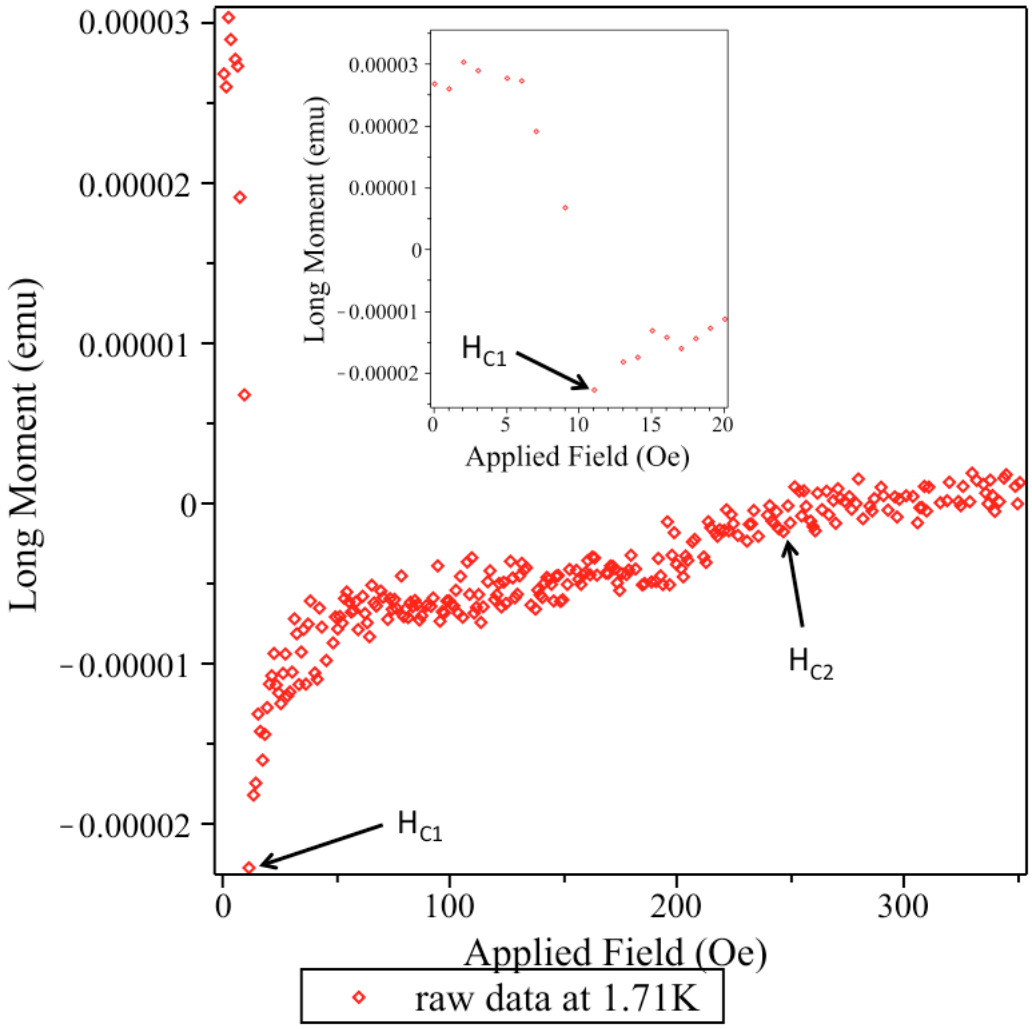

Figure 4.11: Magnetization as a function of applied magnetic field for the sample I33sc2. Plane of the sample was oriented perpendicular to the applied field. Temperature was maintained at a constant 1.71K throughout this measurement. Comparing this plot to Figure 2.2, we can see that this sample exhibits similar characteristics to that of a Type 2 superconductor. In particular H_{C1} ∼11 Oe and H_{C2} ∼250 Oe for this sample (not including demagnetization).

Notice in the upper inset when $H < 11$ Oe the magnetization has a linear decreasing slope for increasing H and has a minima at H =11 Oe. Furthermore,

the magnetization decays to zero as $H \rightarrow 250$ Oe. Hence, I33sc2 is a type 2 superconductor with H_{C1} ~11 Oe and H_{C2} ~250 Oe (not including demagnetization). Figure 4.12 shows magnetization as a function of temperature (DC) of I33sc2 and a diamagnetic transition can be seen at ~1.85K.

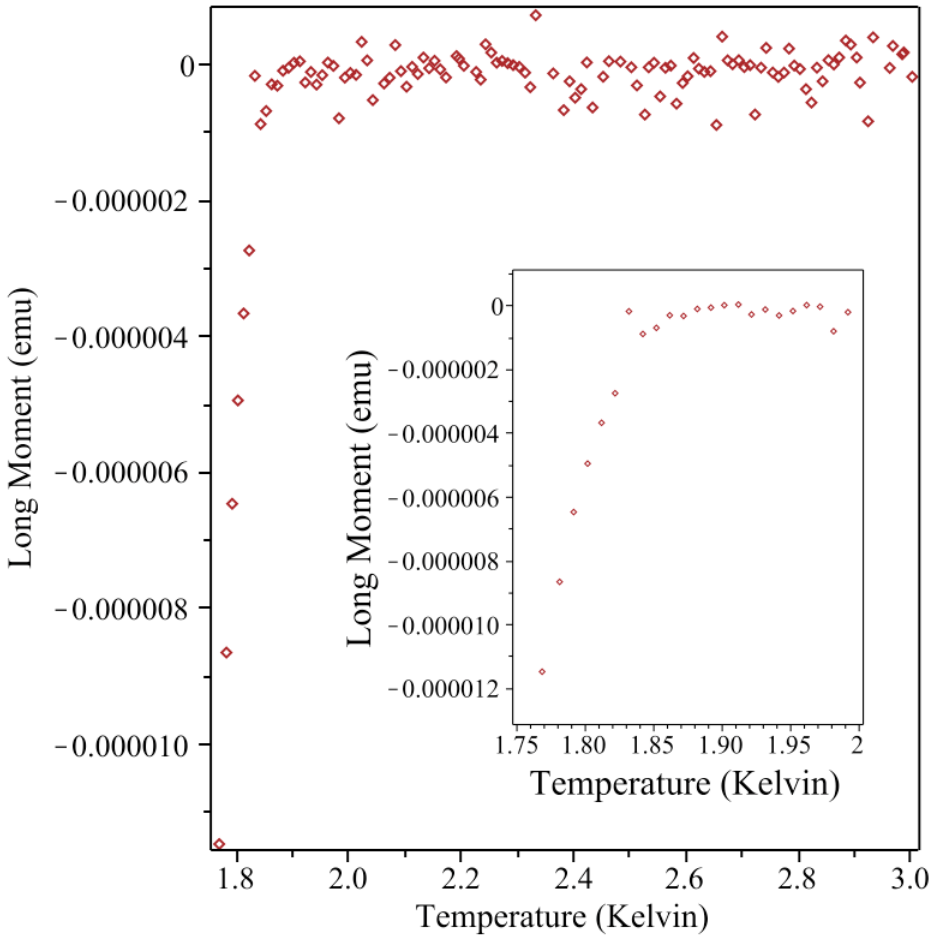

Figure 4.12: ZFC DC susceptibility of superconducting lithium purple bronze (sample I33sc2) at 8 Oe where the plane of the sample is perpendicular to the applied field. Notice the superconducting transition at T_C ~1.85K (see lower inset).

AC susceptibility was measured using a Quantum Design PPMS and the AC

coil was built by hand (refer to Appendix A for details). Figure 4.13 shows magnetization as a function of temperature (AC) of I33sc2 and a diamagnetic transition can be seen at ∼1.85K.

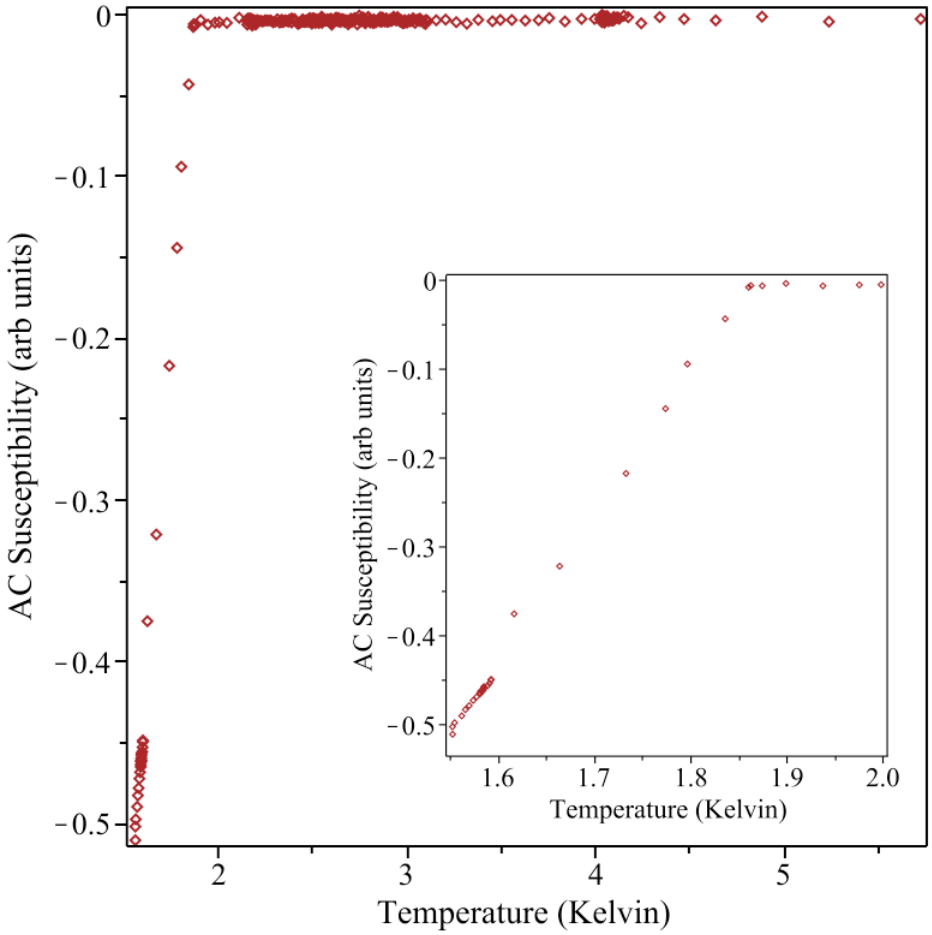

Figure 4.13: FC AC susceptibility of superconducting lithium purple bronze (sample I33sc2) where the plane of the sample is perpendicular to the applied field. Notice the superconducting transition at T_C ∼1.85K (see lower inset).

Therefore, from the measurements of resistance as a function of temperature (Figure 4.7), magnetization as a function of applied field (Figure 4.11), DC and AC susceptibility (Figures 4.12 and 4.13) we have confirmed the LiPB single

crystal 'I33sc2' has a superconducting transition temperature of $T_C \sim 2$ K. In the next two sections we will discuss the sample orientation with respect to the 'a' and 'b' crystallographic lattice parameters.

4.2.1 Single Crystal X-Ray Diffraction

The LiPB single crystal I33sc2 was analysed by single crystal XRD. The purpose of this measurement was to confirm that the a-crystallographic lattice parameter is perpendicular to the plane of the single crystal. The sample plane was oriented parallel to the glass slide (Figure 4.14).

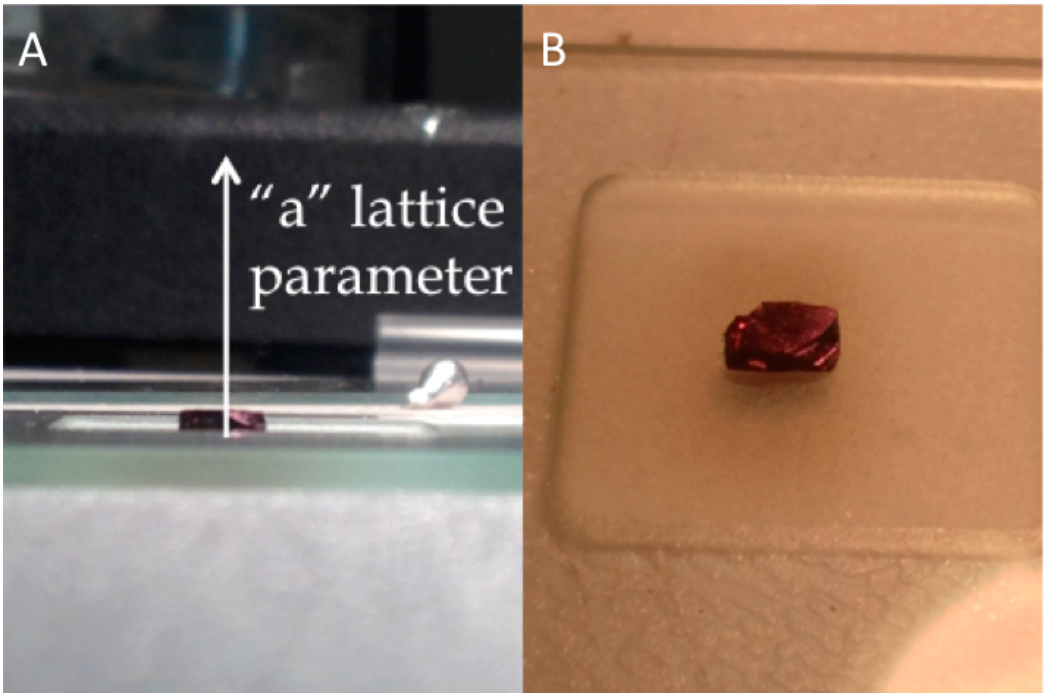

Figure 4.14: Position of I33sc2 on the glass slide. **A**: Out-of-plane direction is facing upwards which is along the 'a' lattice parameter; a similar observation is noted in [12]. **B**: Position of I33sc2 on glass slide from top view, one can clearly see that the flat plane of the sample is parallel to the surface of the glass slide.

A small angle range was scanned about the point $2\theta = 6.918^o$ (corresponding to the a-crystallographic lattice parameter[12]). The a-crystallographic lattice parameter corresponds to 12.762$\mathring{A}$. A source beam wavelength of λ=1.54$\mathring{A}$ was

[12]see the first row of Table C.3

used. Solving $2a \sin\theta = \lambda$, we obtain $2\theta = 6.918^o$ which is the approximate location of the peak. Examining Figure 4.15 one observes a large peak about $2\theta = 6.918^o$. This result confirms that the a-crystallographic lattice parameter is perpendicular to the plane of the single crystal.

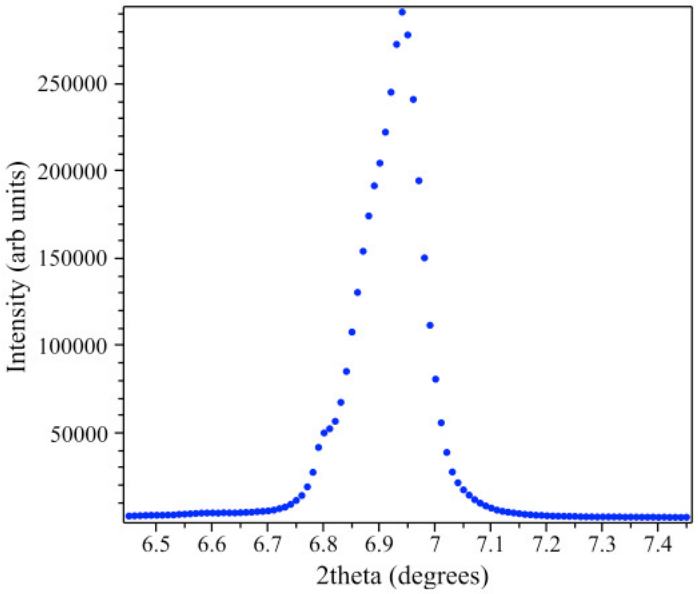

Figure 4.15: Result of single crystal XRD of I33sc2 for the geometry given in Figure 4.14.

4.2.2 Crystal Alignment via Optical Anisotropy

A BOMEM Mid-Infrared Michelson interferometer with a Mercury Cadmium Telluride MCT liquid nitrogen cooled detector was used. This is a quantum detector that detects infrared light through its interaction with a semiconducting material [90]. The interaction of the incident light onto the semiconducting material liberates electrons from the valence band into the conduction band. The energy of the incident photons is directly proportional to their frequency and a photon will liberate an electron as long as its wavelength is smaller than the cut-off wavelength of the detecting material. Since noise can be generated through thermal excitations of the electrons, the quantum detector was cooled down to liquid nitrogen temperatures prior to each measurement [90].

Lithium purple bronze has a monoclinic structure and has very different resistances along all three crystal axes. The high and low in-plane resistive axes of the sample I33sc2 were determined by the method outlined below.

Nominally unpolarized light is incident on a polarizer. The polarizer causes the incident light to become linearly polarized. The polarization vector of the outgoing light points parallel to the 0^o and 180^o transmission axis (white line shown in Figure 4.16 (right)). The main feature in Figure 4.16 is how the long axis of the sample is nearly perpendicular to the transmission axis of the polarizer at polarization angle of 0 degrees.

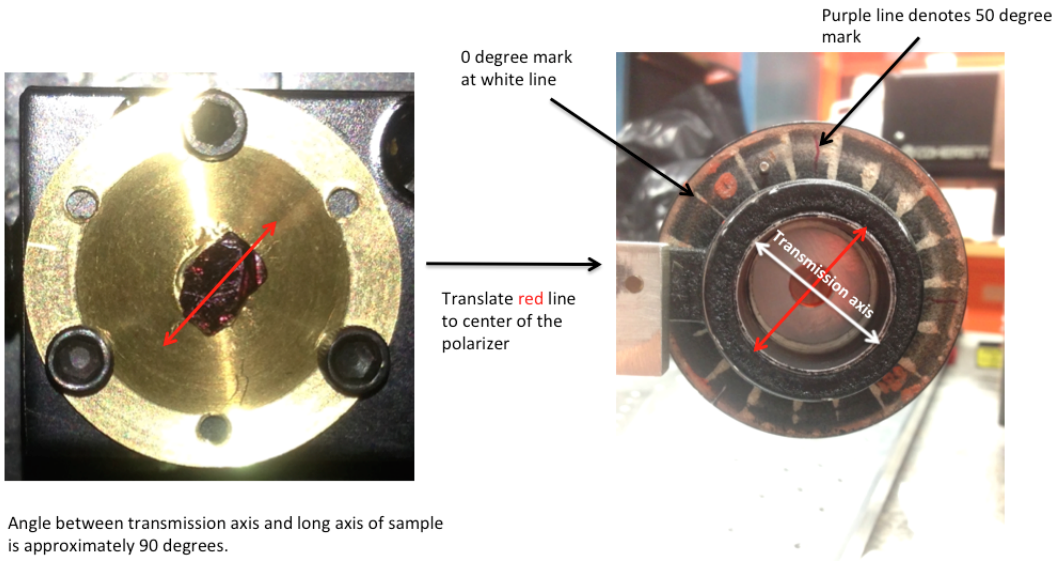

Figure 4.16: **Left**: Sample I33sc2 mounted for reflection measurement. **Right**: Transmission axis location on polarizer connecting 0 and 180 degrees. Take note that the polarizer is in its **0 degree** position as explained in Figure 4.17 **Left image**.

As the polarization vector of the light rotates (this is accomplished by rotation of the polarizer in intervals of $\sim 10^o$ as seen in Figure 4.17), it is reflected off of the sample[13] with different intensity.

[13]The sample holder is cone shaped in order to reflect light away from the detector so it doesn't contribute to the measured intensity.

Figure 4.17: **Left image:** polarization angle of **0 degrees**. **Centre image:** polarization angle of **10 degrees**. **Right image:** polarization angle of **20 degrees**.

The polarization vector reflects at highest intensity when it is oriented parallel to the higher conductive axis and reflects at lowest intensity when it is oriented parallel to the lower conductive axis. The intensity of the reflected light changes continuously as a function of polarizer rotation angle. Hence one expects a sine curve for reflected intensity as a function of polarization angle which is what was obtained[14] (see Figure 4.18).

[14]Axis alignment of an anisotropic single crystal can also be performed using Laue diffraction [56].

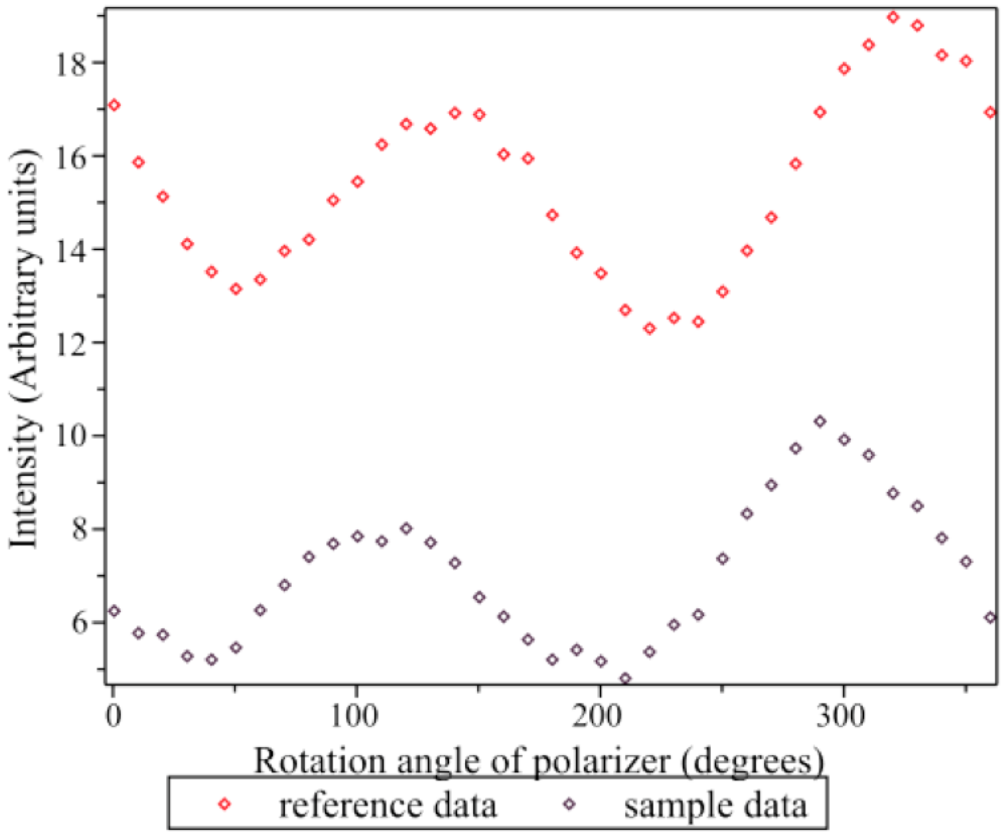

Figure 4.18: Sample and reference data sets.

A correction needs to be made because the light from the light source is somewhat polarized. Consequently, the measurement needs to be performed on a reference mirror to cancel the polarization of the source [91]. This gives two independent data sets as seen in Figure 4.18. The sample data is then divided by the reference data and the resulting reflectivity of the sample is obtained as a function of polarization angle (see Figure 4.19).

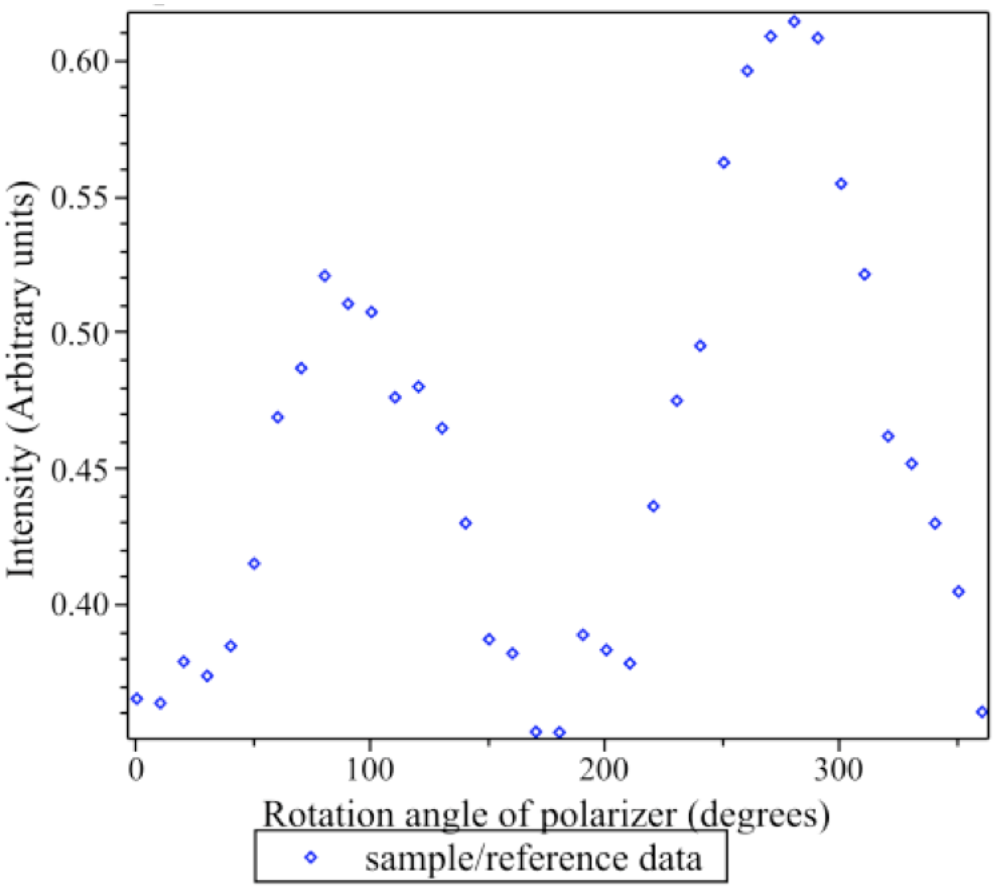

Figure 4.19: Sample data divided by the reference data.

Notice how the detector intensity peaks at roughly 90 degrees and 270 degrees. Comparing this result to Figure 4.16, we conclude that the low resistive axis is along the long axis of this single crystal; which was also the case in reference [12]. The peak at 270 degrees is larger than the peak at 90 degrees, this effect may be due to slight damage to the polarizer. This measurement was repeated 3 times (for each measurement the orientation of the sample was changed) and the results are consistent with the above findings.

4.2.3 Summary

The single crystal I33sc2 has been shown to be superconducting using the various tests: resistance as a function of temperature (Figure 4.7), determination of H_{C1} and H_{C2} (Figure 4.11), DC susceptibility (Figure 4.12) and AC susceptibility (Figure 4.13). Its orientation has been determined via single crystal X-ray diffraction and optical anisotropy techniques. The a-crystallographic lattice parameter is perpendicular to the plane of the single crystal and the b-crystallographic lattice parameter is parallel to the long axis of the single crystal.

Chapter 5

Results and Discussion:

Rubidium Molybdenum Oxide

In section 5.1 we give an overview of the various anomalous properties of the lilac brown single crystals found in the flux of the growth with Rb substituted for Li (i.e. batch III.33_{Rb}) and provide motivation for the synthesis of polycrystalline rubidium doped molybdenum dioxide. Section 5.2 will provide evidence for the superconductivity of polycrystalline rubidium doped molybdenum dioxide.

5.1 III.33_{Rb} Lilac Brown Single Crystals

Molybdenum dioxide MoO_2 or tugarinovite (naturally occurring MoO_2) typically has three single crystal allotropes which appear lilac brown in colour and form platelets, rectangular prisms and in some cases polyhedral shaped crystals [23, 35, 37, 95–97]. There were three main types of lilac brown single

crystals obtained in the flux of $III.33_{Rb}$. The first type were thick bar shaped crystals LBAR with average dimensions $1.5 \times 0.4 \times 0.4$ mm^3. The second type of crystal was lilac brown polyhedral POLY (avg. dimensions $0.5 \times 0.3 \times 0.3$ mm^3) and the third type were small lilac brown bar shaped crystals SBAR (avg. dimensions $1 \times 0.1 \times 0.1$ mm^3).

5.1.1 Resistivity of LBAR

The resistivity was measured for four lilac brown single crystals as a function of temperature. Two lilac brown single crystals from batch $III.33_{Rb}$ were measured and had approximate dimensions $\sim 1.5 \times 0.4 \times 0.4$ mm^3 (LBAR). Two lilac brown single crystals from batch $IV.33_K$ were measured and had approximate dimensions $\sim 3 \times 0.6 \times 0.6$ mm^3. These samples were connected using a four probe configuration as outlined in section 4.1. The resistivity of molybdenum dioxide is metallic from 300K$\rightarrow$ 2K [5, 29, 37]. All tested LBAR crystals[1] exhibited this behaviour (see Figure 5.1).

[1]Only some LBAR crystals were tested and hence could still exhibit resistive characteristics similar to SBAR and POLY, see Section 5.1.2.

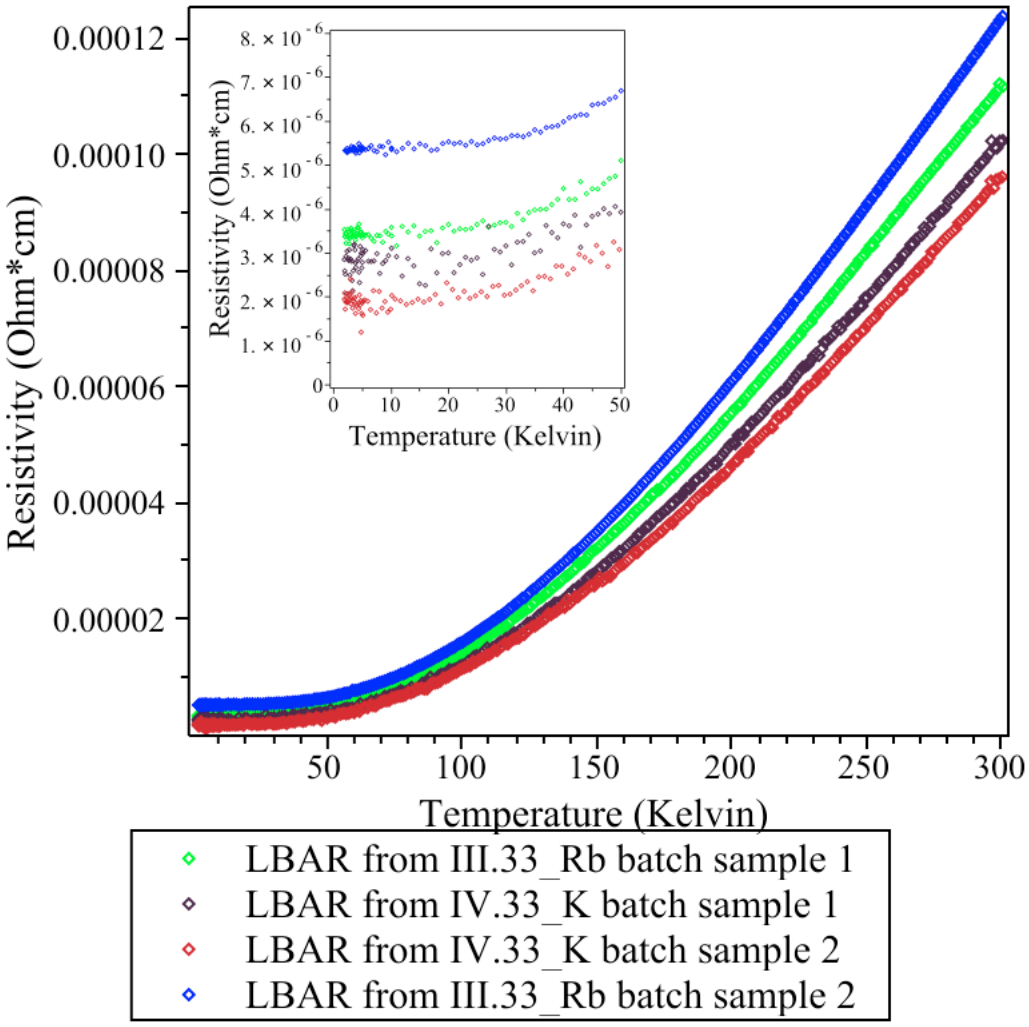

Figure 5.1: Resistivity as a function of temperature for four lilac brown single crystals, two from the III.33$_{Rb}$ batch and two from the IV.33$_K$ batch. All four single crystals are good conductors.

5.1.2 Resistance of POLY and SBAR

The POLY and SBAR single crystals displayed[2] insulating behaviour from 230−270K and then metallic behaviour from 2−230K with an anomalous transition at 94K (see Figure 5.2).

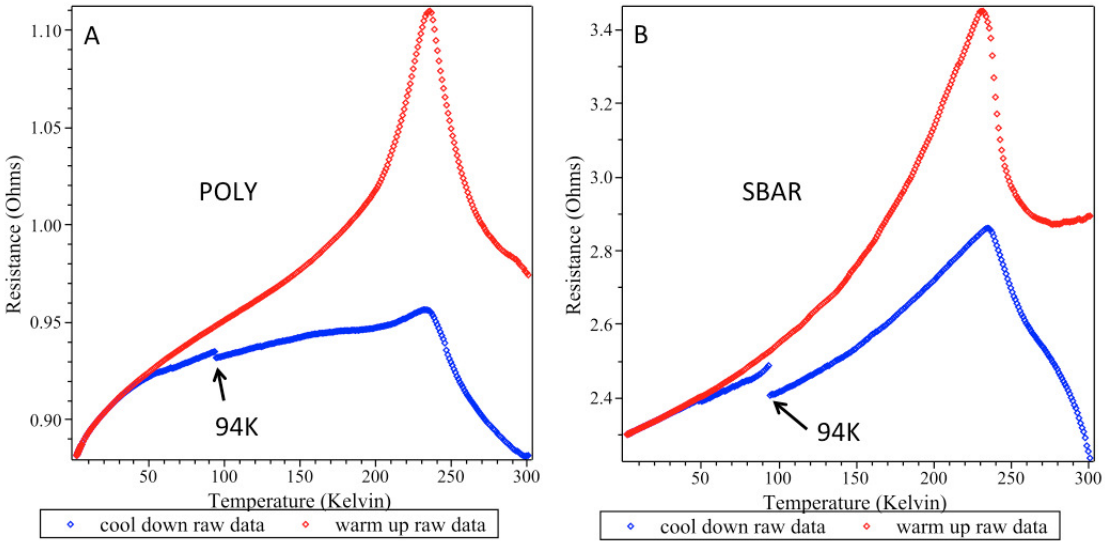

Figure 5.2: Resistance as a function of temperature for **A**: a POLY sample and **B**: an SBAR sample in zero applied magnetic field (before application of any applied magnetic field).

The 94K→93K transition is present only during the cooldown (i.e. from 300→2K). A similar M/I transition was seen in polycrystalline $K_{0.05}MoO_2$ at 270K along with a 54K transition during only the cooldown [4]. The 54K transition in polycrystalline $K_{0.05}MoO_2$ looks similar in appearance to the 94K transition in POLY and SBAR as seen in Figure 5.2 . In addition, for the POLY and SBAR single crystals, the M/I transition at 230K displays magneto-resistive

[2]Not all POLY and SBAR crystals were tested and some could still exhibit resistive characteristics similar to LBAR.

behaviour (see Figure 5.3, which shows the magneto-resistance for a POLY single crystal).

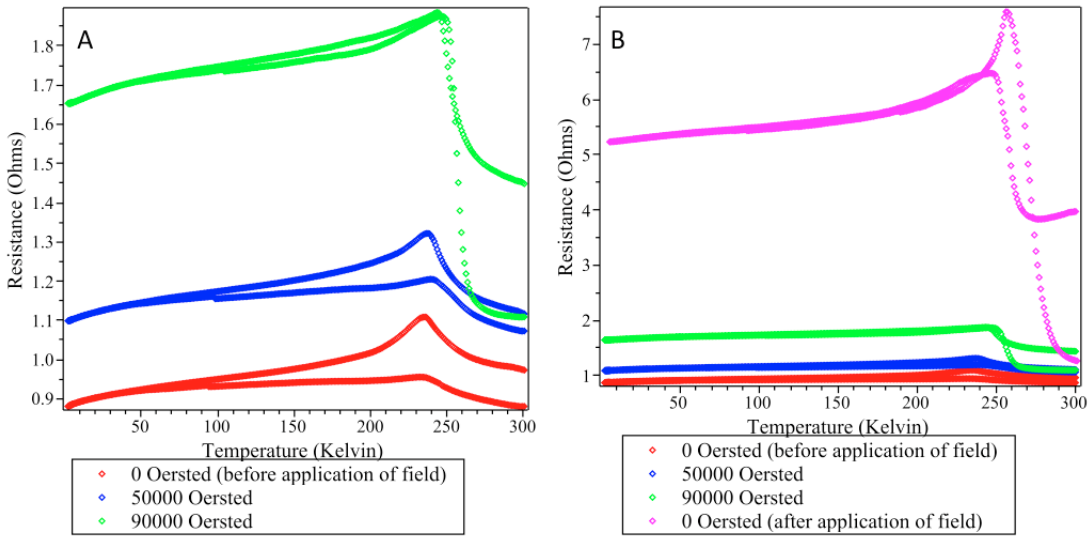

Figure 5.3: Figures **A** and **B** show resistance as a function of temperature at various applied fields and 1mA excitation current for a POLY single crystal from the $III.33_{Rb}$ batch.

In Figure 5.3 **A** notice how upon changing the field from 0 Oe to 50,000 Oe (red and blue curves) the curve is shifted vertically with little distortion. However, the transition near 230K distorts heavily when changing the field from 50,000 Oe to 90,000 Oe (blue and green curves). In Figure 5.3 **B** the magnetic field is turned off (pink curve), the curve further distorts and shifts vertically upwards. The same features from Figure 5.3 are seen in the resistance as a function of temperature data of SBAR at various applied magnetic fields.

5.1.3 Specific Heat of Lilac Brown Single Crystals

Specific heat was measured using a Quantum Design PPMS. A specific heat measurement as a function of temperature was performed on a mixture of LBAR and POLY type lilac brown single crystals from batch III.33$_{Rb}$. This measurement is shown in Figure 5.4.

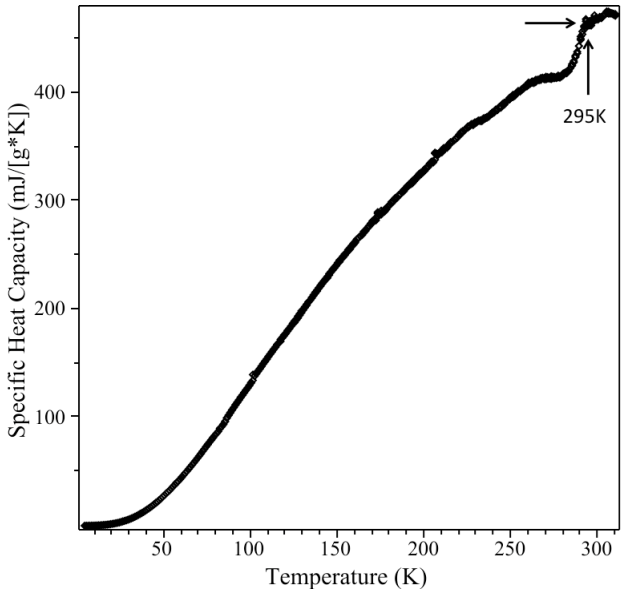

Figure 5.4: Specific heat as a function of temperature for a mixture of LBAR and POLY type lilac brown crystals from III.33$_{Rb}$ in the temperature range 310K to 2K.

Note the phase transition at ∼295K which may correspond to the onset temperature of a semiconductor transition as seen in the POLY and SBAR crystal types (see Figure 5.2). A similar transition in the specific heat was also seen at 306K for polycrystalline $K_{0.05}MoO_2$ [4].

In Appendix B, we show that the specific heat at low temperature is given as:

$$C(T) = \gamma T + \alpha T^3. \tag{5.1}$$

Using a least squares fit to the following equation

$$\boxed{C(T)/T = \gamma + \alpha T^2}, \tag{5.2}$$

one expects a linear relationship between C/T and T^2 at low temperature. A low temperature fit of the specific heat is shown in Figure 5.5 from 4.35K to 11.2K. Note that the result is reasonably linear.

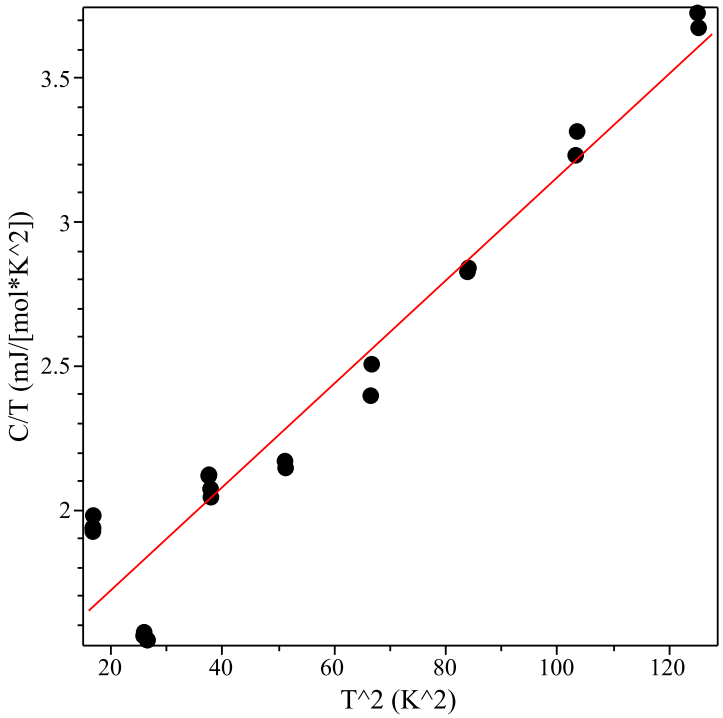

Figure 5.5: C/T as a function of T^2 at low temperature for a mixture of LBAR and POLY type lilac brown crystals from batch III.33$_{Rb}$.

Using equation (5.2) the coefficients were found to be $\gamma = 1.36\frac{mJ}{mol \cdot K^2}$ and

$\alpha = 0.0179\frac{mJ}{mol \cdot K^4}$. The minimum error for all 22 points is 0.82% and the maximum error is 2.8%. Polycrystalline $K_{0.05}MoO_2$ gave the following parameters: $\gamma = 1.5(2)\frac{mJ}{mol \cdot K^2}$, $\alpha = 0.93(1)\frac{mJ}{mol \cdot K^4}$ [4]. The parameter γ is very close for both compounds. However, comparing α between these two compounds one sees that it varies by an order of magnitude. Furthermore, 11K is not an unreasonably high temperature for this fit to be a good approximation. Pure molybdenum dioxide has a Debye temperature $\theta_D = 525K$ [4]. Assuming the crystal structures of the LBAR and POLY lilac brown single crystals are similar to that of pure MoO_2 and that therefore the Debye temperature is similar: we can calculate the upper limit for the T^2 behaviour of C/T. Experimentally, the T^2 term tends to hold for $T \leq \theta_D/50$ [82] and using $\theta_D = 525$K (for pure MoO_2) we obtain an upper bound for the temperature: $T_{max} \simeq \theta_D/50 = 525/50 \sim 11$K. Hence, for the data used in this plot ($\lesssim$11K), equation (5.1) is a valid approximation [82].

5.1.4 X-ray diffraction data

Assorted lilac brown single crystals[3] from batch $III.33_{Rb}$ were carefully inspected under a microscope for impurities[4] and ground thoroughly into a powder with a mortar and pestle (which was cleaned in aqua regia AR and rinsed with distilled water before use). The powder was then placed carefully on a cleaned glass slide (cleaned in AR and rinsed with distilled water before use). The powder dimensions were roughly $4 \times 4 \times 0.3$ mm^3 and a total of two Bragg Brentano XRD (see Figure C.2 for details) runs were performed over a two day period. Figure 5.6 compares the XRD data for the ground lilac brown crystals and polycrystalline $K_{0.05}MoO_2$ from the literature [4].

[3] i.e. a mix of LBAR, SBAR and POLY type single crystals.

[4] Even though the sample was leached, sometimes material remained stuck in fissures on the crystal surface. These fissures were inspected and mechanically cleaned to minimize impurities. If the fissures could not be mechanically cleaned then the single crystal was not used in this measurement.

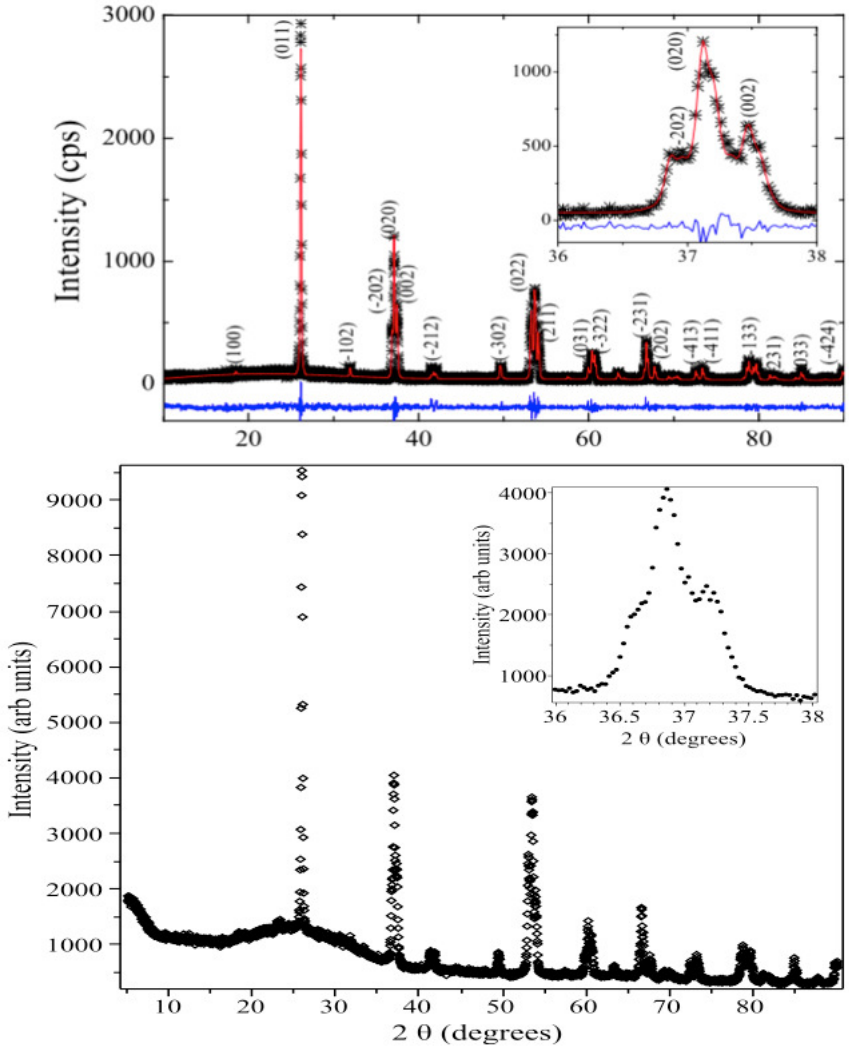

Figure 5.6: **UPPER DIAGRAM:** The x-ray powder diffraction data for polycrystalline $K_{0.05}MoO_2$ taken from [4]. Notice the head and shoulders pattern is centred slightly above 37^o. **LOWER DIAGRAM:** The xray powder diffraction data for assorted lilac brown single crystals of $III.33_{Rb}$. Notice the head and shoulders pattern is centred slightly below 37^o.

Notice how the peak at 54^o is $\sim 2/3$ the size of the peak at 37^o for the polycrystalline $K_{0.05}MoO_2$ data set. However these peaks in the data set for the lilac brown crystals are about the same size (with the peak at 54^o only slightly

smaller than the peak at 37^o). Figure 5.7 compares XRD data for the lilac brown crystals and polycrystalline $MoO_{2.05}$ from the literature [32].

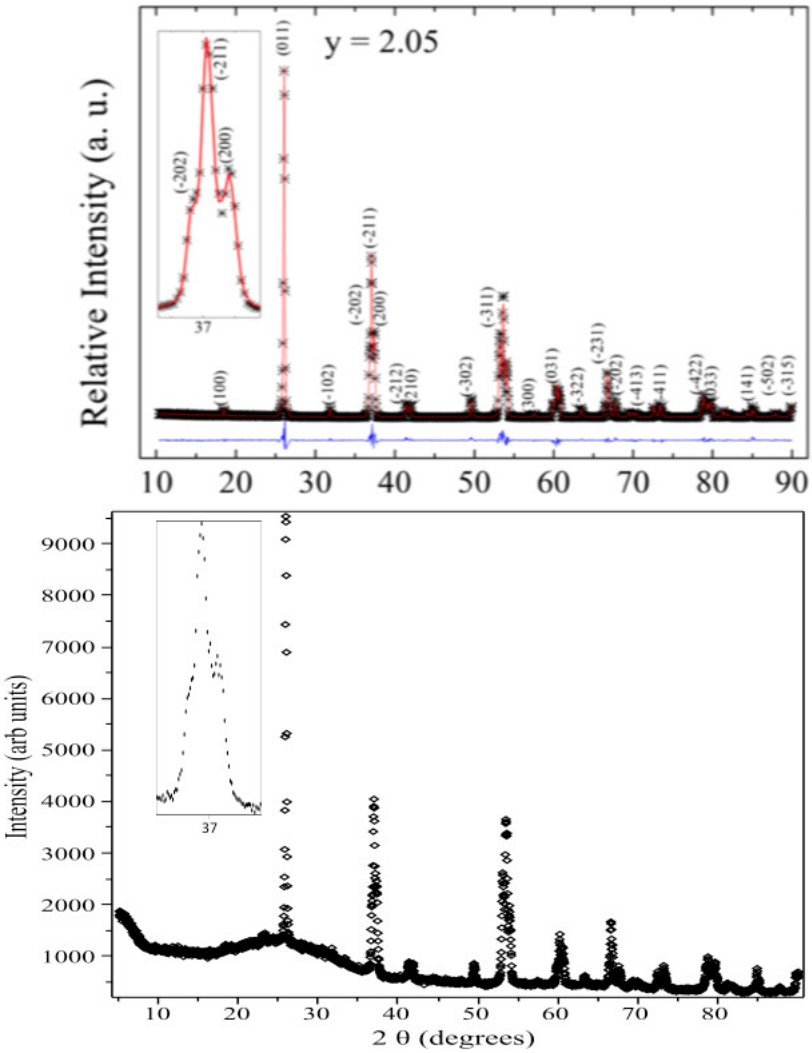

Figure 5.7: **UPPER DIAGRAM:** The x-ray powder diffraction data for polycrystalline $MoO_{2.05}$ taken from [32]. Notice the head and shoulders pattern is centred slightly above 37^o. **LOWER DIAGRAM:** The xray powder diffraction data for assorted lilac brown single crystals of III.33$_{Rb}$. Notice the head and shoulders pattern is centred slightly below 37^o.

Notice that in both the polycrystalline $MoO_{2.05}$ and the lilac brown single crystal

data sets, the peak at 54^o is only slightly smaller than the peak at 37^o. Finally, Table 5.1 compares the lattice parameters of lilac brown single crystals from $III.33_{Rb}$ to the lattice parameters of polycrystalline $K_{0.05}MoO_2$, tugarinovite and MoO_2. The 'a' and 'b' lattice parameters of the lilac brown single crystals from $III.33_{Rb}$ are slightly larger than those for the other compounds.

Table 5.1: X-ray data comparison between my powder data (first and second row) and various compounds.

Data set name	a(Å)	b(Å)	c(Å)	alpha(deg)	beta(deg)	gamma(deg)
$III.33_{Rb}$-purple_ refine_1	5.6273	4.8758	5.6465	90.0	120.935	90.0
$III.33_{Rb}$-purple_ refine_2	5.6278	4.8604	5.5404	90.0	119.728	90.0
polycrystalline $K_{0.05}MoO_2$ [4]	5.6082	4.8589	5.6264	90.0	120.929	90.0
Tugarinovite (MoO2) [23]	5.59	4.82	5.51	90.0	119.533	90.0
Moly. diox. (MoO2) [38]	5.6109	4.8562	5.6285	90.0	120.95	90.0

The XRD data from Figures 5.6 and 5.7 look fairly similar to the powder XRD data obtained for the lilac brown single crystals and all major peaks are present. One of the main differences is the formation of a head-and-shoulders pattern whose central peak is located at $\sim 36.9^o$ for the lilac brown single

crystals from $III.33_{Rb}$, $\sim 37.2^o$ for polycrystalline $K_{0.05}MoO_2$ and $\sim 37.1^o$ for polycrystalline $MoO_{2.05}$ (see Figures 5.6 and 5.7). This suggests that the crystal structure of the lilac brown single crystals are similar to that of both polycrystalline $K_{0.05}MoO_2$ and polycrystalline $MoO_{2.05}$. All three XRD patterns taken for the lilac brown single crystals from $III.33_{Rb}$ display the same head-and-shoulders pattern with central peak located at $\sim 36.9^o$.

Single crystal XRD powder diffraction was performed on a lilac brown single crystal from batch $III.33_{Rb}$ using a RIGAKU system with Bragg Brentano optics. The two measurements were tabulated (Table 5.1). During a crystal structure refinement a small figure of merit (FOM) defines a good phase set [92]. The weighted profile R-factor R_{wp} is proportional to the square root of the sum of squared differences between the measured and computed intensity values i.e. $\sim \sqrt{\sum_i (y_{C,i} - y_{M,i})^2}$, where $y_{C,i}$ are the intensity values computed from the model and $y_{M,i}$ are the measured intensity values, i denotes the corresponding value of 2θ the data was taken at [93]. χ^2 is proportional to $\sim (1/N) \sum_i (y_{C,i} - y_{M,i})^2$ where N is the total number of data points. The XRD data labelled '$III.33_{Rb}$-purple_refine_1' was refined using PDXL (FOM: 0.816, $R_{wp} = 6.7\%$, $\chi^2 = 3.69$). The XRD data labelled '$III.33_{Rb}$-purple_refine_2' was also refined using PDXL (FOM: 1.345, $R_{wp} = 5.6\%$, $\chi^2 = 2.58$). 'Tugarinovite' data (naturally occurring mineral) was taken from reference [23], 'Moly. diox.' data (synthetic) was taken from reference [38] and 'polycrystalline $K_{0.05}MoO_2$' data ($R_{wp} = 12.24\%$ and $\chi^2 = 1.47$) was taken from [4].

5.1.5 Characterization of $III.33_{Rb}$ Lilac Brown Single Crystals

In this section we discuss a measurement of inductively coupled plasma mass spectrometry (ICP-MS) on the lilac brown single crystals. 23 SBAR and POLY type single crystals (taken from the batch $III.33_{Rb}$) were carefully inspected under a microscope to make sure they were clean. The total mass of these crystals was ∼3mg. The crystals were crushed into powder and dissolved in AR. Inductively coupled plasma mass spectrometry ICP-MS performed at Brock was used to classify[5] the approximate amount of Rb^{85} doping in the SBAR and POLY single crystals. The single crystal were ground into a powder and dissolved into aqua regia. The solution is then sprayed as an aerosol into an inductively coupled plasma torch where the atoms are ionized and then analyzed in the mass spectrometer [94]. The results suggest that the crystal composition is[6] $Rb_{0.00007}MoO_{2-\delta}$. We need to subtract some unknown parameter δ here because ICP-MS cannot give percent composition of oxygen. $\delta \sim 0$ is a good approximation from the XRD powder data given in Figures 5.6, 5.7 and Table 5.1. It seems that all of the sample did not dissolve in aqua regia which is usually the case with a high concentration of molybdenum [99]. Furthermore, this experiment only confirms the presence of rubidium in some of the single crystals and is by no means a complete test to verify the rubidium doping ratio in the

[5]ICP-MS is able to detect composition to the order of 1 ppt (part per trillion) [98].

[6]Since the fitting parameter for the slope of the Rb^{85} calibration curve was A=7478.00±931.843 counts/(s·ppb) this gives an error of about 12%. Hence, this infers an Rb doping between $Rb_{0.00006}MoO_{2-\delta}$−$Rb_{0.00008}MoO_{2-\delta}$.

SBAR and POLY samples shown in Figures 5.2 and 5.3.

5.2 Polycrystalline Rb Doped Molybdenum Dioxide

In this section we show that polycrystalline $Rb_{0.03}MoO_{2-\delta}$ is superconducting with a small superconducting volume fraction. We do this by analysing the FC/ZFC data (Figure 5.8), magnetization as a function of applied field data (Figure 5.9) and resistivity as a function of temperature data (Figures 5.10 and 5.11). Both susceptibility measurements were performed on a Quantum Design MPMS. Both resistivity measurements were performed on a Quantum Design PPMS. The four probe setup, explained in Section 4.1, was used for the resistivity measurements.

FC and ZFC magnetization as a function of temperature measurements were performed on a cylindrical shaped sample of polycrystalline $Rb_{0.03}MoO_{2-\delta}$ at 50 Oe (see Figure 5.8).

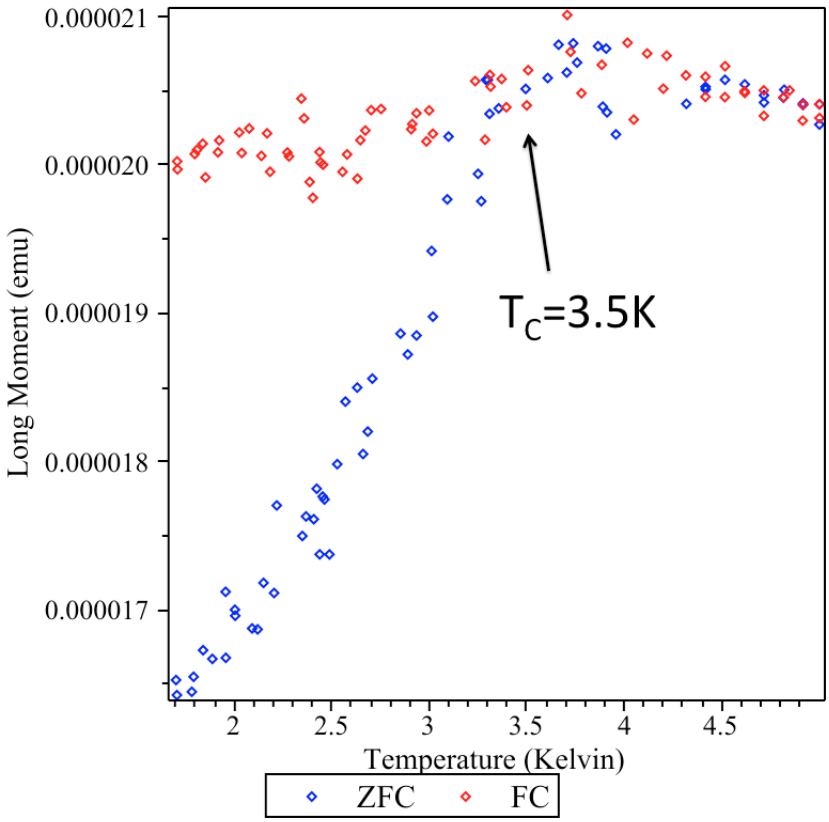

Figure 5.8: ZFC/FC measurements of susceptibility as a function of temperature for superconducting polycrystalline $Rb_{0.03}MoO_{2-\delta}$ at 50 Oe. The sample was in the shape of a cylindrical disk with applied field perpendicular to the flat surface. Demagnetization was not calculated.

One can clearly see a transition at 3.5K. A ZFC magnetization measurement as a function of applied field was performed on the same cylindrical shaped sample of polycrystalline $Rb_{0.03}MoO_{2-\delta}$ at 1.7K (Figure 5.9).

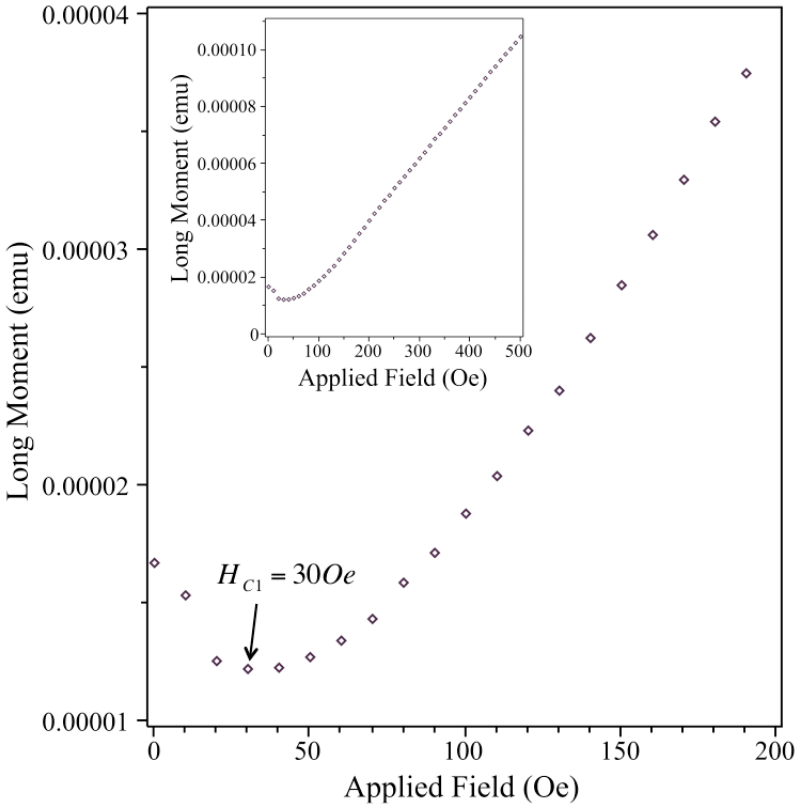

Figure 5.9: Magnetization as a function of applied field for superconducting polycrystalline $Rb_{0.03}MoO_{2-\delta}$ at 1.7K. Upper inset is the full data set, notice a linear trend from 150 Oe to 500 Oe. The sample was in the shape of a cylindrical disk with applied field perpendicular to the flat surface. Demagnetization was not calculated.

We cannot properly determine H_{C2} from the data assuming the superconducting portion of the sample is Type 2 with H_{C1}= 30 Oe and that the paramagnetic contribution is increasing linearly with applied field. The majority of the sample is paramagnetic which can be seen by the positive magnetization for applied fields $0 < H < 90$ Oe and the positively sloped linear response for applied fields > 90 Oe (see upper inset for full data set). Resistivity was measured as a

function of temperature for a bar shaped sample from 300K to 2K (Figure 5.10).

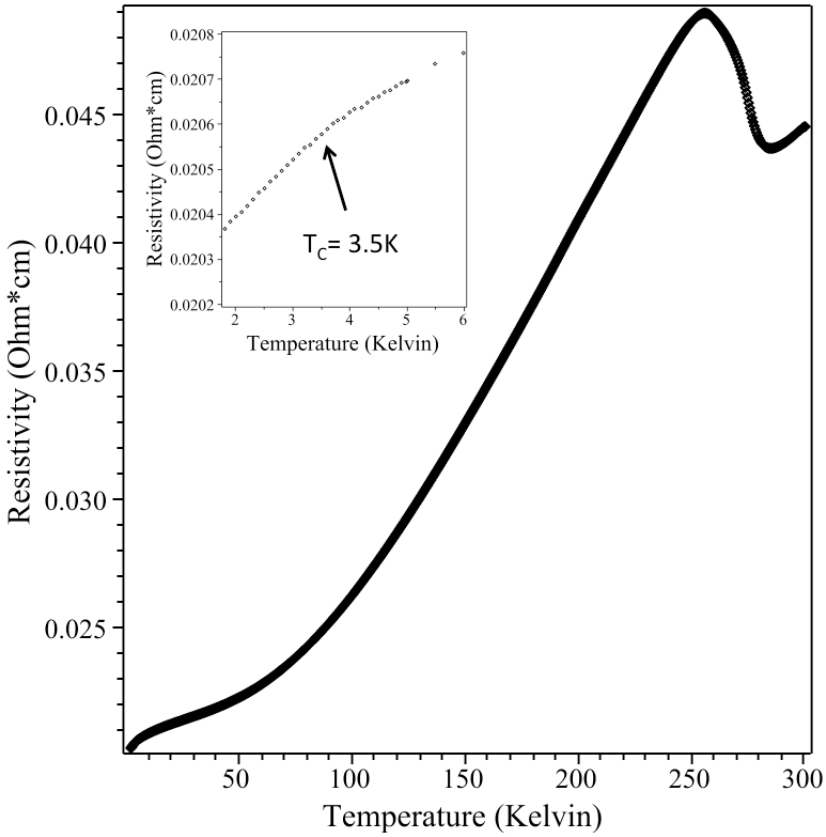

Figure 5.10: Resistivity as a function of temperature for superconducting polycrystalline $Rb_{0.03}MoO_{2-\delta}$. In the upper inset notice an increase in the slope for temperatures <3.5K.

One can clearly see a transition at 3.5K. The slight increase of the $\rho(T)$ slope below 3.5K (upper left inset) implies a small superconducting volume fraction. In addition, the transition at T∼260K is similar in appearance to that found in POLY and SBAR as seen in Figure 5.2. The height of this peak at T∼260K was suppressed as the sample was thermally cycled. Lastly, resistivity was measured as a function of temperature on polycrystalline $Rb_{0.03}MoO_{2-\delta}$ using various applied fields in the temperature range 1.9K to 5K (Figure 5.11).

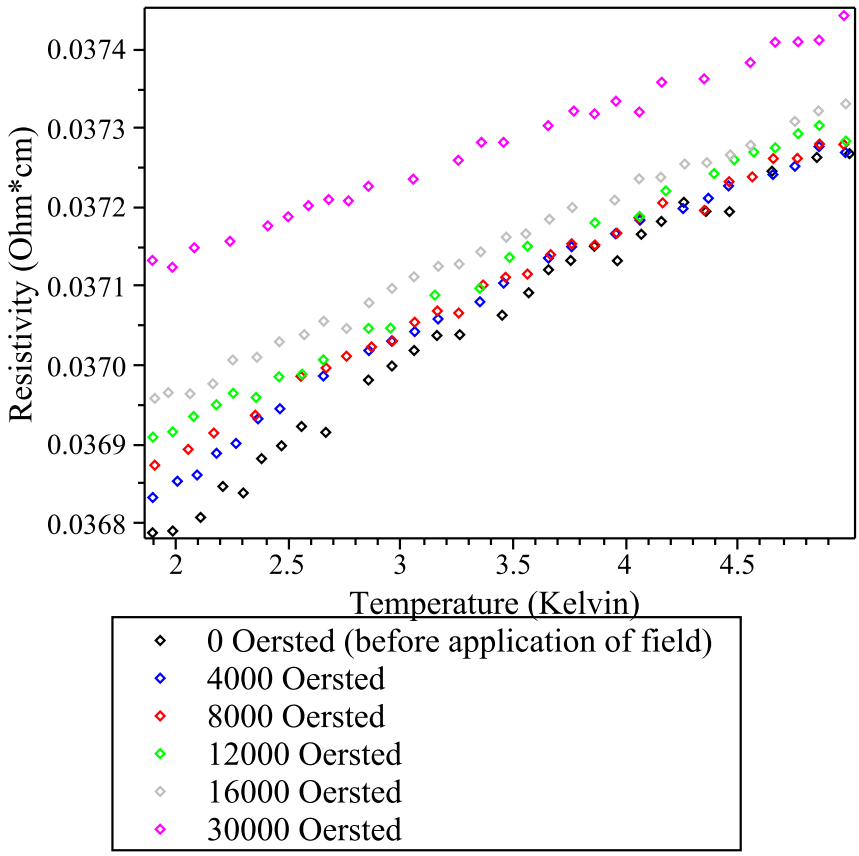

Figure 5.11: Resistivity as a function of temperature for superconducting polycrystalline $Rb_{0.03}MoO_{2-\delta}$ at various applied fields.

One can clearly see the complete suppression of the superconducting transition at 3.5K as the applied field is increase from 0 Oe $\rightarrow$ 30,000 Oe. A slight slope seems to be visible at 16,000 Oe which gives us an approximate value for the upper critical field in the range 16,000 Oe $\leq H_{C2} \leq$ 30,000 Oe. Also, the sample seems to exhibit magnetoresistance which can be seen by an increase in sample resistivity with increasing applied field.

Chapter 6

Conclusions and Future Work

The temperature gradient flux technique was used to successfully grow single crystals of LiPB. A large LiPB single crystal 'I33sc2' (dimensions: $4.7 \times 3.0 \times 1.2$ mm^3) was grown using doping parameter $n = 0.33$ and confirmed to be superconducting. In future work I33sc2 will be used for polarized reflectivity measurements in the superconducting state (below $T_C \sim$1.85K) similar to the analysis done in the literature for the normal state [51, 80]. We also performed resistivity measurements on a non-superconducting single crystal (grown with doping parameter $n = 0.30$) along the b-crystallographic axis. For this single crystal, we found the maximum value of the energy gap to be 2 meV$\pm$0.1 meV at 9.16K, which differs from the accepted literature value of $\sim$1 meV at 5-6K [1, 2]. The optical properties of the non superconducting LiPB single crystals will be studied in future work to verify the optical gap of 2 meV at 9.16K. A more rigorous approach should be used to find $E_g(T)$ which takes into account the low

dimensionality of the system. One could also try expressing[1] $\tau := \tau(T)$.

The temperature gradient flux technique, with doping parameter $n = 0.33$, was used to successfully grow lilac brown single crystals. These lilac brown single crystals are similar in appearance to naturally occurring single crystal MoO_2 (i.e. tugarinovite). Two types of lilac brown single crystals of interest were polyhedral (denoted as 'POLY', having approximate dimensions: $0.5 \times 0.3 \times 0.3$ mm^3) and small bar shaped (denoted as 'SBAR', having approximate dimensions: $1 \times 0.1 \times 0.1$ mm^3). These single crystals exhibited anomalous properties in the resistivity and specific heat. The anomalous properties include a M/I transition at 250K and a small phase transition in the resistivity at 94K. Assorted lilac brown single crystals were studied with powder X-ray diffraction (XRD) and refined twice using PDXL software. The lattice parameters obtained for both refinements were a=5.6273Å, b=4.8758Å, c=5.6465Å and a=5.6278Å, b=4.8604Å, c=5.5404Å. These lattice parameters can be compared to synthetic MoO_2 (having lattice parameters a=5.6109Å, b=4.8562Å, c=5.6285Å) and tugarinovite (having lattice parameters a=5.59Å, b=4.82Å, c=5.51Å). The lilac brown single crystals have slightly larger 'a' and 'b' lattice parameters than MoO_2 and tugarinovite. As future work it would be of interest to measure single crystal XRD on POLY and SBAR single crystals which will provide details on the lattice of the single crystals including: site ordering details, bond angles, bond lengths, and unit cell dimensions [100].

Polycrystalline rubidium molybdenum dioxide $Rb_{0.03}MoO_{2-\delta}$ was prepared by

[1] τ is the mean time an electron travels between two consecutive collisions.

solid-state reaction. Using various experimental techniques this compound is superconducting with a T_C=3.5K. The resistivity as a function of temperature data of polycrystalline $Rb_{0.03}MoO_{2-\delta}$ shows a M/I transition at ∼260K. This M/I transition is similar to the one found for the lilac brown single crystals from the $III.33_{Rb}$ batch, but lacks a phase transition at 94K. Furthermore, the M/I transition at ∼260K was suppressed as the sample was thermally cycled (from 2K to 400K) which could correspond to the sample losing or gaining oxygen. As future work it would be of interest to make samples with various doping concentrations of Rb and possibly various annealing techniques in $O_{2,gas}$ and $H_{2,gas}$ to try and increase the superconducting volume fraction of the material.

Appendices

Appendix A

AC susceptibility

This appendix will explain the experimental apparatus associated with an AC coil, a basic explanation of the physics of an AC coil (Section A.1) and how an AC coil is designed (Section A.2). The AC susceptibility measurement was performed with a Quantum Design PPMS, where the internal workings of the system are given in Figure A.1. The sample was placed inside the AC coil located within a low temperature probe (Figure A.2). The experimental apparatus used for the AC susceptibility measurement is shown in Figure A.3.

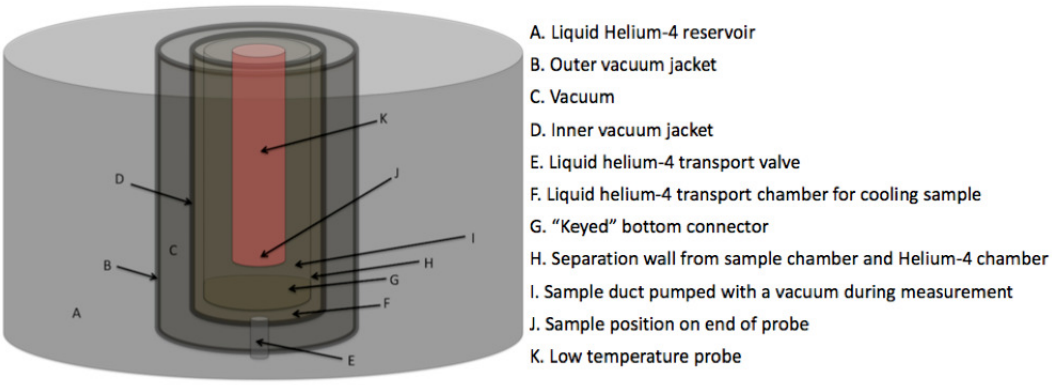

Figure A.1: The internal workings of the PPMS measurement space. The PPMS was used for resistivity, AC susceptibility and specific heat measurements. Reproduced from [102].

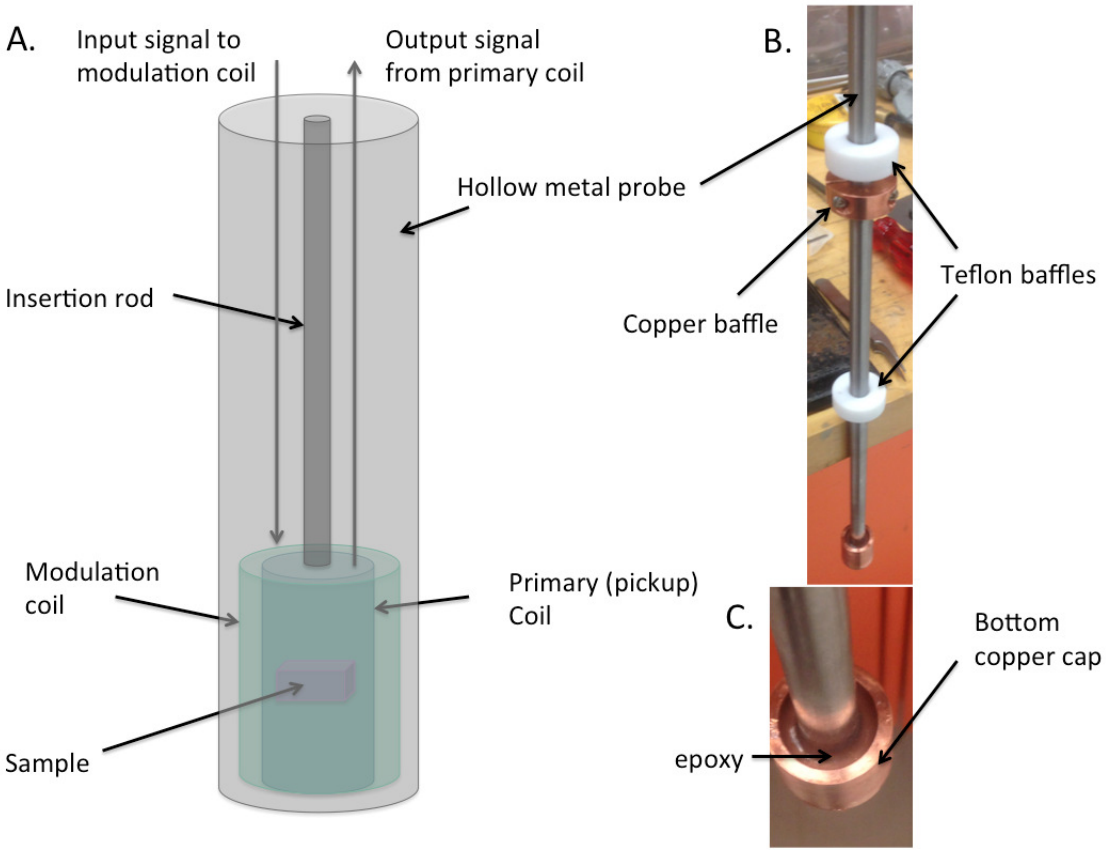

Figure A.2: A. Schematic inside the low temperature probe. B. Schematic of the lower half of the low temperature probe. C. Bottom section of the low temperature probe.

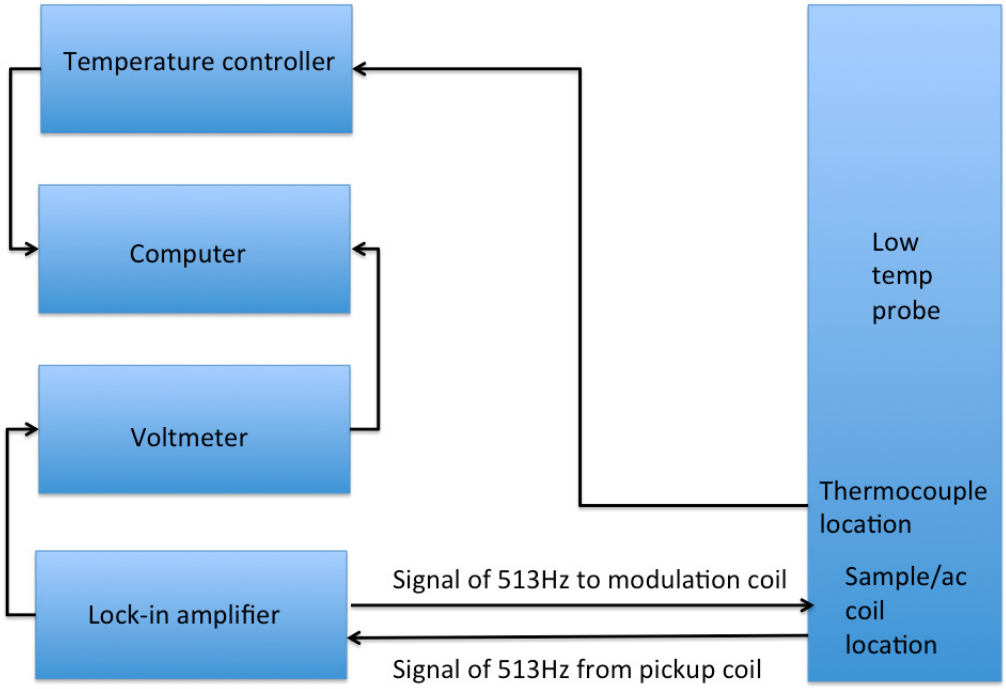

Figure A.3: Experimental apparatus used for AC susceptibility measurement.

A.1 Overview of the physics of an AC coil

To reduce noise in the pickup coil, one must ensure that its magnetic flux Φ_P is nearly zero inside [101]. To understand the need for the condition $\Phi_P = 0$ in the primary coil one must understand the concept of inductance. Inductance is the generation of an electromotive force (emf) produced by a changing current. There are two specific types of inductance, **mutual inductance** and **self-inductance** [103]. **Mutual inductance** occurs when a circuit element has a non-zero changing current which induces an emf in a nearby circuit element. **Self-inductance** occurs when a circuit element experiences a changing current which induces an emf in itself. Both self- and mutual inductance contribute to

the net voltage experienced in the primary coil. Satisfying the condition $\Phi_P = 0$ in the primary coil eliminates the primary coil self-inductance and thus only the mutual inductance of the sample on the primary coil will contribute to the net voltage in the primary coil. The placement of the modulation and primary coils for the AC susceptibility apparatus is illustrated in Figure A.4. The equivalent circuit setup for the AC susceptibility apparatus is given in Figure A.5.

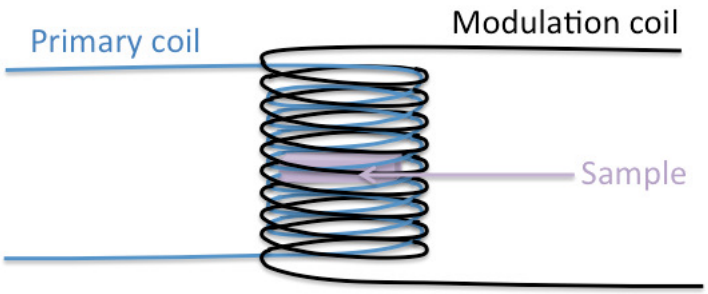

Figure A.4: Schematic showing the experimental arrangement between the primary coil, modulation coil and the sample. Notice here that the modulation coil is wrapped around the primary coil and the sample is located inside the primary coil.

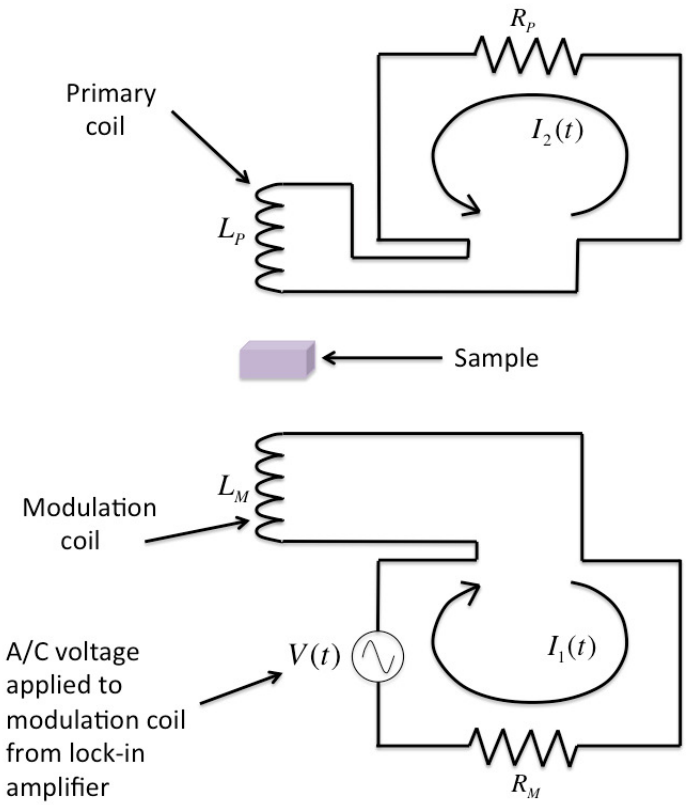

Figure A.5: Schematic showing an equivalent circuit setup between the primary coil, modulation coil and the sample. Ideally, all magnetic flux lines emanating from the sample Φ_S point along the coaxial z-axis of the primary and modulation coils.

To find the voltage across the primary coil we consider Figure A.5. Applying Kirchhoff's Voltage Law to the upper loop, we obtain [104]

$$-V_P - V_{P,self} + V_{Mod} + V_S = 0, \tag{A.1}$$

where V_P is related to the voltage drop across the resistor R_P and the inductive reactance of the primary coil, $V_{P,self}$ is the voltage associated with the self-inductance of the primary coil, V_{Mod} is the voltage produced in the primary

coil due to the modulation coil and V_S is the voltage produced in the primary coil due to the sample. Equation (A.1) becomes

$$-V_P - L_P\frac{dI_2}{dt} + M_{PMod}\frac{dI_1}{dt} + \frac{d\Phi_S}{dt} = 0, \tag{A.2}$$

where L_P is the self-inductance of the primary coil, M_{PMod} is the mutual inductance between the primary and the modulation coils, Φ_S is the induced magnetic flux of the sample originating from the magnetic field of the modulation coil[1]. From Figure A.4 one can see that all of the magnetic field created by the modulation coil passes through the primary coil. This implies that[2] $M_{PMod} = \sqrt{L_P L_{Mod}}$ [105]. The self-inductance of the primary coil is $L_P = N_P\Phi_P/I_2$. Since $\Phi_P = 0$, we have $L_P = 0$ and $M_{PMod} = 0$, and equation (A.2) becomes

$$-V_P + \frac{d\Phi_S}{dt} = 0. \tag{A.3}$$

Writing equation (A.3) in terms of the induced voltage of the sample in the primary coil V_S, we obtain

$$-V_P + V_S = 0, \tag{A.4}$$

and thus

[1] All magnetic flux emanating from the sample Φ_S is captured by the primary coil.

[2] The coefficient in-front of the square root is generally between 0 and 1. We have the coefficient 1 here because the modulation coil is wrapped directly on top of the primary coil so that all magnetic flux created by the modulation coil is captured by the primary coil.

$$V_P = V_S. \tag{A.5}$$

Therefore, the voltage measured in the primary coil V_P is equal to the induced voltage of the sample in the primary coil. Equation (A.5) is not exact, as there is always a remnant voltage induced in the primary coil due to the modulation coil V_{Mod}. However, for practical purposes one can design modulation and primary coils such that[3] $V_{Mod} \ll V_S$.

A.2 Design of an AC coil

A typical AC susceptibility coil design consists of a primary (also called "pickup") coil and a modulation coil. The pickup coil was wound using 40 AWG enamelled copper wire and the modulation coil was wound with a slightly thicker wire gauge. The primary coil was wound first using a total of 6 layers (see Table A.1 for details). The primary coil should be slightly larger than the sample and is responsible for picking up the magnetic response of the sample. The modulation coil, having a total of 4 layers (see Table A.2 for details), was wound directly over top of the primary coil . The modulation coil creates a certain time dependent magnetic field $H(t) = H_o \cos(\omega t)$. The stipulation for an AC coil is given by the following relation

$$\Phi_P = B_P A = 0, \tag{A.6}$$

[3]See equation (A.15) for more details.

where B_P is the magnetic field induced in the primary coil, Φ_P is the induced magnetic flux in the primary coil and A is the inner cross-sectional area of the primary coil. For a long solenoid B_P takes on the following form

$$B_P \simeq \frac{\mu_o N I_{induced}}{l}, \tag{A.7}$$

where N is the total number of turns in the primary coil and $I_{induced}$ is the current induced in the primary coil due to self-induction. Substituting equation (A.7) into (A.6), we obtain

$$\Phi_P = \frac{\mu_o N I_{induced}}{l} A = 0. \tag{A.8}$$

Equation (A.7) can be generalized to each layer of the primary coil. Hence for six layers of turns equation (A.8) becomes

$$\Phi = \frac{\mu_o I_{induced}}{l} \left(N_1 A_1 + N_2 A_2 + N_3 A_3 + N_4 A_4 + N_5 A_5 + N_6 A_6\right) = 0, \tag{A.9}$$

which implies that

$$\left(N_1 A_1 + N_2 A_2 + N_3 A_3 + N_4 A_4 + N_5 A_5 + N_6 A_6\right) = 0. \tag{A.10}$$

The area ($A_i = \pi r_i^2$) gets larger with the addition of each layer. Here, r_i is the radius of the i^{th} solenoid layer. Therefore, equation (A.10) takes the following form

$$N_1 r_1^2 + N_2 r_2^2 + N_3 r_3^2 = -\left(N_4 r_4^2 + N_5 r_5^2 + N_6 r_6^2\right). \tag{A.11}$$

The negative sign indicates that the outer three layers need to be wound in the opposite direction of the inner three layers (see Table A.1).

Table A.1: Measured parameters for the primary coil

Layer	Diameter of primary coil (mm)	Number of turns (N)	Turn direction
1	5.58	89.5	counter-clockwise
2	5.85	86.1	counter-clockwise
3	6.10	85.1	counter-clockwise
4	6.34	89.2	clockwise
5	6.60	85.3	clockwise
6	6.83	to be determined	clockwise

In Table A.1, the last row has yet to be determined. Substituting all parameters from Table A.1 into equation (A.11) and solving for N_6, we obtain

$$N_6 \simeq 34 turns. \tag{A.12}$$

A modulation coil was then wound directly over top of the primary coil. The modulation coil has the same length as the primary coil. Four layers were wound all in the same direction in order to generate a suitable magnetic field. The parameters for the modulation coil are recorded in Table A.2.

Table A.2: Measured parameters for the modulation coil

Layer	Diameter of modulation coil (mm)	Number of turns (N)	Turn direction
1	6.91	61.7	counter-clockwise
2	7.28	59.9	counter-clockwise
3	7.41	59.4	counter-clockwise
4	7.73	58.7	counter-clockwise

Once the AC coil was completed, its accuracy was tested using a lock-in amplifier. To understand how to check for good accuracy of a pickup coil consider the following argument. Consider a signal in the modulation coil given by $H(t) = H_o \cos(\omega t)$, then the induced electromotive force (emf) in the pickup coil is given by

$$V_P = -N\frac{d\Phi}{dt}, \tag{A.13}$$

where ideally $V_P = 0$ (without a sample) upon substitution of equation (A.9) into equation (A.13). We expect, in general without a sample inside the coil that the remnant voltage produced in the primary coil due to the modulation coil (see the third term in equation (A.1)) will be given by

$$V_{Mod} = V_o sin(\omega t), \tag{A.14}$$

where V_o is a constant and the signal is shifted by 90 degrees (because the voltage leads the current by 90 degrees in a purely inductive circuit[4]). To test the

[4]Recall the modulation coil outputs a magnetic field of $H(t) = H_o \cos(\omega t)$, thus the measured voltage in the primary coil will be $\sim \sin(\omega t)$

sensitivity of the pickup coil we applied a voltage to the modulation coil (without a sample) at 513 Hz and then measured the response of the pickup coil. If the value of $V_o \ll 1nV$ for any reasonable applied voltage in the modulation coil then the AC coil is sufficiently accurate for experimental purposes. In our case we turned up the sensitivity of the lock-in amplifier and confirmed that indeed $V_o \ll 1nV$. Hence, the emf in a well designed AC coil (with sample) takes the following form:

$$\boxed{V_P = V_o sin(\omega t) + V_S \simeq V_S}. \tag{A.15}$$

Appendix B

Specific Heat

B.1 Debye Model $C \sim T^3$

In this appendix we derive the T^3 dependence of the specific heat due to atomic vibrations. Atomic vibrations in a solid can be thought of as a wave (when one atom moves it pushes its neighbour, this neighbour atom pushes its neighbour, etc.). Vibrational waves move at the speed of sound with angular frequency given by [82, 106]

$$\omega = \upsilon k. \tag{B.1}$$

It can be shown that the energy of a 1D quantum oscillator is given by [107]

$$\epsilon = \hbar\omega \left(n + \frac{1}{2} \right), \tag{B.2}$$

where n is the energy level ($n = 0, 1, 2, ...$), $\hbar = h/2\pi$ is the reduced Planck

constant, $\omega = \sqrt{k/m}$ is the angular frequency, k is the spring constant and m is the mass of the atom. The canonical partition function of this system becomes [108]

$$Z = \sum_n e^{-\beta\epsilon_n} = \sum_n e^{-\beta\hbar\omega\left(n+\frac{1}{2}\right)}, \tag{B.3}$$

where $\beta = 1/k_B T$. The average internal energy of a 1D oscillator can be expressed as [106, 108]

$$\langle\epsilon\rangle_{1D} = -\frac{1}{Z}\frac{\partial Z}{\partial\beta} = \hbar\omega(n_B(\beta\hbar\omega) + 1/2)), \tag{B.4}$$

where the Bose factor $n_B(\beta\hbar\omega) = 1/(e^{\beta\hbar\omega} - 1)$ tells us the expected level of excitation at a given temperature[1]. Before proceeding with the calculation, we make the following assumptions [106, 108]:

- Thermal energy is caused by long wavelength vibrations.
- Sound waves can be quantized similar to light waves.
- The dispersion relation described by equation (B.1) is valid.
- Vibrations of atoms have 3 polarizations (2 transverse and 1 longitudinal).
- The velocity of sound is independent of polarization direction[2].
- The velocity of sound is independent of direction of travel in a solid[3].

[1] Hence if at a particular value of temperature T, the Bose factor $n_B(\beta\hbar\omega) = 4$, then on average at temperature T the system is at an excitation state of 4.

[2] This is not true in general as almost always the transverse modes have lower velocities than the longitudinal mode.

[3] In general this is also not true.

The expectation value of total energy is the sum over all vibrational wave modes (or oscillators) in the system [106, 108]

$$\langle \epsilon \rangle_{total} = 3 \sum_{\vec{k}} \langle \epsilon \rangle_{1D} = 3\hbar \sum_{\vec{k}} \omega_{\vec{k}} (n_B(\beta \hbar \omega_{\vec{k}}) + 1/2)), \tag{B.5}$$

where the multiplicative pre-factor 3 takes into account the 3 polarizations of sound.

Consider a 1D "box" of length $L = Na$, where N is the number of unit cells in the crystal and a is the lattice parameter. Next wrap the box into a circle and choose L such its radius is 1. Hence we now have a periodic box of length L. Any point on this circle can be described by $z = e^{ikx}$. Using Born-von Karman boundary conditions we obtain $z = e^{ikx} = e^{ik(x+L)}$ which implies that $e^{ikL} = 1$ and therefore $k = 2\pi n/L$, where $n = 0, 1, 2, ..., (N-1)$ (only sum to $N-1$ here because $n = 0$ and $n = N$ give the same position on the circle). Hence, the spacing between allowed k-values is $2\pi/L$ and the total allowed k-values are as follows [109]

$$k = 0, \frac{2\pi}{Na}, \frac{4\pi}{Na}, ..., \frac{2\pi(N-1)}{Na}, \tag{B.6}$$

which yields a total of N k-values. Hence the sum over all k-values can be replaced by the integral (in 3D)

$$\sum_k (1) = N = \frac{N}{\sigma_B} \sigma_B = \frac{N}{\sigma_B} \int d^3k = \frac{N\sigma}{(2\pi)^3} \int d^3k, \tag{B.7}$$

here σ_B is the volume of a unit cell in reciprocal space and σ is the volume of a unit cell in real space. They are related by $\sigma\sigma_B = (2\pi)^3$. Notice that $N\sigma = L^3$ is the volume of the crystal. Therefore

$$\sum_{\vec{k}}(1) = \left(\frac{L}{2\pi}\right)^3 \int d^3\vec{k} = \frac{V}{(2\pi)^3}\int d^3\vec{k}, \tag{B.8}$$

where L^3 can be replaced by the volume of the single crystal V. Using this result, the expectation value of total energy takes the following form [106, 108]

$$\langle\epsilon\rangle_{total} = 3\hbar\frac{V}{(2\pi)^3}\int \omega_{\vec{k}}(n_B(\beta\hbar\omega_{\vec{k}}) + 1/2))d^3\vec{k}. \tag{B.9}$$

Converting the above equation to spherical polar coordinates, using equation (B.1) and simplifying, we obtain

$$\langle\epsilon\rangle_{total} = \frac{3\hbar V}{2\pi^2\upsilon^3}\int_0^{\omega_d} d\omega\cdot\omega^3\left(\frac{1}{(e^{\hbar\omega/k_BT}-1)} + \frac{1}{2}\right), \tag{B.10}$$

where $\omega_d = (6\pi^2N/V)^{1/3}\upsilon$ is the Debye frequency. The second term in the above integrand does not contribute to the specific heat[4] and hence we obtain [82, 106, 108]

$$\langle\epsilon\rangle_{total} = \frac{3\hbar V}{2\pi^2\upsilon^3}\int_0^{\omega_d} d\omega\frac{\omega^3}{(e^{\hbar\omega/k_BT}-1)}. \tag{B.11}$$

We define $x = \hbar\omega/k_BT$, $x_d = \hbar\omega_d/k_BT$ and the Debye temperature $\theta_D = \hbar\omega_d/k_B$, and thus the above expression becomes

[4]Because it doesn't depend on temperature.

$$\langle \epsilon \rangle_{total} = \frac{9k_B N}{\theta_D^3} T^4 \int_0^{x_d} dx \frac{x^3}{(e^x - 1)}, \tag{B.12}$$

which for low temperatures [82] $\hbar\omega_d \gg k_B T$ becomes

$$\langle \epsilon \rangle_{total} = \frac{9k_B N}{\theta_D^3} T^4 \int_0^{\infty} dx \frac{x^3}{(e^x - 1)} \simeq \frac{9k_B N}{\theta_D^3} T^4 \cdot \frac{\pi^4}{15}. \tag{B.13}$$

Finally, the specific heat of atomic vibrations can be found by taking the derivative of equation (B.13) with respect to temperature [82, 106, 108][5]

$$C_{vib} = \frac{\partial \langle \epsilon \rangle_{total}}{\partial T} = \frac{12k_B \pi^4 N}{5\theta_D^3} T^3, \tag{B.14}$$

and thus

$$\boxed{C_{vib} = \alpha T^3}. \tag{B.15}$$

Equation (B.15) is the atomic contribution to the specific heat. Equation (B.15) is used for fitting the low temperature specific heat data in Figure 5.5.

[5]Notice here that the heat capacity is written without a subscript; this is because for a solid we can assume that $C = C_P = C_V$. Recall that $C_P - C_V = VT\alpha^2/B$, where α is the thermal expansion and B is the isothermal compressibility. In general for solids $\alpha \sim 10^{-6}/K$.

B.2 Sommerfeld Model $C \sim T$

In this appendix we derive the linear temperature dependence of the specific heat due to the electron gas in a metal. Firstly, electrons are fermions and must be treated with Fermi-Dirac statistics. Recall the Fermi-Dirac function equation (4.2)

$$f(\epsilon_k) = \frac{1}{e^{(\epsilon_k - \mu)/k_B T} + 1} \tag{B.16}$$

is the probability that an eigenstate at energy ϵ is occupied. μ is the chemical potential which equals[6] the Fermi energy ϵ_F at $T = 0K$ [106]. Since conduction electrons are free, they have energy

$$\epsilon_k = \frac{\hbar^2 k^2}{2m_e}, \tag{B.17}$$

where k is the wave vector of the conduction electrons. The Fermi energy is given by

$$\epsilon_F = \frac{\hbar^2 k_F^2}{2m_e}, \tag{B.18}$$

where k_F is the Fermi wave vector. Notice that the total number of electrons N can be expressed as the sum of the Fermi-Dirac distribution over all eigenstates

$$N = \sum_{eigenstates} f(\epsilon_k) = 2 \sum_{\vec{k}} f(\epsilon_k), \tag{B.19}$$

[6]The Fermi energy is the highest energy of single particle states that can exist at $T = 0K$.

where the factor of 2 comes from the Pauli Exclusion Principle. Using equation (B.8) the above expression becomes [106]

$$N = \frac{2V}{(2\pi)^3}\int d^3\vec{k} f(\epsilon_k) = \frac{2V\cdot 4\pi}{(2\pi)^3}\int_0^\infty k^2 dk f(\epsilon_k), \tag{B.20}$$

where we converted the integral into polar coordinates and evaluated the azimuthal and polar angles. For low T (i.e. $T \to 0$, which implies $\mu \simeq \epsilon_F$) the Fermi-Dirac distribution function becomes

$$f(\epsilon_k) \simeq \frac{1}{e^{(\epsilon_k-\epsilon_F)/k_BT}+1} = \begin{cases} 1 & ;\ \epsilon_k \leq \epsilon_F \\ 0 & ;\ \epsilon_k \geq \epsilon_F, \end{cases}$$

In particular, if we integrate the integrand in equation (B.20) to some value of energy $k < k_F$ then we obtain the number of electrons up to some energy $\epsilon_k < \epsilon_F$ [82] (from this point in the calculation, we drop the subscript 'k' such that $\epsilon_k = \epsilon$). Therefore

$$N(\epsilon) = \frac{V}{\pi^2}\int_0^k k^2 dk(1) = \frac{V}{3\pi^2}k^3 = \frac{V}{3\pi^2}\left(\frac{2m_e\epsilon}{\hbar^2}\right)^{3/2}, \tag{B.21}$$

which is expressed in terms of ϵ by use of equation (B.17). The density of states in 3D $g(\epsilon)$ at energy ϵ, is by definition the number of states per energy interval, and can be expressed mathematically as [82]

$$g(\epsilon) = \frac{dN}{d\epsilon} = \frac{V}{3\pi^2}\left(\frac{2m_e}{\hbar^2}\right)^{3/2}\frac{d(\epsilon^{3/2})}{d\epsilon}, \tag{B.22}$$

thus

$$g(\epsilon) = \frac{V}{2\pi^2}\left(\frac{2m_e}{\hbar^2}\right)^{3/2}\epsilon^{1/2}. \tag{B.23}$$

The increase in total energy ΔU of a system of N electrons when the temperature changes from 0K to some small temperature T (where $k_B T \ll \epsilon_F$) is [82]

$$\Delta U = \int_{\epsilon_F}^{\infty} d\epsilon(\epsilon - \epsilon_F) f(\epsilon) g(\epsilon) + \int_0^{\epsilon_F} d\epsilon(\epsilon_F - \epsilon)(1 - f(\epsilon)) g(\epsilon). \tag{B.24}$$

The left-hand term in equation (B.24) gives the energy required to excite electrons from the Fermi energy to orbitals above the Fermi energy, where the product $f(\epsilon)g(\epsilon)d\epsilon$ in the number of electrons elevated to energy $\epsilon > \epsilon_F$ in the energy range $d\epsilon$. The right-hand term in equation (B.24) gives the energy required to liberate electrons to the Fermi energy from energy levels $\epsilon < \epsilon_F$, where the term $(1 - f(\epsilon))$ is the probability an electron has been removed from a state of energy $\epsilon < \epsilon_F$.

The heat capacity due to the electrons can be found by differentiating equation (B.24) with respect to T and simplifying to obtain

$$C_{el} = \frac{dU}{dT} = \int_0^{\infty} d\epsilon(\epsilon - \epsilon_F)\frac{df}{dT} g(\epsilon). \tag{B.25}$$

The function $(\epsilon - \epsilon_F)df/dT$ consists of two positive peaks about ϵ_F which converge to ϵ_F for $k_B T \ll \epsilon_F$. Hence, this function acts as a delta function and picks out the energy $\epsilon = \epsilon_F$, causing equation (B.25) to take the following

form [82]

$$C_{el} \simeq g(\epsilon_F) \int_0^\infty d\epsilon(\epsilon - \epsilon_F) \frac{df}{dT}. \tag{B.26}$$

Making the following substitution $x = (\epsilon - \epsilon_F)/k_B T$, we obtain [82]

$$C_{el} = k_B^2 T g(\epsilon_F) \int_{-\epsilon_F \beta}^\infty \frac{e^x}{(1+e^x)^2} x^2 dx, \tag{B.27}$$

where $\epsilon_F \beta \to -\infty$ (here $\beta = (k_B T)^{-1}$) for the case where $k_B T \ll \epsilon_F$. Hence, the integrand can be evaluated analytically and the electronic specific heat becomes

$$\boxed{C_{el} = k_B^2 T g(\epsilon_F) \left(\frac{\pi^2}{3}\right) = \gamma T}. \tag{B.28}$$

Equation (B.28) is the electronic contribution to the specific heat. Equation (B.28) is used for fitting the low temperature specific heat data in Figure 5.5.

Appendix C

Powder X-ray diffraction (PXRD)

In this appendix the basic types of optics used for PXRD measurements is discussed (Figure C.2). The diffraction peaks for LiPB single crystals are tabulated from several different sources (Figures C.3, C.4, Tables C.1, C.2 and Tables C.3- C.12).

C.1 Basic Idea and Optics Used

The two types of optics used for the PXRD measurements are Bragg-Brentano (BB) and Parallel Beam (PB). In principle, PXRD can be thought of as many randomly oriented grains which can be summed over such that incident x-rays will reflect off of an average surface and constructively interfere at certain angles 2θ described by Bragg's law

$$2d \sin\theta = n\lambda, \tag{C.1}$$

where n is a positive integer (n=1 for first order diffraction). The parameters are described in Figure C.1.

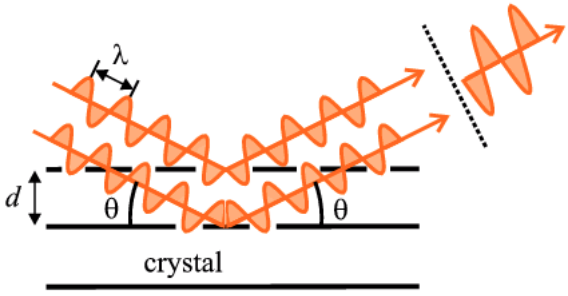

Figure C.1: Reflection of x-rays from a single crystal at one of its characteristic peaks. The RIGAKU unit used for all PXRD measurements has a copper anode, which yields $\lambda = 1.54\mathring{A}$. Image reproduced from [110].

In all powder measurements, both the Bragg-Brentano (BB) optical configuration and the Parallel Beam (PB) optical configuration as described in Figure C.2 were used.

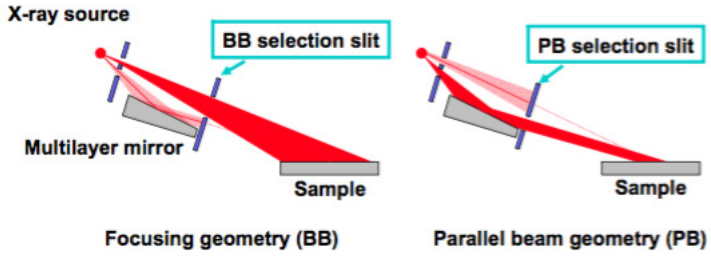

Figure C.2: Optics used for BB and PB measurement. Image reproduced from [112].

The primary difference between these configurations is the insertion of a reflective surface in the PB configuration which is ideal for amorphously shaped powder samples [111]. The BB method is better for lower intensity detection [112]. Without performing a proper optical/sample alignment the

configuration of BB will introduce a 2θ peak shift [112]. Furthermore, an uneven powder surface will introduce a broadening of diffraction peaks [112].

C.2 Diffraction data for single crystal LiPB I.33 batch

In this section XRD powder data from batch I.33 is presented. The program MATCH! [78] was used to characterize the LiPB single crystals (i.e. I.28, I.30, I.31, I.33, I.34 yielded single crystals of LiPB). I.33 fits closest to the accepted powder pattern from [21]. In Figure C.3, the I.33 powder pattern is compared directly to [21].

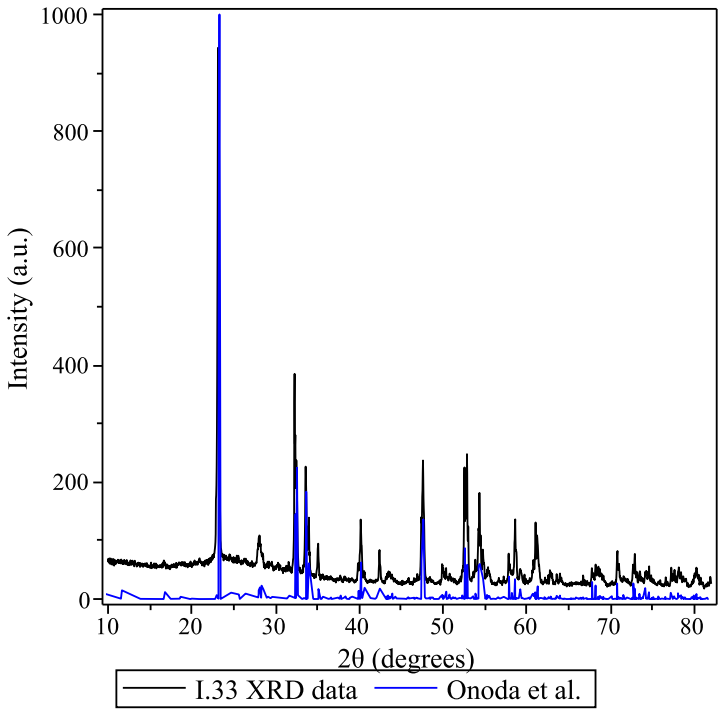

Figure C.3: **a)**: Comarison of raw XRD data from Bragg-Brentano precise scan of LiPB single crystals from batch I.33 (black) (n=0.33) and data taken from [21] (blue). The data from [21] was taken directly from Tables C.1 to C.12.

In Figure C.4, the I.33 powder pattern is compared to that found by a previous

Brock M.Sc. student [113].

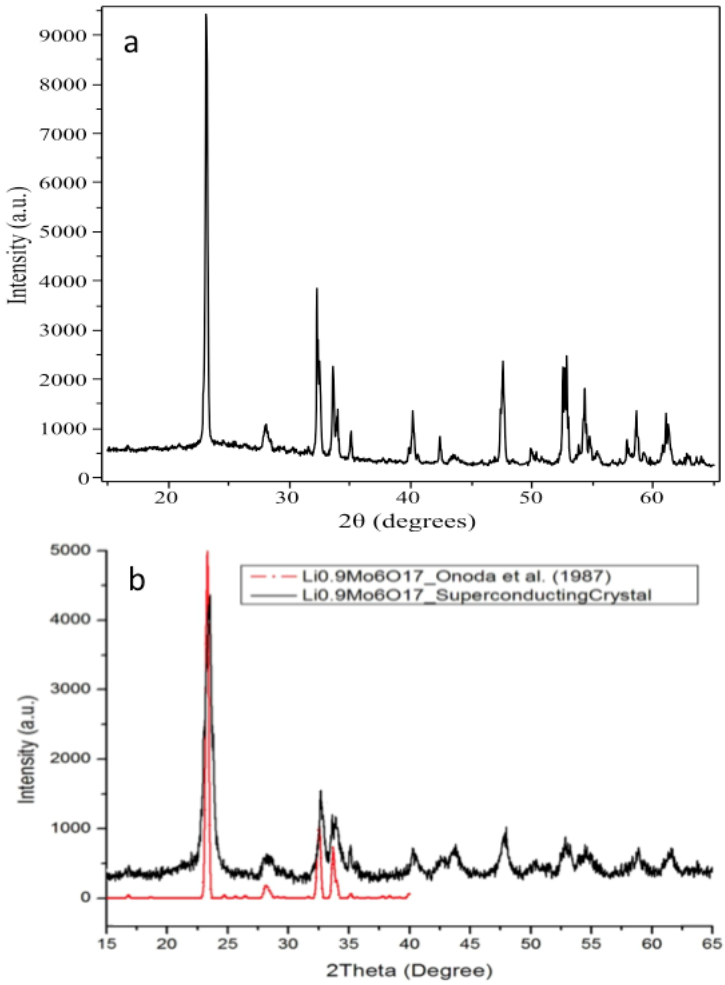

Figure C.4: **a)**: Raw XRD data from Bragg-Brentano precise scan of LiPB single crystals from batch I.33 (n=0.33). **b)**: XRD powder diffraction data, the black data was collected by a previous Brock M.Sc. student [113] and the red data was taken from [21].

Tables C.1 and C.2 give the diffraction peaks for I.33. Tables C.3 to C.12 give the complete list of diffraction peaks from [21] (The peaks can be converted directly to 2θ by solving equation (C.1) and using $\lambda = 1.54\mathring{A}$ with $n = 1$.).

Table C.1: Diffraction peaks of lithium purple bronze n=0.33

2θ	My XRD intensity (arbitrary units)	COD XRD (arbitrary units)
6.92	/	10
9.3	/	5.7
11.66	/	8.1
16.81	/	6.5
23.27	1000	1244.7
24.7	/	6
25.63	/	4.2
26.43	/	5.1
28.07	277.3	63.8
28.41	/	6.3
28.61	/	4.7
28.54	/	9.5
31.66	/	3.1
32.33	499	80.6
32.51	608.9	231.4
33.64	468.7	152.3
33.98	295.7	51.1
35.15	115.4	14
37.79	/	3.3
39.93	63.3	14.7
40.25	331.6	74.8
40.64	28.2	16.6
42.48	143.2	14.6
43.47	137.9	16.2
43.96	/	5.2
47.45	237	36.2
47.67	656.9	132.8
49.98	135.5	15.2
50.4	/	6.9
50.54	/	3.4
50.78	/	4.2
52.3	/	3.4
52.62	442	59.8
52.8	385.2	60.7
52.93	309.6	66.4
53.92	83.6	9.5
54.28	161.8	31.2
54.4	324.3	65
54.8	201.3	29.1
55.44	183.7	22.3
57.9	135.1	32.5
58.29	44.7	8.6
58.68	350	57.1
59.24	78.7	16.9
60.84	117.3	20.6
61.11	195.5	26.2
61.37	223.9	25.2
62.88	60.7	8.1
63.62	22.7	6.4
64	38.6	6.4
66.79	27.2	3
67.84	90.9	24.1
68.3	114.2	19.1

Table C.2: Diffraction peaks of lithium purple bronze n=0.33

2θ	My XRD intensity (arbitrary units)	COD XRD (arbitrary units)
68.61	155.5	14.6
70.88	169	26.1
71.55	/	3.8
72.74	114	16.5
72.96	61.3	23.3
73.57	55.2	10.2
74.32	82.8	20.5
74.67	46.6	10.2
77.32	74.2	9.8
77.71	44.5	4.6
78.24	109.1	19.9
78.76	55.8	12
79.97	/	3.3
80.31	177.4	17.4

C.3 Literature diffraction data

Tables C.3- C.12 is LiPB diffraction data taken from reference [21].

Table C.3: Diffraction peaks of LiPB

d [Å]	Intensity (arbitrary units)	h	k	l	Multiplicity (how often the peak occurs due to symmetry)
12.7613	18.3	1	0	0	2
9.4985	10.5	0	0	1	2
7.6586	0.6	1	0	-1	2
7.5809	14.9	1	0	1	2
6.3806	0.3	2	0	0	2
5.3228	0.0	2	0	-1	2
5.2706	11.9	2	0	1	2
5.0687	0.3	1	1	0	4
4.7745	0.6	0	1	1	4
4.7492	3.9	0	0	2	2
4.4797	0.0	1	1	-1	4
4.4666	0.1	-1	0	2	2
4.4640	0.0	1	1	1	4
4.4356	0.7	1	0	2	2
4.2538	0.0	3	0	0	2
4.1759	0.0	2	1	0	4
3.8977	0.1	3	0	-1	2
3.8669	6.7	3	0	1	2
3.8326	0.6	2	1	-1	4
3.8293	502.4	2	0	-2	2
3.8130	1000.0	2	1	1	4
3.7905	0.1	2	0	2	2
3.6010	10.9	0	1	2	4
3.4730	7.8	-1	1	2	4
3.4584	0.1	1	1	2	4
3.3701	9.3	3	1	0	4
3.1903	2.7	4	0	0	2
3.1855	8.2	3	0	-2	2
3.1846	14.9	3	1	-1	4
3.1677	19.9	3	1	1	4
3.1662	14.7	0	0	3	2
3.1520	2.2	3	0	2	2
3.1469	22.9	2	1	-2	4
3.1252	17.3	2	1	2	4
3.0807	2.2	-1	0	3	2
3.0654	4.0	1	0	3	2
3.0341	1.4	4	0	-1	2
3.0146	3.7	4	0	1	2
2.8483	0.9	-2	0	3	2
2.8242	5.8	2	0	3	2
2.7625	1.6	4	1	0	4
2.7615	145.1	0	2	0	2
2.7594	1.7	3	1	-2	4
2.7468	224.6	0	1	3	4
2.7375	6.5	3	1	2	4
2.6990	0.2	1	2	0	4
2.6904	0.4	-1	1	3	4
2.6802	1.8	1	1	3	4
2.6614	0.0	4	0	-2	2
2.6592	183.6	4	1	-1	4
2.6517	0.3	0	2	1	4
2.6461	1.3	4	1	1	4
2.6353	61.2	4	0	2	2

Table C.4: Diffraction peaks of LiPB

d [Å]	Intensity (arbitrary units)	h	k	l	Multiplicity (how often the peak occurs due to symmetry)
2.5978	1.3	-1	2	1	4
2.5947	0.0	1	2	1	4
2.5529	0.1	3	0	-3	2
2.5523	17.1	5	0	0	2
2.5343	0.2	2	2	0	4
2.5315	0.2	-2	1	3	4
2.5270	0.0	3	0	3	2
2.5145	4.0	2	1	3	4
2.4714	0.3	5	0	-1	2
2.4583	0.7	5	0	1	2
2.4512	2.7	2	2	-1	4
2.4461	0.0	2	2	1	4
2.3976	2.5	4	1	-2	4
2.3873	0.4	0	2	2	4
2.3784	6.0	4	1	2	4
2.3746	0.0	0	0	4	2
2.3488	3.1	-1	2	2	4
2.3443	4.6	1	2	2	4
2.3390	0.9	-1	0	4	2
2.3301	0.2	1	0	4	2
2.3173	0.0	3	1	-3	4
2.3168	0.8	5	1	0	4
2.3162	1.9	3	2	0	4
2.2979	4.1	3	1	3	4
2.2594	0.1	4	0	-3	2
2.2582	2.9	5	0	-2	2
2.2559	14.1	5	1	-1	4
2.2533	1.6	3	2	-1	4
2.2473	0.1	3	2	1	4
2.2459	0.9	5	1	1	4
2.2398	62.7	2	2	-2	4
2.2383	13.3	5	0	2	2
2.2354	12.2	4	0	3	2
2.2333	1.6	-2	0	4	2
2.2320	2.4	2	2	2	4
2.2178	19.3	2	0	4	2
2.1815	1.6	0	1	4	4
2.1538	0.4	-1	1	4	4
2.1468	2.1	1	1	4	4
2.1269	17.8	6	0	0	2
2.0912	0.0	4	1	-3	4
2.0903	4.4	5	1	-2	4
2.0880	0.4	4	2	0	4
2.0866	2.0	3	2	-2	4
2.0829	0.4	-3	0	4	2
2.0811	6.1	0	2	3	4
2.0802	0.4	6	0	-1	2
2.0771	1.1	3	2	2	4
2.0744	3.9	5	1	2	4
2.0721	0.7	4	1	3	4
2.0708	3.4	6	0	1	2
2.0704	1.9	-2	1	4	4
2.0641	2.8	3	0	4	2

Table C.5: Diffraction peaks of LiPB

d [Å]	Intensity (arbitrary units)	h	k	l	Multiplicity (how often the peak occurs due to symmetry)
2.0581	9.4	2	1	4	4
2.0563	0.5	-1	2	3	4
2.0517	0.8	1	2	3	4
2.0422	4.1	4	2	-1	4
2.0363	1.0	4	2	1	4
1.9975	0.6	5	0	-3	2
1.9848	0.1	6	1	0	4
1.9826	1.6	-2	2	3	4
1.9768	3.1	5	0	3	2
1.9745	0.9	2	2	3	4
1.9489	2.3	-3	1	4	4
1.9489	0.5	6	0	-2	2
1.9467	0.1	6	1	-1	4
1.9390	2.4	6	1	1	4
1.9335	1.7	3	1	4	4
1.9335	1.2	6	0	2	2
1.9163	0.1	4	2	-2	4
1.9147	65.9	4	0	-4	2
1.9065	136.4	4	2	2	4
1.8997	3.3	0	0	5	2
1.8952	1.0	4	0	4	2
1.8819	1.2	-1	0	5	2
1.8784	2.7	5	1	-3	4
1.8761	0.0	1	0	5	2
1.8746	1.9	3	2	-3	4
1.8743	2.6	5	2	0	4
1.8643	2.6	3	2	3	4
1.8612	0.1	5	1	3	4
1.8416	0.1	5	2	-1	4
1.8378	0.7	6	1	-2	4
1.8361	2.5	5	2	1	4
1.8260	6.8	-2	0	5	2
1.8249	2.5	6	1	2	4
1.8230	6.3	7	0	0	2
1.8221	0.0	1	3	0	4
1.8154	3.3	2	0	5	2
1.8090	12.6	4	1	-4	4
1.8074	0.0	0	3	1	4
1.8005	1.3	0	2	4	4
1.7964	7.7	0	1	5	4
1.7939	1.7	7	0	-1	2
1.7926	1.6	4	1	4	4
1.7900	0.0	-1	3	1	4
1.7890	0.1	1	3	1	4
1.7868	0.9	7	0	1	2
1.7848	2.7	-1	2	4	4
1.7813	2.9	-1	1	5	4
1.7808	1.6	1	2	4	4
1.7764	1.3	1	1	5	4
1.7743	2.6	6	0	-3	2
1.7688	0.1	2	3	0	4
1.7569	1.9	6	0	3	2
1.7487	1.3	4	2	-3	4

Table C.6: Diffraction peaks of LiPB

d [Å]	Intensity (arbitrary units)	h	k	l	Multiplicity (how often the peak occurs due to symmetry)
1.7481	0.8	5	2	-2	4
1.7478	6.2	5	0	-4	2
1.7415	0.5	-3	0	5	2
1.7399	0.1	2	3	-1	4
1.7388	10.2	5	2	2	4
1.7380	87.1	2	3	1	4
1.7375	8.6	4	2	3	4
1.7365	0.8	-2	2	4	4
1.7337	56.1	-2	1	5	4
1.7312	1.6	7	1	0	4
1.7294	0.9	5	0	4	2
1.7292	58.7	2	2	4	4
1.7277	2.2	3	0	5	2
1.7247	1.6	2	1	5	4
1.7165	1.0	0	3	2	4
1.7081	4.8	7	0	-2	2
1.7062	0.3	7	1	-1	4
1.7021	1.0	-1	3	2	4
1.7004	0.0	1	3	2	4
1.7001	9.3	7	1	1	4
1.6959	0.2	7	0	2	2
1.6896	0.9	3	3	0	4
1.6893	56.7	6	1	-3	4
1.6850	60.0	6	2	0	4
1.6742	35.4	6	1	3	4
1.6664	0.5	5	1	-4	4
1.6647	2.1	3	3	-1	4
1.6629	1.0	-3	2	4	4
1.6622	2.8	3	3	1	4
1.6615	0.2	6	2	-1	4
1.6609	7.1	-3	1	5	4
1.6592	2.7	2	3	-2	4
1.6567	5.2	6	2	1	4
1.6560	2.6	2	3	2	4
1.6533	5.3	3	2	4	4
1.6503	1.5	5	1	4	4
1.6489	0.1	3	1	5	4
1.6399	0.6	-4	0	5	2
1.6318	0.1	7	1	-2	4
1.6247	3.1	4	0	5	2
1.6212	1.3	7	1	2	4
1.6185	0.9	5	2	-3	4
1.6074	3.8	5	2	3	4
1.5952	0.0	8	0	0	2
1.5946	0.3	4	3	0	4
1.5940	0.1	3	3	-2	4
1.5928	0.3	6	0	-4	2
1.5923	0.6	6	2	-2	4
1.5915	38.3	0	3	3	4
1.5897	1.7	3	3	2	4
1.5872	0.1	7	0	-3	2
1.5838	0.9	6	2	2	4
1.5831	10.5	0	0	6	2

Table C.7: Diffraction peaks of LiPB

d [Å]	Intensity (arbitrary units)	h	k	l	Multiplicity (how often the peak occurs due to symmetry)
1.5803	0.0	-1	3	3	4
1.5782	0.4	1	3	3	4
1.5760	0.1	6	0	4	2
1.5759	0.8	8	0	-1	2
1.5739	34.0	4	3	-1	4
1.5735	32.7	4	2	-4	4
1.5731	1.3	-1	0	6	2
1.5726	0.8	7	0	3	2
1.5721	1.1	-4	1	5	4
1.5712	0.3	4	3	1	4
1.5704	0.1	8	0	1	2
1.5690	1.7	1	0	6	2
1.5651	1.1	0	2	5	4
1.5626	1.6	4	2	4	4
1.5586	16.7	4	1	5	4
1.5551	1.6	-1	2	5	4
1.5518	1.4	1	2	5	4
1.5461	0.1	-2	3	3	4
1.5423	0.8	2	3	3	4
1.5403	0.7	-2	0	6	2
1.5327	2.7	2	0	6	2
1.5325	0.0	8	1	0	4
1.5317	0.3	5	0	-5	2
1.5304	1.3	6	1	-4	4
1.5254	7.6	7	1	-3	4
1.5232	9.2	-2	2	5	4
1.5218	7.6	0	1	6	4
1.5214	4.9	7	2	0	4
1.5170	11.5	8	0	-2	2
1.5170	2.2	2	2	5	4
1.5162	0.2	5	0	5	2
1.5155	9.5	6	1	4	4
1.5154	1.1	8	1	-1	4
1.5141	0.2	4	3	-2	4
1.5129	0.7	-1	1	6	4
1.5125	10.5	7	1	3	4
1.5105	21.8	8	1	1	4
1.5093	0.9	1	1	6	4
1.5092	1.4	4	3	2	4
1.5073	0.2	8	0	2	2
1.5044	1.9	7	2	-1	4
1.5002	1.7	7	2	1	4
1.4932	0.0	3	3	-3	4
1.4931	0.3	5	3	0	4
1.4927	3.2	6	2	-3	4
1.4889	0.0	-3	0	6	2
1.4880	0.6	3	3	3	4
1.4837	0.7	-2	1	6	4
1.4823	3.3	6	2	3	4
1.4785	0.9	3	0	6	2
1.4769	1.6	2	1	6	4
1.4769	4.3	5	2	-4	4
1.4764	3.5	5	3	-1	4

Table C.8: Diffraction peaks of LiPB

d [Å]	Intensity (arbitrary units)	h	k	l	Multiplicity (how often the peak occurs due to symmetry)
1.4760	0.7	5	1	-5	4
1.4736	0.1	5	3	1	4
1.4730	0.7	-3	2	5	4
1.4657	0.1	5	2	4	4
1.4647	2.4	3	2	5	4
1.4628	0.9	8	1	-2	4
1.4621	5.5	5	1	5	4
1.4550	0.7	0	3	4	4
1.4541	6.0	8	1	2	4
1.4535	1.3	7	0	-4	2
1.4526	1.3	7	2	-2	4
1.4467	0.1	-1	3	4	4
1.4452	0.0	7	2	2	4
1.4445	0.9	1	3	4	4
1.4387	0.0	7	0	4	2
1.4375	0.0	-3	1	6	4
1.4307	0.1	8	0	-3	2
1.4282	1.1	3	1	6	4
1.4272	0.0	4	3	-3	4
1.4269	1.0	5	3	-2	4
1.4244	0.2	6	0	-5	2
1.4241	0.7	-4	0	6	2
1.4218	0.8	5	3	2	4
1.4211	0.2	4	3	3	4
1.4206	0.4	-2	3	4	4
1.4185	0.5	8	0	3	2
1.4179	0.1	9	0	0	2
1.4165	2.7	2	3	4	4
1.4121	1.0	4	0	6	2
1.4100	1.2	-4	2	5	4
1.4094	0.1	6	0	5	2
1.4057	2.3	7	1	-4	4
1.4046	0.0	9	0	-1	2
1.4003	2.9	4	2	5	4
1.4002	0.2	9	0	1	2
1.3922	1.7	7	1	4	4
1.3920	0.0	6	3	0	4
1.3850	0.1	8	1	-3	4
1.3813	0.0	8	2	0	4
1.3807	29.2	0	4	0	2
1.3797	0.3	6	2	-4	4
1.3794	0.6	-3	3	4	4
1.3792	0.0	6	1	-5	4
1.3790	0.7	-4	1	6	4
1.3786	0.1	6	3	-1	4
1.3761	0.1	7	2	-3	4
1.3759	0.5	6	3	1	4
1.3739	1.0	8	1	3	4
1.3739	0.5	3	3	4	4
1.3734	23.2	0	2	6	4
1.3734	1.0	9	1	0	4
1.3727	0.1	1	4	0	4
1.3688	0.1	6	2	4	4

Table C.9: Diffraction peaks of LiPB

d [Å]	Intensity (arbitrary units)	h	k	l	Multiplicity (how often the peak occurs due to symmetry)
1.3687	3.0	8	2	-1	4
1.3681	3.7	4	1	6	4
1.3669	4.2	-1	2	6	4
1.3666	1.8	7	2	3	4
1.3664	0.1	0	4	1	4
1.3656	1.1	6	1	5	4
1.3651	0.8	8	2	1	4
1.3642	5.4	1	2	6	4
1.3626	2.5	9	0	-2	2
1.3612	3.0	9	1	-1	4
1.3588	0.0	-1	4	1	4
1.3584	0.2	1	4	1	4
1.3573	3.9	9	1	1	4
1.3569	0.3	0	0	7	2
1.3547	0.8	9	0	2	2
1.3537	0.8	5	3	-3	4
1.3518	0.0	-5	0	6	2
1.3508	0.4	-1	0	7	2
1.3495	0.0	2	4	0	4
1.3478	0.2	1	0	7	2
1.3472	0.0	5	3	3	4
1.3452	1.3	-2	2	6	4
1.3401	4.9	2	2	6	4
1.3395	1.1	5	2	-5	4
1.3389	0.3	5	0	6	2
1.3383	0.1	6	3	-2	4
1.3365	0.0	2	4	-1	4
1.3357	0.3	2	4	1	4
1.3333	0.6	6	3	2	4
1.3307	0.0	8	0	-4	2
1.3301	0.2	-2	0	7	2
1.3296	26.7	8	2	-2	4
1.3290	0.2	5	2	5	4
1.3271	3.7	4	3	-4	4
1.3259	0.1	0	4	2	4
1.3244	2.2	2	0	7	2
1.3231	0.6	8	2	2	4
1.3230	0.5	9	1	-2	4
1.3224	0.8	7	0	-5	2
1.3220	2.0	0	3	5	4
1.3205	0.6	4	3	4	4
1.3192	0.0	-1	4	2	4
1.3184	0.0	1	4	2	4
1.3177	1.9	0	1	7	4
1.3177	7.0	8	0	4	2
1.3160	0.7	-1	3	5	4
1.3157	1.1	9	1	2	4
1.3140	0.3	1	3	5	4
1.3133	0.0	3	4	0	4
1.3130	0.8	-5	1	6	4
1.3122	1.8	-1	1	7	4
1.3105	2.7	-3	2	6	4
1.3094	2.1	1	1	7	4

Table C.10: Diffraction peaks of LiPB

d [Å]	Intensity (arbitrary units)	h	k	l	Multiplicity (how often the peak occurs due to symmetry)
1.3084	1.8	7	0	5	2
1.3035	0.0	3	2	6	4
1.3015	0.0	3	4	-1	4
1.3012	2.3	5	1	6	4
1.3003	0.3	3	4	1	4
1.2992	0.7	9	0	-3	2
1.2989	26.7	-2	4	2	4
1.2974	0.0	2	4	2	4
1.2967	0.0	-3	0	7	2
1.2965	17.8	-2	3	5	4
1.2954	0.4	7	3	0	4
1.2937	0.2	8	1	-4	4
1.2932	2.5	-2	1	7	4
1.2926	0.6	2	3	5	4
1.2890	0.8	9	0	3	2
1.2888	0.2	3	0	7	2
1.2879	8.9	2	1	7	4
1.2862	0.1	7	2	-4	4
1.2860	1.4	7	1	-5	4
1.2848	0.1	7	3	-1	4
1.2822	2.7	7	3	1	4
1.2817	1.0	8	1	4	4
1.2775	18.7	6	3	-3	4
1.2764	4.6	6	0	-6	2
1.2761	0.8	10	0	0	2
1.2759	1.2	7	2	4	4
1.2732	0.3	7	1	5	4
1.2710	11.6	6	3	3	4
1.2703	0.0	8	2	-3	4
1.2676	0.1	5	3	-4	4
1.2672	0.2	4	4	0	4
1.2669	0.7	3	4	-2	4
1.2665	0.1	10	0	-1	2
1.2659	1.3	6	2	-5	4
1.2657	0.5	-4	2	6	4
1.2656	1.4	0	4	3	4
1.2651	2.2	-3	3	5	4
1.2647	0.2	3	4	2	4
1.2635	3.4	6	0	6	2
1.2630	0.0	10	0	1	2
1.2624	0.1	-3	1	7	4
1.2618	0.6	8	2	3	4
1.2614	0.2	9	2	0	4
1.2605	0.5	5	3	4	4
1.2600	0.2	-1	4	3	4
1.2598	0.1	3	3	5	4
1.2589	0.4	1	4	3	4
1.2573	0.4	4	2	6	4
1.2567	0.2	4	4	-1	4
1.2553	0.1	6	2	5	4
1.2553	0.3	4	4	1	4
1.2552	0.0	9	1	3	4
1.2551	4.4	3	1	7	4

Table C.11: Diffraction peaks of LiPB

d [Å]	Intensity (arbitrary units)	h	k	l	Multiplicity (how often the peak occurs due to symmetry)
1.2535	1.1	-4	0	7	2
1.2521	0.0	7	3	-2	4
1.2519	0.0	9	2	-1	4
1.2488	0.9	9	2	1	4
1.2473	0.5	7	3	2	4
1.2439	0.2	4	0	7	2
1.2437	3.1	6	1	-6	4
1.2434	3.7	10	1	0	4
1.2425	0.2	-2	4	3	4
1.2404	0.6	2	4	3	4
1.2357	0.0	10	0	-2	2
1.2345	10.7	10	1	-1	4
1.2317	1.8	6	1	6	4
1.2312	0.1	10	1	1	4
1.2291	4.7	10	0	2	2
1.2281	1.5	8	0	-5	2
1.2256	0.0	4	4	-2	4
1.2245	0.3	-4	3	5	4
1.2231	1.7	9	0	-4	2
1.2230	9.9	4	4	2	4
1.2224	6.0	-4	1	7	4
1.2220	3.0	9	2	-2	4
1.2181	6.5	4	3	5	4
1.2178	0.3	0	2	7	4
1.2162	3.6	9	2	2	4
1.2153	2.2	8	0	5	2
1.2145	0.1	3	4	-3	4
1.2144	1.9	5	4	0	4
1.2141	0.8	-5	2	6	4
1.2135	2.8	4	1	7	4
1.2134	1.3	-1	2	7	4
1.2117	2.7	9	0	4	2
1.2117	0.0	3	4	3	4
1.2112	0.2	1	2	7	4
1.2059	0.0	10	1	-2	4
1.2056	0.0	8	3	0	4
1.2054	0.0	5	4	-1	4
1.2048	0.1	5	2	6	4
1.2045	0.4	6	3	-4	4
1.2039	0.1	5	4	1	4
1.2034	0.0	-5	0	7	2
1.2021	3.2	7	3	-3	4
1.2017	2.7	7	0	-6	2
1.2003	3.0	0	3	6	4
1.1998	0.4	10	1	2	4
1.1988	6.1	8	1	-5	4
1.1984	0.0	-2	2	7	4
1.1972	3.6	6	3	4	4
1.1972	0.5	8	3	-1	4
1.1960	0.3	-1	3	6	4
1.1958	4.1	7	3	3	4
1.1948	8.6	8	3	1	4
1.1942	0.8	9	1	-4	4

Table C.12: Diffraction peaks of LiPB

d [Å]	Intensity (arbitrary units)	h	k	l	Multiplicity (how often the peak occurs due to symmetry)
1.1942	0.4	1	3	6	4
1.1941	1.7	2	2	7	4
1.1936	0.0	0	4	4	4
1.1929	1.4	5	0	7	2
1.1927	0.8	7	2	-5	4
1.1892	3.2	8	2	4	4
1.1891	2.5	7	0	6	2
1.1890	0.0	-1	4	4	4
1.1880	0.0	10	0	-3	2
1.1879	0.0	1	4	4	4
1.1873	1.0	0	0	8	2
1.1869	0.0	8	1	5	4
1.1836	0.3	9	1	4	4
1.1834	0.1	-1	0	8	2
1.1824	0.6	7	2	5	4
1.1814	0.4	-2	3	6	4
1.1810	1.0	1	0	8	2
1.1793	2.3	10	0	3	2
1.1782	0.0	4	4	-3	4
1.1780	0.3	5	4	-2	4
1.1779	0.8	2	3	6	4

Appendix D

Energy gap code

In this appendix the energy gap code (Figures D.1, D.2 and D.3) used to plot $E_g(T)$ in Figure 4.6 is attached. The code was written using Maple 14 [114].

```
> restart
> C := ExcelTools:-
      Import("/Users/call_me_dare/Desktop/Masters_Research/Data/PPMS
      resistivity/LMO_1_sample_18_thin/LMO_I.30_x2_004_ln_resistance_1OT_warm.xlsx");
```

$$C := \begin{bmatrix} 1..55 \text{ x } 1..2 \text{ Array} \\ \text{Data Type: anything} \\ \text{Storage: rectangular} \\ \text{Order: Fortran\_order} \end{bmatrix} \quad (1)$$

```
> for i from 1 by 3 to 49 do
  E_i := Array([[C(i), C(i + 55)], [C(i + 1), C(i + 56)], [C(i + 2), C(i + 57)], [C(i
      + 3), C(i + 58)], [C(i + 4), C(i + 59)]], order = Fortran_order)
  end do:

> with(CurveFitting):
> for i from 1 by 3 to 49 do
  f_i := LeastSquares(E_i, x)
  end do:
> for i from 1 by 3 to 49 do
  F_i := plot(f_i, x = E_i(1)..E_i(5), colour = black)
  end do:
> with(plots):
> p1 := pointplot(C, style = point, colour = brown, legend = "warm up data for fit");
```

$$p1 := PLOT(\ldots) \quad (2)$$

```
> display([p1, F_1, F_7, F_13, F_19, F_25, F_31, F_37, F_43, F_49], axes = boxed, labels
      = ["1/T (1/Kelvin)", "ln(R_b) (ln(Ohm))"], labeldirections = ["horizontal", "vertical"],
      labelfont = ["ROMAN", 12], title
      = `Inverse temperature dependance vs. natural logarithm of resistivity for single crystal
      from batch I.30 with 1 mA excitation current`, titlefont = ["ROMAN", 14]);
>
```

Figure D.1: Energy gap code page 1.

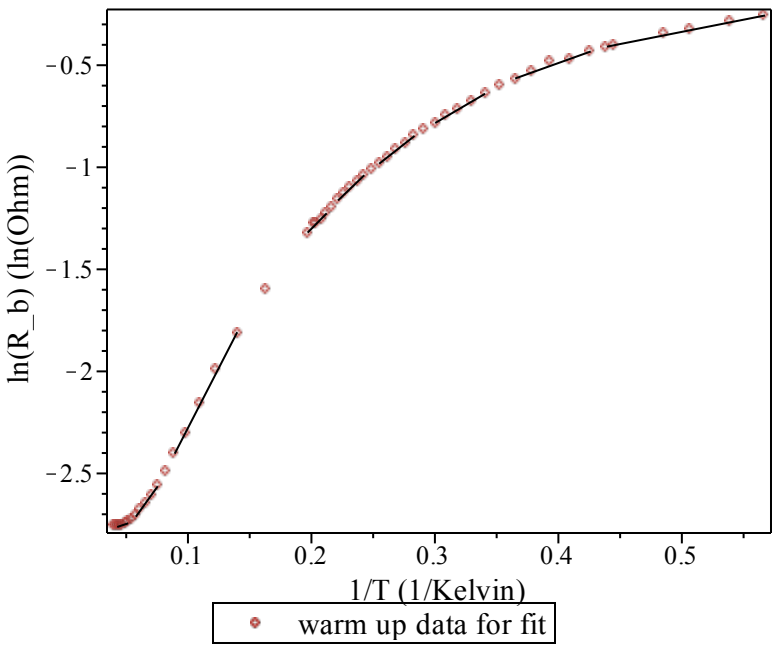


```
> for i from 1 by 3 to 49 do
  G_i := diff(f_i, x)
  end do:
> for i from 1 by 3 to 49 do
  i
  end do:
> for i from 1 by 1 to 17 do
  3·i − 2
  end do:
> B
      := [seq([ 1/5 ( 1/C(3·n − 2) + 1/C(3·n − 1) + 1/C(3·n) + 1/C(3·n + 1)
      + 1/C(3·n + 2) ), 2·8.6173303·10^−5·1000· G_(3·n − 2)], n = 1 ..17) ]:
> p2 := pointplot(B, style = point, colour = blue);
                                  p2 := PLOT(...)                    (1)
>
```

Figure D.2: Energy gap code page 2.

```
> display([p2], axes = boxed, labels = ["Temperature (Kelvin)", "Egap (meV)"], labeldirections
      = ["horizontal", "vertical"], title
      = `T vs. Energy Gap for single crystal from batch I.30 with 1 mA in plane excitation current
     along lowest resistive axis`, titlefont = ["ROMAN", 14], labelfont = ["ROMAN", 12], view
      = [0..22, 0..2.2]);
```

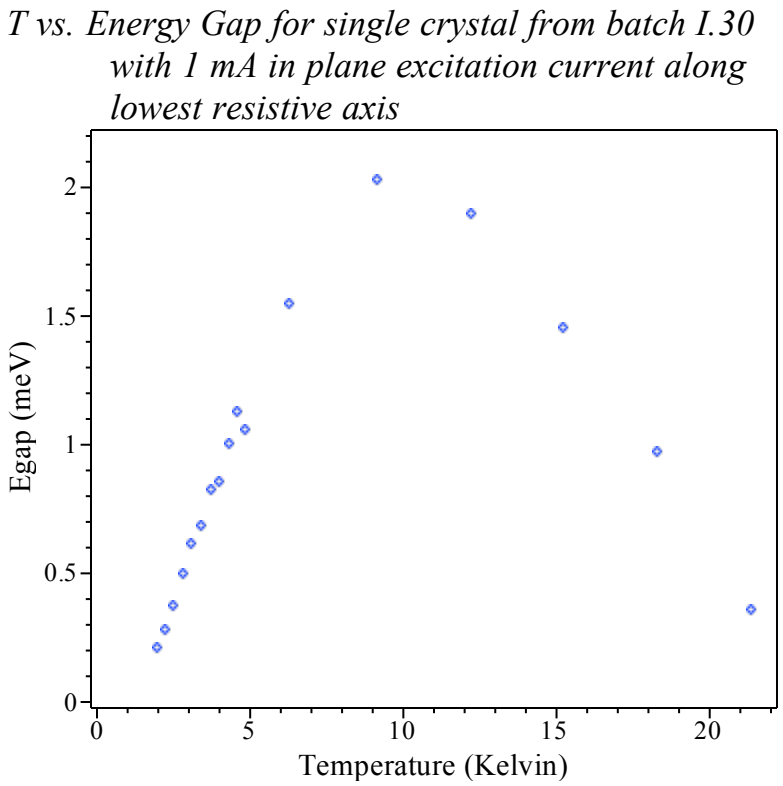


```
> writedata("/Users/call_me_dare/Desktop/Masters_Research/Data/PPMS
      resistivity/LMO_1_sample_18_thin/Egap_data.txt", B);
>
```

boltzmann constant taken from: http://physics.nist.gov/cgi-bin/cuu/Value?tkev

Find error of points quickly, print 5 point to txt file:

```
> Errorpoints := [seq( [C(i), C(i + 55)], i = 4..8) ];
```

$$Errorpoints := [[0.48573162539742964, -0.3474434346229713], [0.4393673066536388, -0.4160385808263775], [0.44488932509538043, -0.41057089750905756], [0.42614848166142383, -0.43871224149251026], [0.4089645074957748, -0.47227845820802805]] \quad (1)$$

```
> writedata("/Users/call_me_dare/Desktop/Masters_Research/Data/PPMS
```

Figure D.3: Energy gap code page 3.

Bibliography

[1] Xu, X., et al., "Directional Field-Induced Metallization of Quasi-One-Dimensional Li0.9Mo6O17", *PRL* **2009**, *102*, 1-4.

[2] Dudy, L., Denlinger, J. D., et. al., "Photoemission Spectroscopy and the Unusually Robust One Dimensional Physics of Lithium Purple Bronze", *arXiv* **2013**, 1-20.

[3] Greenblatt, M., "Molybdenum Oxide Bronzes with Quasi-Low-Dimensional Properties", *Chem. Rev.* **1988**, *88*, 31-53.

[4] Alves, L., de Lima, B., et al., "Phase transitions in K-doped MoO2", *Journal of Applied Physics* **2014**, *115*, pg. 204912-1 to 204912-4.

[5] Alves, L., dos Santos, C., et al., "Superconductivity and magnetism in the KxMoO2-δ", *Journal of Applied Physics* **2012**, *112*, pg. 073923-1 to 073923-5.

[6] Alves, L. M. S., Damasceno, V. I., et al., "Unconventional metallic behavior and superconductivity in the K-Mo-O system", *PHYSICAL REVIEW B* **2010**, *81*, pg. 174532-1 to 174532-5.

[7] Alves, L. M. S., de Lima, B. S., et al., "Superconductivity and Physical Properties in the KxMoO2-δ", *InTech* **2015**, pg. 3-15.

[8] Xiaofeng, X., Bangura, A. F., Greenblatt, M., et. al., "On the transport and thermodynamic properties of quasi-two-dimensional purple bronzes A0.9Mo6O17 (A=Na, K)", *arXiv* **2012**, pg. 1-8.

[9] McCarroll, W. H., Greenblatt, M., "Preparation of Lithium Molybdenum Oxide Bronzes by a Temperature Gradient Flux Growth Technique", *Journal of SS Chem.* **1984**, *54*, 282-290.

[10] Strobel, P., Greenblatt, M., "Crystal Growth and Electrical Properties of Lithium, Rubidium, and Cesium Molybdenum Oxide Bronzes", *Jour. of SSC* **1980**, *36*, 331-338.

[11] Matsuda, Y., Sato, M., et al., "On the anomalous transport properties of Li0.9Mo6O17", *Solid State Phys.* **1986**, *19*, 6039-6052.

[12] Boujida, M., Escribe-Filippini, C., et al., "Superconducting properties of the low dimensional lithium molybdenum purple bronze Li0.9Mo6O17", *Physica C* **1988**, *153-155*, pg. 465-466.

[13] Escribe-Filippini, C., Beille, J., et al., "Pressure effect on the transport properties of superconducting Li0.9Mo6O17 bronze", *Physica C* **1989**, *162-164*, 427-428.

[14] Wakeham, N., Bangura, A., et al., "Gross violation of the Wiedemann-Franz law in a quasi-one-dimensional conductor", *Nature Communications* **2011**, 1-6.

[15] Luz, M., dos Santos, C., et al., "Anisotropic electrical resistivity of quasi-one-dimensional Li0.9Mo6O17 determined by the Montgomery method", *PHYSICAL REVIEW B* **2007**, *76* pg. 233105-1 to 233105-3.

[16] Schlenker, C., Schwenk, H., et al., "Superconducting properties of the low dimensional purple bronze Li0.9Mo6O17", *Physica 135B* **1985**, 511-514.

[17] Mingliang, T., Chen, L., et al., "Thermoelectric power studies in quasi-two-dimensional purple bronzes AMo6O17 (A=Na, K, Tl)", *Physics Letters A* **1997**, *234*, 477-482.

[18] Mercure, J. F., Bangura, A. F., et al., "Upper Critical Magnetic Field far above the Paramagnetic Pair-Breaking Limit of Superconducting One-Dimensional Li0.9Mo6O17 Single Crystals", *Physical Review Letters* **2012**, *108*, 187003-1 to 187003-5.

[19] Lebed, A.G., Sepper, O., "Possible triplet superconductivity in the quasi-one-dimensional conductor Li0.9Mo6O17" *PHYSICAL REVIEW B* **2013**, *87* pg. 100511-1 to 100511-5.

[20] Sepper, O., Lebed, A.G., "Quantum limit and reentrant superconducting phases in the Q1D conductor Li0.9Mo6O17" *Physica B* **2015**, *460* pg. 231-235.

[21] Onoda, M., Toriumi, K., et. al., "Crystal Structure of Lithium Molybdenum Purple Bronze Li0.9Mo6O17", *Journal of Solid State Chemistry* **1987**, *66*, 163-170.

[22] Hahn, T. (Editor), "INTERNATIONAL TABLES FOR CRYSTALLOGRAPHY", *fifth edition* **2005**, *Volume A*.

[23] Mineral Data Publishing, version 1, "Tugarinovite", *Mineral Data Publishing* **2005**, *Version 1 http://www.handbookofmineralogy.org/pdfs/tugarinovite.pdf*

[24] Scanlon, D., Watson, G., et. al. "Theoretical and Experimental Study of the Electronic Structures of MoO3 and MoO2", *J. Phys. Chem.* **2010**, *114* pg. 4636–4645.

[25] Burns, G., Glazer, M., "Space Groups for Solid State Scientists", *third edition* **2013**, *Elsevier Inc.* pg. 112-119.

[26] **Jmol: an open-source Java viewer for chemical structures in 3D**, *http://www.jmol.org/*.

[27] Chateigner, D., Chen, X., et al., "Crystallography Open Database", *The Research Council of Lithuania* **2017**, *http://www.crystallography.net/cod/index.php*.

[28] ed. Schlenker, C., "Low-Dimensional Electronic Properties of Molybdenum Bronzes and Oxides", *Volume 11* **1989**, *Kluwer Academic Publishers*, pg. 1-295.

[29] Conroy, L., Ben-dor, L., et al., "Molybdenum(IV) Oxide and Tungsten(IV) oxide single crystals", *Inorg. Synth.* **1973**, *14*, pg. 105-107.

[30] Rogers, D. B., Shannon, R.D., et. al., "Crystal Chemistry of Metal Dioxides with Rutile-Related Structures" *Inorganic Chemistry* **1969**, *8* pg. 841-849.

[31] Eyert, V., Horny, R., et. al., "Embedded Peierls instability and the electronic structure of MoO2" *J. Phys.: Condens. Matter* **2000**, *12* pg. 4923-4946.

[32] Alves, L., Benaion, S., et al., "Electrical Resistivity in Non-stoichiometric MoO2", *Braz J Phys* **2015**, pg. 1-4.

[33] Li, Z., Schram, T., et al., "Investigation on Molybdenum and Its Conductive Oxides as p-Type Metal Gate Candidates", *Journal of The Electrochemical Society* **2008**, *155*, pg. H481-H484.

[34] Schulmeyer, W., Ortner, H., "Mechanisms of the Hydrogen Reduction of Molybdenum Oxides", *International Plansee Seminar* **2001**, *3*, pg. 129-146.

[35] Kruglova, A. G., et. al., "Tugarinovite, MoO2, a new hypogene molybdenum mineral", *International Geology Review* **1982**, *24*, 617-620.

[36] Magnéli, A., Andersson, G., "Identification of Molybdenum and Tungsten Oxides", *X-Ray Powder Patterns* **1952**, *24*, pg. 1998-2000.

[37] Ben-dor, L., Shimony, Y., "Crystal structure, magnetic susceptibility and electrical conductivity of pure and NiO-doped MoO2 and WO2", *Materials Research Bulletin* **1974**, *9*, 837-844.

[38] Brandt, B., Skapski, A., "A refinement of the Crystal Structure of Molybdenum Dioxide", *ACTA CHEMICA SCANDINAVICA* **1967**, *21*, pg. 661-672.

[39] Samokhin, K., "Phys 5P73: Superconductivity", *Brock University* **2012**, *https://brocku.ca/webcal/2012/graduate/phys.html*.

[40] Solymar, L., Walsh, D., Syms, R. R. A., "Electrical Properties of Materials", *Oxford* **2014**, *9th edition*, pg. 381.

[41] "The Critical Field, Hc", *Module 7: High temperature Superconductors*, *http://nptel.ac.in/courses/113104005/lecture33/33_4.html*.

[42] "Type I and Type II Superconductors", *Electronics World* **2017**, *http://elektroarsenal.net/type-i-and-type-ii-superconductors.html*.

[43] Green, B., "Superconducting Phases in Bulk and Thin Film LA2CuO4", *Article 17* **2008**, *Volume 4* pg. 85-92.

[44] Vishik, I., "What is superconducting volume fraction and how do you measure it?", *Quora* **2014**, *https://www.quora.com/What-is-superconducting-volume-fraction-and-how-do-you-measure-it*.

[45] Chen, X. H., Wu, T., et. al., "Superconductivity at 43 K in SmFeAsO1-xFx", *Nature Publishing Group* **2008**, *453* pg. 761-762.

[46] Blundell, S., "Magnetism in Condensed Matter", **2001**, *Oxford University Press Inc.*, pg. 4-6.

[47] Gokhfeld, D., "Does anybody know how we can calculate volume fraction of superconductivity in inhomogeneous sample from SQUID bulk data?", *ResearchGate* **2013**, *https://www.researchgate.net/post/Does_anybody_know_how_we_can_calculate_volume_fraction_of_superconductivity_in_inhomogeneous_sample_from_SQUID_bulk_data.*

[48] Campbell, A.M., Blunt, F.J., et al., "Quantitative determination of percentage superconductor in a new compound", *Cryogenics* **1991**, *31* pg. 732-737.

[49] Buntar, V., Weber, H.W., "Magnetic properties of fullerene superconductors", *Supercond. Sci. Technol.* **1996**, *9* pg. 599-615.

[50] Chester, G. V., Thellung, A., "The Law of Wiedemann and Franz" *Proc. Phys. Soc.* **1960**, pg. 1005-1013.

[51] Choi, J., Musfeldt, J. L., et al., "Probing localization effects in Li0.9Mo6O17 purple bronze: An optical-properties investigation", *Physical Review B* **2004**, *69*, pg. 085120-1 to 085120-9.

[52] Luttinger, J. M., "An Exactly Soluble Model of a Many-Fermion System" *Jour. of Math. Phys.* **1963**, *4* pg. 1154-1162.

[53] Jarrell, M., "Lecture 1: The Equilibrium Green Function Method", **2011**, *http://www.phys.lsu.edu/ jarrell/Green/lecture1.pdf* pg. 7.

[54] Denlinger, J. D., Gweon, G. H., et al., "Non-Fermi-Liquid Single Particle Line Shape of the Quasi-One-Dimensional Non-CDW Metal Li0.9Mo6O17:

Comparison to the Luttinger Liquid", *Physical Review Letters* **1999**, *82*, 2540-2543.

[55] Gweon, G.-H., Denlinger, J. D., et. al., "Non-Fermi Liquid Angle Resolved Photoemission Line Shapes of Li0.9Mo6O17" *PHYSICAL REVIEW LETTERS* **2000**, *85* pg. 3985.

[56] Wang, F., Mo, S.-K., et. al., "Case for bulk nature of spectroscopic Luttinger liquid signatures observed in angle-resolved photoemission spectra of Li0.9Mo6O17" *PHYSICAL REVIEW B* **2006**, *74* pg. 113107-1 to 113107-4.

[57] Xu, X., Bangura, A. F., "Transport and thermodynamic properties of quasi-two-dimensional purple bronzes A0.9Mo6O17 (A = Na, K)" *PHYSICAL REVIEW B* **2012**, *85* pg. 195101-1 to 195101-7.

[58] Goldman, A. M., "Electrostatic Gating of Ultrathin Films" *Annu. Rev. Mater. Res.* **2014**, *44* pg. 45-63.

[59] Jompol, Y., Ford, C. J. B., et. al., "Probing Spin-Charge Separation in a Tomonaga-Luttinger Liquid" *SCIENCE* **2009**, *325* pg. 597-601.

[60] Popović, Z. S., Satpathy, S., "Density-functional study of the Luttinger liquid behavior of the lithium molybdenum purple bronze Li0.9Mo6O17", *Phys. Rev. B* **2006**, *74*, pg. 045117-1 to 045117-6.

[61] Gweon, G.-H., Mo, S.-K., et. al., "Luttinger liquid angle-resolved photoemission line shapes from samples of Li0.9Mo6O17 grown by the

temperature-gradient-flux technique" *PHYSICAL REVIEW B* **2004**, *70* pg. 153103-1 to 153103-3.

[62] Xue, J., Duda, L.-C., et. al., "Electronic Structure near the Fermi Surface in the Quasi-One-Dimensional Conductor Li0.9Mo6O17" *PHYSICAL REVIEW LETTERS* **1999**, *83* pg. 1235-1238.

[63] Peierl, R.E., "Quantum Theory of Solids", **1955**, *Clarendon, Oxford*, pg. 108.

[64] ed. Levy, F., "Physics and Chemistry of Materials with Layered Structures", *Volume 2* **1976**.

[65] Toombs, G. A., "QUASI-ONE-DIMENSIONAL CONDUCTORS", *North-Holland publishing company* **1977**, *C40*, pg. 183-240.

[66] Fowler, M., "Electrons in One Dimension: the Peierls Transition", *Introduction: Looking for Superconductors and Finding Insulators* **2007**, *http://galileo.phys.virginia.edu/classes/752.mf1i.spring03/PeierlsTrans.pdf.*

[67] ed. Schlenker, C., "Low-Dimensional Electronic Properties of Molybdenum Bronzes and Oxides", *Volume 11* **1989**, *Kluwer Academic Publishers*, pg. 295-405.

[68] Schlenker, C., Dumas, J., et. al., "Charge-density-wave instabilities in the low-dimensional molybdenum bronzes and oxides", *Philosophical Magazine Part B* **1985**, *52* pg. 643-667.

[69] Whangbo, M., Canadell, E., "Band Electronic Structure of the Lithium Molybdenum Purple Bronze Li0.9Mo6O17", *J. Am. Chem. Soc.* **1988**, *110*, pg. 358-363.

[70] User's Guide, "CN4000 Series Temperature Controller", *Omega Engineering Inc.* **2006**, *https://www.omega.com/manuals/manualpdf/M4546.pdf*, pg. 13-32.

[71] "An Introduction to the Physics of Nuclei and Particles", *Brooks Cole CENGAGE Learning* **2004**, *Dalhousie University*, Appendix B: Properties of Nuclides.

[72] Schubert, U., Hüsing, N. "Synthesis of Inorganic Materials", *Third Edition* **2012**, *Wiley-VCH*, pg. 28, 29, 59-61, 117-121, 156-159.

[73] Sekiya, T., "Flux Growth of MoO2 Single Crystals", *Mat. Res. Bull.* **1981**, *16* pg. 841-846.

[74] Solodovnikov, S. F., Bazarov, B. G., et al., "Li2MoO4-MoO3 Phase Diagram and Crystal Structure of Li4Mo5O17", *Russian Journal of Inorganic Chemistry* **1999**, *44*, 954-961.

[75] Yoreo, J., Vekilov, P., "Principles of Crystal Nucleation and Growth", **2003**, *Lawrence Livermore National Laboratory, University of Houston*, pg. 57-93.

[76] Polte, J., "Fundamental growth principles of colloidal metal nanoparticles- a new perspective", *CrystEngComm* **2015**, *17*, 6809-6830.

[77] Lorenzo, A. T., Muller, A. J., "Estimation of the Nucleation and Crystal Growth Contributions to the Overall Crystallization Energy Barrier", *Journal of Polymer Science: Part B: Polymer Physics* **2008**, *46*, 1478-1487.

[78] "MATCH! Phase Identification from Powder Diffraction", **2017**, *http://www.crystalimpact.com/match/*.

[79] Zisman, W. A., "Relation of the Equilibrium Contact Angle to Liquid and Solid Constitution", *U. S. Naval Research Laboratory* **1964**, *American Chemical Society*, pg. 1-51.

[80] Degiorgi, L., Wachter, P., "Optical investigation of quasi-one- and two-dimensional systems A0.9Mo6017 (A= Li, K, and Na)", *Physical Review B* **1988**, *38*, pg. 5821-5826.

[81] "PDXL: Integrated X-ray powder diffraction software", **2017**, *https://www.rigaku.com/en/service/software/pdxl*,

[82] Kittel, C., "Introduction to Solid State Physics", *Eighth Edition* **2005**, *John Wiley and Sons Inc.*, pg. 107-209.

[83] Fitzpatrick, R., "Thermodynamics and Statistical Mechanics: An intermediate level course", *The University of Texas at Austin* pg. 189-195.

[84] Sze, S. M., Ng., K., "Physics of Semiconductor Devices", *Third Edition* **2007**, *John Wiley and Sons Inc.*, pg. 24-26.

[85] Colinge, J.-P., Colinge, C., "Physics of Semiconductor Devices", *KLUWER ACADEMIC PUBLISHERS*, pg. 25-30.

[86] Schroder, D., "SEMICONDUCTOR MATERIAL AND DEVICE CHARACTERIZATION", *Third Edition* **2006**, *John Wiley and Sons, Inc.*, pg. 2-8.

[87] Pearson, W. B., Templeton, I. M., "Superconducting Transition of Lead", *Physical Review* **1958**, *109*, pg. 1094.

[88] Rose-Innés, A. C., Rhoderick, E. H., "Introduction to Superconductivity", *Second Edition* **1978**, *Pergamon Press*, pg. 67-68.

[89] Decker, D. L., et. al., "Critical Field Measurements on Superconducting Lead Isotopes*", *Physical Review* **1958**, *112*, pg. 1888-1898.

[90] Griffiths, P., Haseth, J., "Fourier Transform Infrared Spectrometry", *Second Edition* **2007**, *John Wiley and Sons Inc.*, pg. 148-152.

[91] Hildebrand, M., "The Infrared Optical Properties of Sr2RuO4 and SmTiO3 Including an Object-Oriented Resistivity Interface", *Masters Thesis* **1999**, *Brock University*, pg. 47.

[92] Main, P., Fiske, S. J., et. al., "MULTAN-80: A System of Computer Programs for the Automatic Solution of Crystal Structures from X-ray Diffraction Data" *Univs. of York, England and Louvain, Belgium* **1980**.

[93] Toby, B., "R factors in Rietveld analysis: How good is good enough?", *Powder Diffraction* **2006**, *21*, pg. 67-70.

[94] Toby, B., "What is ICP-MS?... and more importantly, what can it do?", *USGS* **2013**, *https://crustal.usgs.gov/laboratories/icpms/intro.html*.

[95] Barthelmy, D., "Tugarinovite Mineral Data", **2014**, *http://webmineral.com/data/Tugarinovite.shtml#.WHjLuLFh2Rt*

[96] Bando, Y., et al., "Crystal Growth of Molybdenum Oxides by Chemical Transport", *Bulletin of the Institute for Chemical Research* **1976**, *54*, 330-334.

[97] Mercier, J., Fourcaudot, G., "ASPECTS OF CHEMICAL VAPOR TRANSPORT AND CRYSTAL GROWTH OF Mo AND Ti DIOXIDES AND MIXED OXIDES", *Journal of Crystal Growth* **1982**, *59*, 599-604.

[98] "Quadrupole ICP-MS Lab: ICP-MS?", *The University of Texas at Austin, Jackson School of Geosciences* **April 19, 2017**, *http://www.jsg.utexas.edu/icp-ms/icp-ms/*.

[99] Dulski, T., "A Manual for the Chemical Analysis of Metals", *ISBN: 978-0-8031-2066-2* **1996**, *ASTM International*.

[100] Clark, C. M., Dutrow, B. L., "Single-crystal X-ray Diffraction", *Geochemical Instrumentation and Analysis* **2017**, *https://serc.carleton.edu/research_education/geochemsheets/techniques/SXD.html*.

[101] Kundu, S., Nath, T. K., "An Automated Ac Susceptibility Set up Fabricated Using a Closed-Cycle Helium Refrigerator", *Indian Institute of technology Kharagpur*, 1-2.

[102] PPMS Sample Chamber, "Physical Property Measurement System", **Quantum deisgn**, *https://www.qdusa.com/sitedocs/productBrochures/1070-002.pdf.*

[103] Griffiths, D., "Introduction to Electrodynamics", *Third Edition* **1999**, *Prentice-Hall, Inc.*, pg. 310-316.

[104] Mahmood, N., Edminister, J., "Schaum's Outlines: Electric Circuits", *Fourth Edition* **2003**, *McGraw-Hill Companies*, pg. 336-338.

[105] Fitzpatrick, R., Magnetic induction, "Mutual inductance", **2006**, *http://farside.ph.utexas.edu/teaching/em/lectures/node83.html.*

[106] Simon, S., "The Oxford Solid State Basics", **2014**, *University of Oxford*, Lecture1, Lecture 2, Lecture 3, Lecture 4.

[107] Grffiths, D., "Introduction to Quantum Mechanics", *Second Edition* **2005**, *Pearson Education Inc.*, pg. 42-51.

[108] Huang, Di-Jing, "Introduction to Solid State Physics", **2014**, pg. 3-32.

[109] Bose, S., "Phys 4P71: Advanced Condensed Matter Physics", *Brock University* **2012**, *https://brocku.ca/webcal/2012/undergrad/phys.html.*

[110] Barnes, P., et. al., Birkbeck College, University of London. , "Bragg's Law", **2006**, *http://pd.chem.ucl.ac.uk/pdnn/powintro/braggs.htm.*

[111] "The Rigaku Journal", *Rigaku Corporation* **2010**, *26*, 29-30.

[112] Rigaku Corporation Application laboratory Keigo Nagao, "X-ray diffraction for powder sample" *http://homepage.ntu.edu.tw/ kcyuan/form/For_Rigaku-Upload_powder.pdf* pg.1-26.

[113] Peng, X., "Crystal Growth and Characterization of Li0.9Mo6O17", *Brock University* **2012**, pg. 36.

[114] "Maplesoft Product Line", *Waterloo Maple Inc.* **2017**, *http://www.maplesoft.com/products/.*

[115] Van Zeghbroeck, B., Principles of Semiconductor Devices, "2.2.5 Temperature dependence of the energy bandgap", **1997**, *http://ecee.colorado.edu/ bart/book/eband5.htm.*

[116] Jacobsen, M., Laboratory Facilities, "Cornelius Group Website", **2006**, *http://www.physics.unlv.edu/ cornel/labfacilities.htm.*

[117] Hwang, E. H., Das Sarma, S., et al., "The quasiparticle spectral function in doped graphene", *Condensed matter theory center* **2013**, 1-5.

[118] Craven, R. A., Meyer, S. F., "Specific heat and resistivity near the charge-density-wave phase transitions in 2H-TaSe2 and 2H-TaS2", *Physical Review B* **1977**, *16*, 4583-4593.

[119] Landau, L. D., "The Theory of a Fermi Liquid" *Soviet Physics JETP* **1957**, *3* pg. 920-925.

[120] Magnéli, A., Andersson, G., "On the MoO2 Structure Type", *ACTA CHEMICA SCANDINAVICA* **1955**, *9*, pg. 1378-1381.

[121] Damascelli, A., "Probing the Electronic Structure of Complex Systems by ARPES", *Physica Scripta.* **2004**, *T109*, pg. 61–74.